Investigation of Porous Metal Oxide Coatings for a Novel Electrochemical Sensor for Orthophosphate

By

Rachel E. Moss

A dissertation submitted in partial fulfillment of
the requirements for the degree of

Doctor of Philosophy

(Environmental Chemistry and Technology)

at the

UNIVERSITY OF WISCONSIN-MADISON

2012

Date of final oral examination: 06/13/2012

The dissertation is approved by the following members of the Final Oral Committee:
Marc A. Anderson, Professor, Civil & Environmental Engineering
James J. Schauer, Professor, Civil & Environmental Engineering
Katherine D. McMahon, Associate Professor, Civil & Environmental Engineering
Eric E. Roden, Professor, Geology and Geophysics
William J. Hickey, Professor, Soil Science

To my little sister, Sarah.

INVESTIGATION OF POROUS METAL OXIDE COATINGS FOR A NOVEL ELECTROCHEMICAL SENSOR FOR ORTHOPHOSPHATE

Rachel E. Moss

Under the supervision of Professor Marc A. Anderson

At the University of Wisconsin-Madison

Excess phosphorus in the form of inorganic orthophosphates can lead to undesired growth of algae and other aquatic vegetation, ultimately causing the eutrophication of natural water bodies. Currently, phosphate analysis is most commonly performed in a lab setting using time-consuming colorimetric methods. An electrochemical sensor capable of quantifying submicromolar phosphate would make analysis less labor intensive and permit *in situ* measurement of phosphorus in natural waters. This thesis investigates metal oxide coated electrodes as electrochemical detectors of phosphate.

Thin-film nanoporous metal oxyhydroxide and metal oxide coated electrodes were prepared by dip-coating conductive foil in stable colloidal solutions (sols) of iron oxide, titania, zirconia, and/or alumina followed by thermal treatment that produced a stable ceramic on the support. Phosphate anions adsorbed to metal oxides via inner-sphere mechanisms that measurably perturbed electrochemical properties. The high surface area of these coatings amplified chemical changes upon phosphate adsorption such that they were measured with cyclic voltammetry (CV) and electrochemical impedance spectroscopy (EIS).

The electrochemical responses of a hematite iron oxide electrode in phosphate solution were: 1) more prominent cathodic and anodic features visible in cyclic voltammograms, and 2)

alterations in impedance that could be tied to trends in Bode phase plots and model circuits. A lin-log relationship between the phase angle of impedance (θ) at frequency 0.2 Hz and phosphate concentration 10 nM − 0.1 mM (0.31 $\mu g \cdot L^{-1}$ – 3.1 $mg \cdot L^{-1}$ as P) gave a coefficient of determination (R^2) of 0.93 or greater for the pH range 6.75 to 8.25. At pH 7, the correlation between phase of impedance and phosphate concentration had a resolution of half-log units over a full 1 nM to 0.1 mM (31 $ng \cdot L^{-1}$ – 3.1 $mg \cdot L^{-1}$ as P) range in both inert perchlorate electrolyte and in simulated lake water that contained competing ions. Modeled equivalent circuits with constant phase elements gave consistent fits for the hematite electrode response to phosphate. Phosphate was also found to perturb features of EIS and CV plots using the titanium oxide, zirconium oxide, and aluminum oxide thin-film electrodes tested over a circumneutral pH range. The results of this dissertation work show promise for the development of a novel, real-time electrochemical sensor composed of nanoporous metal oxide materials for the monitoring of phosphate in aquatic ecosystems.

Approved:

Date: June 13, 2012

Signature: 

Marc A. Anderson, Professor
Environmental Chemistry & Technology

ACKNOWLEDGEMENTS

I wish to first express my gratitude to my Ph.D. advisor Professor Marc Anderson for his mentorship, encouragement, and constant support through my graduate career. In addition to giving me the resources necessary for my research, his good attitude through my time here has been invaluable. It has been my pleasure to be his advisee.

I have also greatly appreciated my collaboration with Jennifer Jackowski, particularly for her work in the initial stages of the phosphate sensor project. I am thankful to Rodolfo Pérez-Roa for his indispensible contribution to statistical analysis. Both have been great allies, and I have been very fortunate to get to know them through my time in Marc Anderson's lab.

I thank Isabel Tejedor for her experimental assistance and knowledgeable advice. Her attentiveness and skill have been greatly appreciated. Also important have been the assistance and encouragement from many of Marc's current and past graduate students, including Yukihiro Hara, Ramsey Kropp, Jesse Wouters, Jessica Sanfilippo Silva, and Kevin Leonard. Additionally, I attribute a great deal of my success to the support of current and former graduate students from Joel Pedersen's lab: Kartik Kumar, Clarissa Booth, Christen Bell Smith, and Kurt Jacobson.

Many thanks go to Will Bleam, Bill Hickey, and Shicheng Chen for their mentorship during the tenure of the siderophore project previous to my work with Marc Anderson. I also thank Jamie Schauer, Eric Roden, and Trina McMahon for their advice and participation as committee members and for their support through the process.

Finally, my work would not have been possible without funding from the National Resources Initiative (NRI), the National Science Foundation (NSF), and the University of Wisconsin-Madison Graduate School.

Table of Contents

Page

Acknowledgements ..... **iv**

List of Tables ..... **ix**

List of Figures ..... **x**

Nomenclature ..... **xvi**

1. INTRODUCTION **1**

1.1. Phosphorus Monitoring **1**

1.1.1. Phosphorus in the Environment 1

1.1.2. Current State of Phosphate Sensors 2

1.2. Chemistry of the Oxide-Solution Interface **4**

1.2.1. The Electrical Double Layer 4

1.2.2. Metal Oxides 7

1.2.3. Potential-Determining Anions 8

1.3. Sol-Gel Chemistry **10**

1.4. Electrochemistry **11**

1.4.1. Electrochemical Cell 11

1.4.2. Electrochemical Methods 13

1.4.2.1. Cyclic Voltammetry 13

1.4.2.2. Electrochemical Impedance Spectroscopy 14

1.5. Purpose of This Study **16**

References **17**

Tables **24**

Figures **25**

2. DEVELOPMENT AND EVALUATION OF A NANOPOROUS IRON (HYDR)OXIDE ELECTRODE FOR PHOSPHATE SENSING 27

Abstract 27

2.1. Introduction 27

2.2. Experimental 31

2.2.1. Iron (Hydr)oxide Electrode Synthesis 31

2.2.2. Chemicals 33

2.2.3. Apparatus and Electroanalytical Procedure 34

2.3. Results and Discussion 36

2.3.1. Electrode Characterization 36

2.3.2. Stability of Electrode Coating with Potential Cycling 37

2.3.3. Electrochemical Analysis of Phosphate Using Cyclic Voltammetry 38

2.3.4. Electrochemical Analysis of Phosphate Using Electrochemical Impedance Spectroscopy 40

2.3.5. Limitations from Hysteresis 44

2.3.6. Comparison of Phosphate Signal with Arsenate 44

2.3.7. Electrochemical Analysis of Phosphate in Simulated Lake Water 45

2.4. Conclusion 46

References 48

Figures 57

3. EFFECTS OF pH ON PHOSPHATE ADSORPTION TO HEMATITE AS STUDIED WITH CYCLIC VOLTAMMETRY AND ELECTROCHEMICAL IMPEDANCE SPECTROSCOPY 70

Abstract 70

3.1. Introduction 71

3.2. Experimental 73

3.3. Results and Discussion 77

3.3.1. Electrode Characterization 77

3.3.2. Cyclic Voltammograms 78
3.3.3. Charge Storage 84
3.3.4. Electrochemical Impedance Spectroscopy 85
3.4. Conclusion 91
References 93
Figures 99

4. ELECTROCHEMICAL RESPONSE OF TITANIA, ZIRCONIA, AND ALUMINA ELECTRODES TO PHOSPHATE 110
Abstract 110
4.1. Introduction 111
4.2. Experimental 113
4.2.1. Sol Preparation 113
4.2.2. Electrode Preparation and Characterization 114
4.2.3. Chemicals 115
4.2.4. Apparatus and Electroanalytical Procedure 116
4.3. Results and Discussion 118
4.3.1. Electrode Coating 118
4.3.2. Electrochemical Analysis 120
4.3.2.1. Titania 120
4.3.2.2. Zirconia 124
4.3.2.3. Alumina 126
4.3.3. Memory Effects 128
4.4. Conclusion 128
References 130
Tables 137
Figures 138

5. CONCLUDING REMARKS AND RECOMMENDATONS 164

5.1. Concluding Remarks 164

5.2. Recommendations for Further Study 166

References 168

Appendix A. OUTPUT OF THE EQUIVALENT CIRCUIT MODEL FOR THE HEMATITE ELECTRODE IN PHOSPHATE 170

LIST OF TABLES

Page

Table 1.1 Isoelectric pH values of oxide materials referenced in this work 24

Table 4.1 Isoelectric pH values of metal oxide ceramics prepared via sol-gel methods 137

Table A.1 Parameters of best fit to model circuit $R_S + Q_1/(R_2+Q_2)/(R_3+C_4/R_4)$ for electrochemical impedance spectra of the hematite electrode in 5 mM $NaClO_4$, pH 6.00 – 8.75 171

Table A.2 Parameters of best fit to model circuit $R_S + Q_1/(R_2+Q_2)/(R_3+C_4/R_4)$ for electrochemical impedance spectra of the hematite electrode in 10^{-8} M phosphate, 5 mM $NaClO_4$, pH 6.00 – 8.75 172

Table A.3 Parameters of best fit to model circuit $R_S + Q_1/(R_2+Q_2)/(R_3+C_4/R_4)$ for electrochemical impedance spectra of the hematite electrode in 10^{-7} M phosphate, 5 mM $NaClO_4$, pH 6.00 – 8.75 173

Table A.4 Parameters of best fit to model circuit $R_S + Q_1/(R_2+Q_2)/(R_3+C_4/R_4)$ for electrochemical impedance spectra of the hematite electrode in 10^{-6} M phosphate, 5 mM $NaClO_4$, pH 6.00 – 8.75 174

Table A.5 Parameters of best fit to model circuit $R_S + Q_1/(R_2+Q_2)/(R_3+C_4/R_4)$ for electrochemical impedance spectra of the hematite electrode in 10^{-5} M phosphate, 5 mM $NaClO_4$, pH 6.00 – 8.75 175

Table A.6 Parameters of best fit to model circuit $R_S + Q_1/(R_2+Q_2)/(R_3+C_4/R_4)$ for electrochemical impedance spectra of the hematite electrode in 10^{-4} M phosphate, 5 mM $NaClO_4$, pH 6.00 – 8.75 176

LIST OF FIGURES

Page

Figure 1.1 Diagram of the electrical double layer (edl) of a positively charged oxide electrode with associated potential Φ at function of distance x from the surface 25

Figure 1.2 Speciation of orthophosphate over pH range 3 – 11 26

Figure 2.1 X-ray diffraction peak profiles of pure hematite (α-Fe_2O_3) compared to Electrode A (*above*) and Electrode B (*below*) 57

Figure 2.2 Decay in anodic peak current (I_{ap}) with repeated potential cycling, as a percent of maximum I_{ap} value, for Electrode A (amorphous ferrihydrite) and Electrode B (hematite) in 10^{-3} M phosphate, 0.01 M $NaClO_4$, pH 4. Cyclic voltammetric scans are -0.2 V – 0.8 V vs. SCE at 100 $mV \cdot s^{-1}$ 58

Figure 2.3 (*above*) Electrode A cyclic voltammograms of increasing phosphate concentration in 0.01 M $NaClO_4$, pH 4; (*below*) Fit of anodic peak current values for 10^{-9} – 10^{-3} M phosphate using Equation (1) 59

Figure 2.4 (*above*) Electrode B cyclic voltammograms of increasing phosphate concentration in 0.01 M $NaClO_4$, pH 4; (*below*) Fit of anodic peak current values for 10^{-9} – 10^{-3} M phosphate using Equation (1) 60

Figure 2.5 Bode phase plot for 10^{-9} – 10^{-4} M phosphate in 5 mM $NaClO_4$, pH 7, at bias voltage -0.24 V vs. SCE over the frequency range of 10 mHz to 10 kHz with dotted line indicating 0.2 Hz 61

Figure 2.6 Fit of the phase of impedance vs. the log of molar phosphate concentration at f = 0.2 Hz for 10^{-9} – 10^{-4} M phosphate in 5 mM $NaClO_4$, pH 7..... 62

Figure 2.7 Nyquist plot for 10^{-9} – 10^{-4} M phosphate in 5 mM $NaClO_4$, pH 7, over the frequency range 200 kHz to 5 mHz 63

Figure 2.8 Nyquist plot for 10^{-7} – 10^{-4} M phosphate in 5 mM $NaClO_4$, pH 7, at high frequencies, with f = 2 Hz indicated for 10^{-4} M phosphate curve 64

Figure 2.9 Bode phase plot for 10^{-9} – 10^{-4} M phosphate in 5 mM $NaClO_4$, pH 4, at bias voltage -0.04 V vs. SCE over the frequency range of 50 mHz – 10 kHz, with dotted line indicating 0.5 Hz 65

Figure 2.10 Fit of the phase of impedance vs. the log of molar phosphate concentration at f = 0.5 Hz, bias voltage -0.04 V vs. SCE, for 10^{-9} – 10^{-4} M phosphate in 5 mM $NaClO_4$, pH 4 66

Figure 2.11 Bode phase plot for 10^{-9} – 10^{-4} M arsenate in 5 mM $NaClO_4$, pH 7, at bias voltage -0.24 V vs. SCE over the frequency range of 10 mHz – 10 kHz, with dotted line indicating 0.2 Hz 67

Figure 2.12 Bode phase plot for 10^{-9} – 10^{-4} M phosphate in simulated lake water, pH 7, at bias voltage -0.24 V vs. SCE over the frequency range of 50 mHz – 10 kHz, with dotted line indicating 0.2 Hz 68

Figure 2.13 Fit of the phase of impedance vs. the log of molar phosphate concentration at f = 0.2 Hz for 10^{-9} – 10^{-4} M phosphate in simulated lake water, pH 7 69

Figure 3.1 Scanning electron micrograph of hematite electrode edge at 1000x magnification 99

Figure 3.2 Cyclic voltammograms of blank solutions containing 5 mM $NaClO_4$ at selected pH 100

Figure 3.3 Cyclic voltammograms at pH 6.00, phosphate concentrations 10^{-8} – 10^{-4} M after subtraction of $NaClO_4$ voltammograms 101

Figure 3.4 Cyclic voltammograms at pH 8.75, phosphate concentrations 10^{-8} – 10^{-4} M after subtraction of $NaClO_4$ voltammograms 102

Figure 3.5 Cyclic voltammograms of 10^{-4} M phosphate at three pH values after subtraction of $NaClO_4$ voltammograms 103

Figure 3.6 Excess charge held by the hematite electrode in phosphate-containing solutions (10^{-8} – 10^{-4} M) in the low voltage zone, E < 0.2 V vs. SCE 104

Figure 3.7 Effect of bias potential on the Bode phase plot obtained by EIS in 5 mM $NaClO_4$, pH 7.00 105

Figure 3.8 Real (*above*) and imaginary (*below*) impedance of a phosphate-free and 10^{-4} M phosphate system at pH 6.00 and 8.75 106

Figure 3.9 Graphical representation of the equivalent circuit analog for the hematite electrode 107

Figure 3.10 Bode phase plot of experimental EIS data with best fit from the equivalent circuit for 5 mM $NaClO_4$ and 10^{-6} M phosphate, pH 7.00 108

Figure 3.11 Values of selected equivalent circuit components R_2, Q_2, R_3, and R_4 as a function of pH and C_{PO4}. Phosphate concentrations are Δ 10^{-8} M, □ 10^{-6} M, ♦ 10^{-4} M. The solid line represents phosphate-free system values 109

Figure 4.1 Scanning electron micrograph of titania (TiO_2) coated electrode surface with 10,000x magnification 138

Figure 4.2 Scanning electron micrograph of zirconia (ZrO_2) coated electrode surface with 10,000x magnification 139

Figure 4.3 Scanning electron micrograph of γ-alumina (γ-Al_2O_3) coated electrode surface with 10,000x magnification 140

Figure 4.4 Cyclic voltammograms of the titania coated electrode in 5 mM $NaClO_4$ over the pH range 6.00 – 8.50. Arrows denote the anodic and cathodic potential sweep direction 141

Figure 4.5 Cyclic voltammograms of the titania coated electrode in 10^{-6} M phosphate, 5 mM $NaClO_4$, over the pH range 6.00 – 8.50 142

Figure 4.6 Cyclic voltammograms of the titania coated electrode in 10^{-4} M phosphate, 5 mM $NaClO_4$, over the pH range 6.00 – 8.50 143

Figure 4.7 Cyclic voltammograms of the titania coated electrode in 5 mM $NaClO_4$ and in 10^{-8} M, 10^{-7} M, 10^{-6} M, 10^{-5} M, and 10^{-4} M phosphate, pH 6.00 144

Figure 4.8 Cyclic voltammograms of the titania coated electrode in 5 mM $NaClO_4$ and in 10^{-8} M, 10^{-7} M, 10^{-6} M, 10^{-5} M, and 10^{-4} M phosphate, pH 7.25 145

Figure 4.9 Cyclic voltammograms of the titania coated electrode in 5 mM $NaClO_4$ and in 10^{-8} M, 10^{-7} M, 10^{-6} M, 10^{-5} M, and 10^{-4} M phosphate, pH 8.50 146

Figure 4.10 Nyquist plot of the titania coated electrode in 5 mM $NaClO_4$ at pH 6.00, 7.25, and 8.50. The electrochemical impedance spectra bias voltage was -0.24 V vs. SCE, with frequency range 50 mHz – 10 kHz 147

Figure 4.11 High frequency region of Nyquist plot of the TiO_2 coated electrode in 5 mM $NaClO_4$ at pH 6.00, 7.25, and 8.50 148

Figure 4.12 Nyquist plot of the titania coated electrode in 5 mM $NaClO_4$ and in 10^{-8} M, 10^{-7} M, 10^{-6} M, 10^{-5} M, and 10^{-4} M phosphate, pH 7.25 149

Figure 4.13 Bode phase plot of the titania coated electrode in 5 mM $NaClO_4$ over the pH range 6.00 – 8.75. The dotted line indicates the frequency 10 Hz 150

Figure 4.14 Bode phase plot of the titania coated electrode in 5 mM $NaClO_4$ and 10^{-8} M, 10^{-7} M, 10^{-6} M, 10^{-5} M, and 10^{-4} M phosphate, pH 8.50. The dotted line indicates the frequency 10 Hz 151

Figure 4.15 Cyclic voltammograms of the zirconia coated electrode in 5 mM $NaClO_4$ over the pH range 6.00 – 8.50 152

Figure 4.16 Cyclic voltammograms of the zirconia coated electrode in 10^{-6} M phosphate, 5 mM $NaClO_4$, over the pH range 6.00 – 8.50 153

Figure 4.17 Cyclic voltammograms of the zirconia coated electrode in 10^{-4} M phosphate, 5 mM $NaClO_4$, over the pH range 6.00 – 8.50 154

Figure 4.18 Cyclic voltammograms of the zirconia coated electrode in 5 mM $NaClO_4$ and in 10^{-8} M, 10^{-7} M, 10^{-6} M, 10^{-5} M, and 10^{-4} M phosphate, pH 6.00 155

Figure 4.19 Bode phase plot of the zirconia coated electrode in 5 mM $NaClO_4$ over the pH range 6.00 – 8.75. The dotted line indicates the frequency 0.2 Hz 156

Figure 4.20 Nyquist plot of the zirconia coated electrode in 5 mM $NaClO_4$ at pH 6.00, 7.25, and 8.50 157

Figure 4.21 Nyquist plot of the zirconia coated electrode in 5 mM $NaClO_4$ and in 10^{-8} M, 10^{-7} M, 10^{-6} M, 10^{-5} M, and 10^{-4} M phosphate, pH 7.25 158

Figure 4.22 Bode phase plot of the zirconia coated electrode in 5 mM $NaClO_4$ and in 10^{-8} M, 10^{-7} M, 10^{-6} M, 10^{-5} M, and 10^{-4} M phosphate, pH 8.50. The dotted line indicates the frequency 0.2 Hz 159

Figure 4.23 Cyclic voltammograms of the alumina coated electrode in 5 mM $NaClO_4$ over the pH range 6.00 – 8.50 160

Figure 4.24 Nyquist plot of the alumina coated electrode in 5 mM $NaClO_4$ at pH 6.00, 7.25, and 8.50 161

Figure 4.25 Bode phase plot of the alumina coated electrode in 5 mM $NaClO_4$ over the pH range 6.00 – 8.75. The dotted line indicates the frequency 0.2 Hz 162

Figure 4.26 Bode phase plot of the alumina coated electrode in 5 mM $NaClO_4$ and in 10^{-8} M, 10^{-7} M, 10^{-6} M, 10^{-5} M, and 10^{-4} M phosphate, pH 8.50. The dotted line indicates the frequency 0.2 Hz 163

NOMENCLATURE

C	Concentration or Capacitance
E	Voltage
E	Time-Dependent Voltage
I	Current or Ionic Strength
I	Time-Dependent Current
J	Current Density
K_a	Acid Dissociation Constant
Q	Constant Phase Element
R	Resistance
R^2	Coefficient of Determination
V	Voltage or Volts
Z	Impedance
α	Constant Phase Element Coefficient
ζ	Zeta Potential
θ	Phase of Impedance
σ	Charge Density
Φ	Electrochemical Potential

AC	Alternating Current
BET	Braunauer-Emmett-Teller
CPE	Constant Phase Element

CV	Cyclic Voltammetry
DC	Direct Current
edl	Electrical Double Layer
EIS	Electrochemical Impedance Spectroscopy
FTIR	Fourier Transform Infrared
ICP-OES	Inductively-Coupled Plasma Optical Emission Spectrometry
iep	Isoelectric pH or Isoelectric Point
IHP	Inner Helmholtz Plane
ISE	Ion-Selective Electrode
LWCC	Liquid Waveguide Capillary Cells
MAGIC	Magnesium Induced Co-Precipitation
NMR	Nuclear Magnetic Resonance
OCP	Open Circuit Potential
OHP	Outer Helmholtz Plane
pzc	Point of Zero Charge
SCE	Standard Calomel Electrode
SCM	Surface Complexation Model
SEM	Scanning Electrode Microscope
SHE	Standard Hydrogen Electrode
SPEIS	Stepped-Potential Electrochemical Impedance Spectroscopy
SSA	Specific Surface Area
TP	Total Phosphorus
XRD	X-Ray Diffraction

CHAPTER 1

INTRODUCTION

1.1. Phosphorus Monitoring

1.1.1. Phosphorus in the Environment

Phosphorus is an essential element for all known species as a necessary component of genetic material, lipid membranes, and molecules for cellular energy storage. An excess of phosphorus in aquatic systems, however, is detrimental to water quality and local ecosystems. Phosphorus was confirmed to be a limiting nutrient for plant growth in long-term whole-lake studies conducted by Schindler (1974) [1] with a greater correlation to lake biomass production than nitrogen input [2]. The inorganic orthophosphates (PO_4^{3-} and its conjugate acids, HPO_4^{2-}, $H_2PO_4^-$, and H_3PO_4), collectively called phosphates, are the most bioavailable form of phosphorus, since these molecules are most easily metabolized by cells. Experimental lakes spiked with phosphate resulted in the water bodies entering states of eutrophication, where excessive levels of this limiting nutrient caused an overgrowth of algae [1]. Increased algal growth in turn led to greater quantities of oxygen-consuming microorganisms, decreasing the dissolved oxygen in these water systems thereby causing fish kills and a reduction in biodiversity. Great amounts of bioavailable phosphorus can enter water systems from runoff from fertilizers, sewage, and animal waste, with the problem compounded by soil erosion due to land development. Governmental bodies such as the U.S. Environmental Protection Agency have made recommendations for maximum orthophosphate levels in lakes and rivers [3], and the

careful monitoring of phosphate levels is key to protecting freshwater bodies from algal blooms and resultant damage to aquatic ecosystems.

1.1.2. Current State of Phosphate Sensors

The U.S. Environmental Protection Agency has established a recommended limit of 0.05 ppm phosphate (as P) for lakes in order to avoid eutrophication. This corresponds to a concentration of 1.6 micromolar (10^{-6} M) in phosphate. However, the actual limit needed to protect water bodies may be less; the Organisation for Economic Cooperation and Development (1982) [4] put the upper limit for non-eutrophic lakes at 0.035 ppm in total phosphorus (TP). This may correspond to actual phosphate concentrations on the nanomolar (10^{-9} M) scale [5]. The testing of phosphate concentrations in natural waters most commonly necessitates the filtering of a collected sample followed by the addition of a chemical reagent that produces a colored phosphate complex that can be measured with a UV-visible spectrophotometer. The magnitude of the signal is then compared against a standard curve with known phosphate concentrations [6]. This analysis is generally performed in a laboratory setting away from the water source and can be laborious when there are a great number of samples to be tested. Furthermore, the error in analysis is high where concentrations are near the micromolar detection limit using the most common colorimetric testing methods. Commercially, a few commercial optical sensors for phosphate work on this same principle, where a water sample is injected into the measuring device and mixed with a reagent that develops a color with intensity indicative of the amount of phosphate present. However, these commercially available instruments are generally made for wastewater monitoring, where the phosphate concentration exceeds the micromolar detection limit of the device. Submicromolar concentrations of phosphate have been

measured colorimetrically using liquid waveguide capillary cells (LWCC) [7-10], in which the path length of light through the cell can be 1 – 2 meters long, so that low concentrations can be determined as in accordance with Beer's law, and the magnesium induced co-precipitation (MAGIC) method [9, 11-13], in which phosphate is preconcentrated, centrifuged, and resuspended to increase concentrations above usual detection limits. However, both of these methods may be impractical for general use in real water samples due to bulky equipment and long wait times for chemical equilibrium to be established before measurement.

Over the past two decades, many researchers have investigated the possibility of electrochemical sensors for phosphate that would eliminate the need for optical methods. Commercial ion selective electrodes (ISEs) already exist for many other aqueous analytes, of which the most common is the pH meter for measuring H^+ concentration. ISEs also exist for Cl^-, SO_4^{2-}, Ca^{2+}, Na^+, and NH_4^+ and other ions. Unfortunately, there is currently no commercial ISE for phosphate. In research laboratories, some progress has been made with respect to the electrochemical measurement of phosphate using potentiometric methods, where phosphate adsorption to an electrode produces a measurable voltage change. Among proposed potentiometric electrodes are cobalt(II) oxide rods that have been found to have good specificity to phosphate and a 10 μM detection limit. Additionally, amperometric biosensors for phosphate have been investigated. Here, enzymes immobilized on an electrode react with phosphate to produce measurable current from the reduction of O_2. These sensors have been purported to have submicromolar phosphate detection limits [14]. Unfortunately, enzymes are not very robust and must be in buffered solutions or they may be denatured. A comprehensive summary of the literature on proposed electrochemical methods of phosphate detection is found in Engblom (1998) [15].

1.2. Chemistry of the Oxide-Solution Interface

1.2.1. The Electrical Double Layer

At time-averaged equilibrium conditions, an electrolyte solution has no potential gradient in the absence of contact with a boundary surface. Small positive and negative ions and their solvating molecules are randomized in the bulk solution by thermal and fleeting electrostatic intermolecular forces. Electroneutrality is maintained by the even charge distribution within the electrolyte.

Introduction of a solid electrode, such as a conducting metal or carbon, to an electrolyte changes the time-averaged positioning of solvated ions and free solvent molecules near the surface of the solid, as the electrolyte must accommodate the charge at the electrode surface to continue to enforce overall electroneutrality. This requirement for a conservation of charge at the electrode-solution interface can be described in terms of charge density, an excess or deficiency of electrons of the constituent parts of the interface in units of charge per area of the surface. If the total charge density of the metal electrode near its surface is σ^M and the balancing total charge density of the electrolyte solution in the vicinity of the electrode is σ^S, then

$$0 = \sigma^M + \sigma^S \qquad (1)$$

$$\text{thus, } -\sigma^M = \sigma^S$$

The solution side is frequently interpreted by the Gouy-Chapman-Stern model as an "electrical double layer" (edl) that describes the distribution of electrolyte charges and oriented dipoles that make up the interfacial region at the boundary of the solid-solution interface. The electrical double layer further consists of a compact and diffuse layer, extending over a distance

from the electrode surface into the bulk solution. The compact layer, closest to the electrode, is further separated into the Inner Helmholtz Plane (IHP) and the Outer Helmholtz Plane (OHP). The diffuse layer consists of thermally fluctuating, loosely associated ions that screen the charge of the electrode and compact layer from the bulk electrolyte, with thickness dependent on ion concentration. A schematic of the electrical double layer for a positively charged electrode surface is in Figure 1.1.

Together, the balancing charge density of the electrolyte (σ^S) is the combined sum of the charge density of the tightly-bound ions and molecules of the Inner Helmholtz Plane (σ^{IHP}), the loosely bound Outer Helmholtz Plane (σ^{OHP}), and the transient diffuse layer (σ^d), such that:

$$-\sigma^M = \sigma^{IHP} + \sigma^{OHP} + \sigma^d \quad (2)$$

In the Outer Helmholtz Plane, ions are only interacting with the electrode surface via outer-sphere mechanisms, where fully solvated ions of opposite charge to the electrode are more concentrated at the interface than in bulk solution. In this layer, the solvated ions are non-specifically adsorbed to the charged electrode surface, and the interactions between ion and electrode involve only long-range electrostatic forces. The distance of closest approach is limited by the solvation shell, shown as x_2 in Figure 1.1.

The Inner Helmholtz Plane consists of solvent molecules and partially or fully desolvated ions that penetrate the inner-sphere of the electrode surface. These ions interact with the solid electrode through stronger, short-range interactions to form a partial or complete layer over the surface area of the material. Ions found in the IHP are considered specifically adsorbed to the solid surface, often with very large binding constants. The distance of closest approach to the

electrode surface (x_1 in Figure 1.1) is less than for the OHP, and is generally on the order of 10 Å.

When a metal electrode potential (Φ_m) and bulk electrolyte solution potential (Φ_s) differ, there is a potential gradient between these two values extending from the surface of the electrode. At x_1, at the IHP, the potential at this distance of specifically adsorbing ions is considered the Stern potential. Unfortunately, this potential may not be directly measured. At a distance x_2, determined by the closest plane of hydrated ions, there is the zeta (ζ) potential that can be measured with electrophoretic mobility experiments. Since the charge at the surface is not directly determined, the ζ potential is a helpful approximation of surface charge and gives information about charge screening. At a farther distance from the electrode, going into the diffuse layer, the potential approaches the asymptotic value of the bulk electrolyte.

Adsorption of an ion onto surfaces has been evaluated with many different surface complexation models in attempts to use experimental data (from adsorption, electrophoretic mobility, IR, NMR, XANES, and others) to make inferences about ion speciation (*e.g.*, a monoprotonated or nonprotonated phosphate ion) and conformation (*e.g.*, monodentate or bidentate) of ions adsorbed at or near the surface. This information about the characteristics of adsorption of specifically adsorbing ions on mineral surfaces, particularly with respect to capacitance, can provide a useful tool with respect to developing new theories where electrochemical data can be used to determine the characteristics of phosphate adsorption on metal oxide electrode materials.

1.2.2. Metal Oxides

Metal oxides are a class of minerals for which the most simple lattice would be a repeating unit of a single metallic element (*e.g.*, Fe or Al) and oxygen. Similar lattices containing a metal with -OH groups are metal hydroxides, and when the lattice contains both oxygen and -OH groups, they are classified as metal oxyhydroxides. Collectively, these minerals are referred to as metal (hydr)oxides, or sometimes more generally as metal oxides. Surface modeling of these minerals illuminate processes at the solid-liquid interface, including specific adsorption, ion exchange, and dissolution; a good resource for general surface models of oxides is contained in a book on the topic by Stumm (1992) [16].

Metal oxides used in these studies are iron (hydr)oxides, aluminum (hydr)oxides, titanium dioxide, and zirconium dioxide produced from sols. Iron (hydr)oxides (*e.g.*, goethite, hematite, ferrihydrite, and magnetite) and aluminum (hydr)oxides (*e.g.*, boehmite and gibbsite) are abundant minerals in soils and sediments. Both Fe and Al (hydr)oxides are generally nontoxic and are chemically stable over an environmental pH range. Titanium dioxide, TiO_2, in anatase and rutile forms, is also found naturally, and it has many industrial applications as a white pigment, and, more recently, in the development of dye-sensitized solar cells. Zirconium dioxide, ZrO_2, is not found in large quantities in natural minerals but can easily be produced commercially. Zirconium dioxide ceramic materials have wide use in industry for their insulating, light refractive, and ion conductive properties.

The surface charge of these (hydr)oxides are pH dependent. The movement of these suspended colloidal particles in an applied electric field is used to determine the ζ potential (the potential at the sheer plane, located at a distance angstroms from the surface) of these materials as a function of the pH of the suspension. A pH designated as the point of zero charge (pzc) is

where the particles in water no longer move in an electric field; below this pzc the oxide has net positive charge, and above the pzc the oxide has net negative charge. The mobility of the particle in the electric field, and thus the ζ potential, is also changed by increasing ionic strength of the aqueous colloidal suspension, as charge is screened by the electrolyte. However, the pzc is not greatly changed when the electrolyte ions are inert (*i.e.*, do not enter the IHP), and net zero charge values for oxides are often given in the literature as not the pzc but the isoelectric pH (iep), the net zero charge pH value in an inert electrolyte solution (often KNO_3). Isoelectric pH values for oxides used these studies are listed in Table 1.1. These values vary based on preparation procedures and trace impurities, and natural oxides taken from environmental sources tend to have lower iep values than those synthetically prepared due to adsorption of carbonate, phosphate, and other ions that are not inert to the material [17].

1.2.3. Potential-Determining Anions

Ions specifically adsorbed into the IHP of a mineral surface are potential-determining – their adsorption perturbs the electrical double layer and effects electrochemical properties of the material [18, 19]. H^+ and OH^- are potential determining ions on oxides that control the zeta potential, related to surface charge, in a Nernstian fashion. Potential-determining anions can adsorb to an oxide via ligand exchange with less acidic surface hydroxyl groups, with the effect of decreasing surface affinity for protons [20]. Thus, as fewer protons are required to neutralize charge, the specific adsorption of anions will lower the isoelectric pH, the pH at which there is no net charge on the surface, from the natural point of zero charge of the material. Similarly, specific adsorption of cations increase positive charge and increase the isoelectric pH by displacing surface protons [21]. Electrophoretic mobility experiments are used to determine

whether an anion is potential-determining. Although both inert and potential-determining ions will change the ζ potential in a concentration dependent way via charge screening, only potential-determining ions are expected to shift the isoelectric pH with increasing ion concentration.

The inorganic orthophosphates, generally as HPO_4^{2-} and $H_2PO_4^-$ at natural pH, have been well-studied as potential-determining anions producing a concentration-dependent shift in isoelectric pH for a series of oxide materials, including iron (hydr)oxides (*e.g.*, goethite [22-27], hematite [28], magnetite [29], ferrihydrite [30], and amorphous FeOOH [31]), titania (anatase [32] and amorphous TiO_2 [33]), alumina (γ-Al_2O_3 and amorphous $Al(OH)_3$ [32]), and zirconia [34]. The iep shift from a specifically adsorbing phosphate can be dramatic. For instance, micromolar concentrations of phosphate added to goethite (α-FeOOH) was found to shift downward the iep of the mineral from its pristine point of zero charge by 5 pH units [27]. Surface complexation modeling has been especially useful for investigating phosphate adsorption on many of these materials, and many studies have shown both a pH and a surface loading dependence on the speciation of phosphate on metal oxides [23, 25, 30, 35-38].

Often, anions specifically adsorb to oxides only over a certain range of pH values, as surface functional groups may have changes in Lewis acidity. The adsorption process may be further complicated when specifically adsorbing molecules have conjugate acids or bases so that the charge of the ion is itself dependent on the pH of the solution, such as the case for phosphate with pK_a values at 2.16, 7.21, and 12.32 (Figure 1.2).

When both the oxide surface and the adsorbing species have the same charge, coulombic repulsion of like-charged surfaces and ions can out-compete close-range attractive forces. However, inner-sphere adsorption of phosphate does occur at pH values above the iep [39-43].

Further complicating the study of adsorption processes, speciation on the oxide surface may not match the speciation in the bulk electrolyte [44, 45]. Protons or the hydroxide anion may also compete with other ions at low and high pH values respectively. Surface complexation models that predict ion orientation and speciation at the solid/solution interface are useful for interpreting these complex systems.

1.3. Sol-Gel Chemistry

Sols are stable suspensions of colloidal solid particles in a liquid. The particles must be great enough in size to not just be considered large molecules, but small enough that the forces of dispersion to be greater than those of gravity – this corresponds to a particle size range between 2 nm and 0.2 μm. These suspensions may be shelf-stable for a period of several years without precipitation or settling of the colloids.

Metal (hydr)oxide sols can be applied to an electrode backing via spray coating or dip coating procedures, resulting in a layer of sol of approximately uniform thickness on the substrate that can be dried in air. As the solvent evaporates, the charged colloidal particles are destabilized from the original sol solution and become linked via van der Waals forces. With further evaporation, gelation occurs. The gel on the substrate is no longer a fluid, as forced interaction of electrical fields on material surfaces result in a complex, three-dimensional network that prevents translational movement of particles.

When the gel is fully dried, the resulting solid is a xerogel film that is brittle and very porous. To produce a robust coating, the xerogel-coated electrode is fired in an oven with programmed temperature and heating time. The thermal treatment sinters the small colloidal particles together into a three dimensional ceramic film attached to the electrode substrate. The

composition of films may partially or fully undergo mineral phase changes when the material is heated to hundreds of ˚C, and the extent of the phase change may be time dependent. Porosity (% of volume that is air) and the size of pores through the material tend to be dependent on sintering time and temperature.

The final ceramic film material may have very high specific surface areas, often several hundreds of square meters per gram. Extensive surface area is a result of a high density of nanopores, particularly micropores (less than 2 nm in diameter) and mesopores (2 – 50 nm in diameter), interspersed throughout the material. The porous film permits more area for interactions between an aqueous solution and the material. In this respect, sol-gel produced nanoporous coated electrodes can be a good choice when one wishes to measure the perturbation of the electrochemical double layer due to specific ion adsorption. In this fashion, a sensitive ion selective electrode may be produced from these nanoporous oxide films.

1.4. Electrochemistry

1.4.1. Electrochemical Cell

An electrochemical cell for analytical experiments is comprised of a potentiostat connected to three electrodes immersed into a solution or suspension. These electrodes are the: 1) working, 2) reference, and 3) counter electrodes.

The working (or indicator) electrode is the location at which the process of interest is occurring. It is often made of conducting metal or carbon, often coated with layers of a solid material of interest. Examples of working electrode coatings in electrochemical experiments include metal oxides and reaction catalysts such as enzymes.

Voltage applied to the working electrode cannot be measured in isolation, so a reference electrode with known redox properties is needed. Voltage between the working and reference electrode is what is precisely measured and controlled in a feedback mechanism in the potentiostat. The reference electrode should have a known redox potential and is optimally non-polarizable (*i.e.*, voltage measured will not be dependent on the passage of current). It should also be placed as close as possible to the working electrode to prevent a large uncompensated resistance from the solution. The classic reference is the standard hydrogen electrode (SHE) that literature values of redox potentials are given in relation to (thus, E^0_{SHE} is defined as 0 V at all temperatures). The SHE has pure hydrogen gas bubbled through a platinum electrode at 1 bar in 1 M acid. Use of the SHE is not practical in most analytical electrochemical experiments, thus an alternate reference electrode with known redox potential is used. In this work, the commercially available saturate calomel electrode (SCE) is used as the reference, with E^0 = +0.244 V (vs. SHE) and reduction half reaction:

$$Hg_2Cl_{2(s)} + 2\ e^- \leftrightarrow 2\ Hg_{(l)} + 2\ Cl^-_{(aq)} \text{ (saturated KCl solution)}$$

For the electrical circuit to be complete, current must flow from the working electrode to a separate electrode. Since reference electrodes are not ideally non-polarizable, substantial current passage through the reference will change the electrochemical properties from their literature values. To prevent this from occurring, a counter (or auxiliary) electrode is used through which the current will pass. The counter electrode is made of conductive, electrochemically inert material such as gold or platinum.

1.4.2. Electrochemical Methods

In this research, we employed two classical methods of electrochemical analysis: cyclic voltammetry (CV) and electrochemical impedance spectroscopy (EIS). Although both control voltage and measure resulting current, the two methods provide different information about the electrochemistry of the system being probed. In most cases, these two methods are complementary and provide further knowledge of reactions occurring at or near the working electrode/electrolyte interface. Perturbations in reduction or oxidation peaks of redox-active electrode material may indicate a change in chemistry from surface alterations, whereas perturbations in the impedance spectra may indicate differences in capacitance or resistance due to changes in the electrical double layer of a material that may or may not be electroactive.

1.4.2.1. Cyclic Voltammetry

Cyclic voltammetry is a method in which applied potential is swept at a fixed rate forward and backward over a voltage range while the resulting current is measured between the working and counter electrodes. The applied scan can be represented as a triangle wave in a graph of voltage (E) vs. time (t), with a slope of dE/dt as the applied scan rate. The measured current is represented by graph of current (I) or current density (J) versus the applied voltage (E). This method is often used in systems where there is electron transfer with reduction and/or oxidation of a species (the electrode material or an ion or molecule in solution in proximity to the electrode) resulting in current peaks in a cyclic voltammogram.

In a simple case, the voltage is swept cathodically from one potential to a lower potential, and electrons may move to reduce a solution species or film, allowing a reductive half reaction at the working electrode and a negative current. In the reverse scan, in which the voltage is

increased anodically back to the original, higher potential, electrons move back into the working electrode and the electroactive solution species or film is re-oxidized, producing a positive current. The magnitude of the current in a reversible redox reaction is proportional to the electroactive species concentration and to the square root of the voltage scan rate. In the general case of a quiescent, diffusion-controlled, fully reversible redox reaction of an ion or uncharged molecule in solution, the cathodic peak is equal in magnitude to the anodic peak, and the voltage at the half-point between the two peaks is E^0, the standard redox potential of the species in solution. However, non-Faradaic anodic and cathodic peaks can also be produced by ion adsorption and desorption in an applied voltage scan, as current itself is a due to a movement of charge with time. A change in solution pH may result in a change in cyclic voltammograms when a half-reaction requires an electron (in a Faradaic case) or when adsorption and desorption of protons or hydroxide anions produces current peaks (in either Faradaic or non-Faradaic cases). Specific adsorption of other ions on an electrode may also affect cyclic voltammograms by either blocking the electrode surface from electroactive species or causing more or less attraction of charged species that affect measured current.

1.4.2.2. Electrochemical Impedance Spectroscopy

Electrochemical Impedance Spectroscopy is a controlled voltage technique in which the voltage is sinusoidally swept with a small amplitude over a bias voltage over a frequency range several orders of magnitude (*e.g.*, 10^{-2} Hz – 10^5 Hz), to be measured against the resulting current wave. Impedance, **Z**, in an alternating current process is analogous to resistance in direct current, such that:

$$\text{DC:} \quad E = IR \tag{3}$$

$$\text{AC:} \quad \mathbf{E} = \mathbf{I} \cdot \mathbf{Z} \tag{4}$$

Where E, I, and R are time-independent voltage, current, and resistance respectively, and **E**, **I**, and **Z** are time-dependent voltage, current, and impedance. Both resistance and impedance are in units of ohms.

Impedance data is often plotted in Nyquist and Bode plots that provide different ways of examining the same experimental output. Nyquist plots show the negative imaginary impedance component versus the real component ($-Z_{imag}$ vs. Z_{real}) of time-dependent **Z**, where:

$$\mathbf{Z} = Z_{real} + jZ_{imag} \tag{5}$$

in which Z_{real} and Z_{imag} are the real and imaginary impedance components respectively and j is the imaginary unit equal to $\sqrt{-1}$.

Portrayal of impedance data in Nyquist plots is often used in analyzing conventional electric circuits and can assist in determining the characteristics of the edl of an electrode. Features can be fit to equivalent circuits with resistor and capacitor components, Warburg components related to porosity and diffusion, and constant phase elements. From an analysis of these circuit elements, we can gain some understanding of electrochemical properties of the electrode and its interaction with the solution species.

The other common method of analyzing the data are Bode plots that map either the magnitude of impedance |Z| or the phase angle of impedance (θ) vs. applied potential frequency

in Hz. The magnitude of the impedance and phase angle can be derived from the real and imaginary components of **Z**, where:

$$|Z| = \sqrt{{Z_{imag}}^2 + {Z_{real}}^2} \quad (6)$$

$$\theta = \tan^{-1}\frac{Z_{imag}}{Z_{real}} \quad (7)$$

Thinking of this a different way, |Z| is analogous to a radius from the (0,0) origin to a point on a Nyquist diagram, and θ is the angle of that radius from the x-axis. Nyquist plots have no inherent frequency information, and both Z_{real} and Z_{imag} are dependent variables determined from the experimental output. Bode plots present the impedance data in ways that incorporate applied frequency, an independent variable. The Bode phase plot in particular gives important information about the capacitive features of the electrode material and its interfacial chemistry. For an electrode in solution, a more capacitive measurement (indicated by a more negative θ) on a Bode phase plot may signal a different concentration of an ion adsorbed in the edl, as the electrochemical features of the surface are changed by adsorbed potential-determining anions. Perturbations in electrochemical features from ion adsorption can be analogous to measurable changes in the electrical characteristics of a circuit produced by altering charge at the two plates of a conventional capacitor.

1.5. Purpose of This Study

This work tests the hypothesis that perturbations in electrochemistry from the strong interactions between phosphate and metal (hydr)oxides can be correlated to phosphate

concentration in a way that is both selective and sensitive for this analyte. Nanoporous metal (hydr)oxide thin-film electrodes produced via sol-gel methods give a high surface area that amplify measurable changes in the electrical double layer of the electrode resulting from the adsorption of phosphate, a potentially determining ion. Findings from this research may be used to produce an *in situ* electrochemical sensor for phosphate in natural waters that may avoid complications arising from colorimetric reagent-based determination. Fundamentally, the hope is that this work will lead to a novel ion selective electrode for phosphate that would be a beneficial tool for environmental scientists, particularly those monitoring freshwater quality.

References

[1] Schindler, D. W. Eutrophication and recovery in experimental lakes: implications for lake management. *Science* **1974**, *184*, 897–899.

[2] Schindler, D. W.; Hecky, R.; Findlay, D.; Stainton, M.; Parker, B.; Paterson, M.; Beaty, K.; Lyng, M.; Kasian, S. Eutrophication of lakes cannot be controlled by reducing nitrogen input: results of a 37-year whole-ecosystem experiment. *Proceedings of the National Academy of Sciences* **2008**, *105*, 11254–11258.

[3] U.S. Environmental Protection Agency *Phosphorus Water Quality Standards Criteria Summaries: A Compilation of State/Federal Criteria*; Washington DC, 1988.

[4] Organisation for Economic Cooperation and Development *Eutrophication of Waters, Monitoring, Assessment and Control*; Paris, 1982.

[5] Hudson, J. J.; Taylor, W. D.; Schindler, D. W. Phosphate concentrations in lakes. *Nature* **2000**, *406*, 54–56.

[6] Koroleff, F. In *Methods of Seawater Analysis*; Grasshoff, K.; Ehrhardt, M.; Kremling, K., Eds.; Verlag Chemie: New York, 1983; pp. 126–129.

[7] Zhang, J. Z.; Chi, J. Automated analysis of nanomolar concentrations of phosphate in natural waters with liquid waveguide. *Environmental Science & Technology* **2002**, *36*, 1048–1053.

[8] Gimbert, L. J.; Haygarth, P. M.; Worsfold, P. J. Determination of nanomolar concentrations of phosphate in natural waters using flow injection with a long path length liquid waveguide capillary cell and solid-state spectrophotometric detection. *Talanta* **2007**, *71*, 1624–1628.

[9] Li, Q. P.; Hansell, D. A. Intercomparison and coupling of magnesium-induced co-precipitation and long-path liquid-waveguide capillary cell techniques for trace analysis of phosphate in seawater. *Analytica Chimica Acta* **2008**, *611*, 68–72.

[10] Patey, M. D.; Rijkenberg, M. J. A.; Statham, P. J.; Stinchcombe, M. C.; Achterberg, E. P.; Mowlem, M. Determination of nitrate and phosphate in seawater at nanomolar concentrations. *TrAC Trends in Analytical Chemistry* **2008**, *27*, 169–182.

[11] Karl, D. M.; Tien, G. MAGIC: A sensitive and precise method for measuring dissolved phosphorus in aquatic environments. *Limnology and Oceanography* **1992**, *37*, 105–116.

[12] Rimmelin, P.; Moutin, T. Re-examination of the MAGIC method to determine low orthophosphate concentration in seawater. *Analytica Chimica Acta* **2005**, *548*, 174–182.

[13] Anagnostou, E.; Sherrell, R. M. A MAGIC method for sub-nanomolar orthophosphate determination in freshwater. *Limnology and Oceanography: Methods* **2008**, *6*, 64–74.

[14] Wollenberger, U.; Schubert, F.; Scheller, F. W. Biosensor for sensitive phosphate detection. *Sensors and Actuators B: Chemical* **1992**, *7*, 412–415.

[15] Engblom, S. O. The phosphate sensor. *Biosensors and Bioelectronics* **1998**, *13*, 981–994.

[16] Stumm, W. *Chemistry of the Solid-Water Interface: Processes at the Mineral-Water and Particle-Water Interface in Natural Systems*; Jon Wiley Spms: New York, NY, 1992.

[17] Kosmulski, M. *Surface Charging and Points of Zero Charge*; CRC, 2009.

[18] Parks, G. A. In *Chemical Oceanography*; Riley, J. P.; Skirrow, G., Eds.; Academic Press: New York, 1975.

[19] Bowden, J. W.; Nagarajah, S.; Barrow, N. J.; Posner, A. M.; Quirk, J. P. Describing the adsorption of phosphate, citrate and selenite on a variable-charge mineral surface. *Soil Research* **1980**, *18*, 49–60.

[20] Hingston, F. J.; Atkinson, R. J.; Posner, A. M.; Quirk, J. P. Specific adsorption of anions. *Nature* **1967**, *215*, 1459–1461.

[21] Forbes, E.; Posner, A.; Quirk, J. The specific adsorption of divalent Cd, Co, Cu, Pb, and Zn on goethite. *European Journal of Soil Science* **1976**, *27*, 154–166.

[22] Yates, D.; Healy, T. Mechanism of anion adsorption at the ferric and chromic oxide/water interfaces. *Journal of Colloid and Interface Science* **1975**, *52*, 222–228.

[23] Parfitt, R. L.; Russell, J. D.; Farmer, V. C. Confirmation of the surface structures of goethite (α-FeOOH) and phosphated goethite by infrared spectroscopy. *Journal of the Chemical Society, Faraday Transactions* **1976**, *72*, 1082–1087.

[24] Hansmann, D. D.; Anderson, M. A. Using electrophoresis in modeling sulfate, selenite, and phosphate adsorption onto goethite. *Environmental Science & Technology* **1985**, *19*, 544–551.

[25] Tejedor-Tejedor, M. I.; Anderson, M. A. Protonation of phosphate on the surface of goethite as studied by CIR-FTIR and electrophoretic mobility. *Langmuir* **1990**, *6*, 602–611.

[26] Nilsson, N.; Lövgren, L.; Sjöberg, S. Phosphate complexation at the surface of goethite. *Chemical Speciation and Bioavailability* **1992**, *4*, 121.

[27] Antelo, J.; Avena, M.; Fiol, S.; López, R.; Arce, F. Effects of pH and ionic strength on the adsorption of phosphate and arsenate at the goethite-water interface. *Journal of Colloid and Interface Science* **2005**, *285*, 476–486.

[28] Breeuwsma, A.; Lyklema, J. Physical and chemical adsorption of ions in the electrical double layer on hematite (α-Fe_2O_3). *Journal of Colloid and Interface Science* **1973**, *43*, 437–448.

[29] Daou, T. J.; Begin-Colin, S.; Grenèche, J. M.; Thomas, F.; Derory, A.; Bernhardt, P.; Legaré, P.; Pourroy, G. Phosphate adsorption properties of magnetite-based nanoparticles. *Chemistry of Materials* **2007**, *19*, 4494–4505.

[30] Arai, Y.; Sparks, D. L. ATR-FTIR spectroscopic investigation on phosphate adsorption mechanisms at the ferrihydrite-water interface. *Journal of Colloid and Interface Science* **2001**, *241*, 317–326.

[31] Appenzeller, B. M. R.; Duval, Y. B.; Thomas, F.; Block, J. C. Influence of phosphate on bacterial adhesion onto iron oxyhydroxide in drinking water. *Environmental Science & Technology* **2002**, *36*, 646–652.

[32] Anderson, M. A.; Malotky, D. T. The adsorption of protolyzable anions on hydrous oxides at the isoelectric pH. *Journal of Colloid and Interface Science* **1979**, *72*, 413–427.

[33] Feiler, A.; Jenkins, P.; Ralston, J. Metal oxide surfaces separated by aqueous solutions of linear polyphosphates: DLVO and non-DLVO interaction forces. *Physical Chemistry Chemical Physics* **2000**, *2*, 5678–5683.

[34] Rigney, M.; Funkenbusch, E.; Carr, P. Physical and chemical characterization of microporous zirconia. *Journal of Chromatography A* **1990**, *499*, 291–304.

[35] Atkinson, R. J.; Parfitt, R. L.; Smart, R. S. C. Infra-red study of phosphate adsorption on goethite. *Journal of the Chemical Society, Faraday Transactions 1* **1974**, *70*, 1472.

[36] Russell, J. D.; Parfitt, R. L.; Fraser, A. R.; Farmer, V. C. Surface structures of gibbsite goethite and phosphated goethite. *Nature* **1974**, *248*, 220–221.

[37] Hiemstra, T.; Van Riemsdijk, W. H. A surface structural approach to ion adsorption: the charge distribution (CD) model. *Journal of Colloid and Interface Science* **1996**, *179*, 488–508.

[38] Persson, P.; Nilsson, N.; Sjoberg, S. Structure and bonding of orthophosphate ions at the iron oxide-aqueous interface. *Journal of Colloid and Interface Science* **1996**, *177*, 263–275.

[39] Geelhoed, J. S.; Hiemstra, T.; Van Riemsdijk, W. H. Phosphate and sulfate adsorption on goethite: Single anion and competitive adsorption. *Geochimica et Cosmochimica Acta* **1997**, *61*, 2389–2396.

[40] Dimirkou, A.; Ioannou, A.; Doula, M. Preparation, characterization and sorption properties for phosphates of hematite, bentonite and bentonite-hematite systems. *Advances in Colloid and Interface Science* **2002**, *97*, 37–60.

[41] Rahnemaie, R.; Hiemstra, T.; van Riemsdijk, W. H. Geometry, charge distribution, and surface speciation of phosphate on goethite. *Langmuir* **2007**, *23*, 3680–3689.

[42] Liu, H.; Sun, X.; Yin, C.; Hu, C. Removal of phosphate by mesoporous ZrO_2. *Journal of Hazardous Materials* **2008**, *151*, 616–622.

[43] Huang, X.; Foster, G. D.; Honeychuck, R. V.; Schreifels, J. A. The maximum of phosphate adsorption at pH 4.0: why it appears on aluminum oxides but not on iron oxides. *Langmuir* **2009**, *25*, 4450–4461.

[44] Ioannou, A.; Dimirkou, A. Phosphate adsorption on hematite, kaolinite, and kaolinite-hematite (kh) systems as described by a constant capacitance model. *Journal of Colloid and Interface Science* **1997**, *192*, 119–128.

[45] Elzinga, E. J.; Sparks, D. L. Phosphate adsorption onto hematite: An in situ ATR-FTIR investigation of the effects of pH and loading level on the mode of phosphate surface complexation. *Journal of Colloid and Interface Science* **2007**, *308*, 53–70.

[46] Moss, R. E.; Jackowski, J. J.; de Souza Castilho, M.; Anderson, M. A. Development and evaluation of a nanoporous iron (hydr)oxide electrode for phosphate sensing. *Electroanalysis* **2011**, *23*, 1718–1725.

[47] Kosmulski, M. Compilation of PZC and IEP of sparingly soluble metal oxides and hydroxides from literature. *Advances in Colloid and Interface Science* **2009**, *152*, 14–25.

[48] Xu, Q. Physical-chemical factors affecting the synthesis and characteristics of transition metal oxide membranes, University of Wisconsin-Madison: Madison, WI, 1991.

[49] Zacharaki, I.; Kontoyannis, C.; Lycourghiotis, A.; Kordulis, C. The influence of calcination on the size of nanocrystals, porous structure and acid-base properties of mesoporous anatase used as catalytic support. *Colloids and Surfaces A: Physicochemical and Engineering Aspects* **2008**, *324*, 208–216.

[50] Georgiadou, I.; Spanos, N.; Papadopoulou, C.; Matralis, H.; Kordulis, C.; Lycourghiotis, A. Preparation and characterization of various titanias (anatase) used as supports for vanadia-supported catalysts. *Colloids and Surfaces A: Physicochemical and Engineering Aspects* **1995**, *98*, 155–165.

[51] Kosmulski, M. The significance of the difference in the point of zero charge between rutile and anatase. *Advances in Colloid and Interface Science* **2002**, *99*, 255–264.

[52] Soled, S.; McVicker, G. B. Acidity of silica-substituted zirconia. *Catalysis Today* **1992**, *14*, 189–194.

[53] Ardizzone, S.; Bianchi, C. L.; Galassi, C. Chromium doped γ-Al_2O_3 powders. Features of the electrical double layer and state of the surface species. *Journal of Electroanalytical Chemistry* **2000**, *490*, 48–53.

[54] Lee, B.; Hench, L. Electrophoretic behavior and surface reactions of sol-gel derived alumina. *Colloids and Surfaces* **1989**, *23*, 211–229.

Tables

Table 1.1 Isoelectric pH values of oxide materials referenced in this work

Oxide type	Phase	pH_{iep}	Notes
Iron (hydr)oxides	α-FeO(OH) (goethite) sol colloids	7.8	a
	α-FeO(OH) sol calcined at 400˚C	8.1	b
	Ferrihydrite	7.6 ± 0.6	c
	Goethite	8.6 ± 0.8	d
	Hematite	7.4 ± 1.4	c
Titania	TiO_2 sol colloids	4.5	e
	TiO_2 sol calcined at 500˚C	6.6 ± 0.1	f
	Anatase	5.9 ± 1.0	g
	Rutile	5.4 ± 0.5	g
Zirconia	ZrO_2 sol colloids	6.6	h
	ZrO_2 sol calcined at 500˚C	7.3	i
	monoclinic ZrO_2	6.6 ± 1.1	c
	tetragonal ZrO_2	7.5 ± 0.9	j
Alumina	δ-AlOOH (boehmite) sol colloids	8.6	k
	δ-AlOOH sol calcined at 500˚C	8.5	l
	synthetic γ-Al_2O_3 and δ-Al_2O_3	9.2 ± 0.6	c

a. Prepared by neutralization of $Fe(NO_3)_3$ solution at room temperature, own work [46]

b. 400˚C calcination of goethite sol, hematite structure, own work

c. Synthetic sample data [47]

d. Average value from compilation of synthetic FeO(OH) samples prepared by Atkinson method [47]

e. Prepared from titania isopropoxide [48]

f. 500˚C calcination of TiO_2 sol prepared from titania isopropoxide, anatase/rutile structure [49, 50]

g. Average value from compilation of synthetic sample data [51]

h. Prepared from zirconium propoxide [48]

i. 500˚C calcination of ZrO_2 sol prepared from zirconium propoxide, tetragonal/monoclinic structure. [52]

j. Mean value from compilation of tetragonal ZrO_2 isoelectric pH data [17]

k. Boehmite sol prepared from aluminum tri-sec-butoxide (ATSB) [53]

l. 500˚C calcination of boehmite sol prepared from ATSB, γ-Al_2O_3 / δ-Al_2O_3 structure [54]

Figures

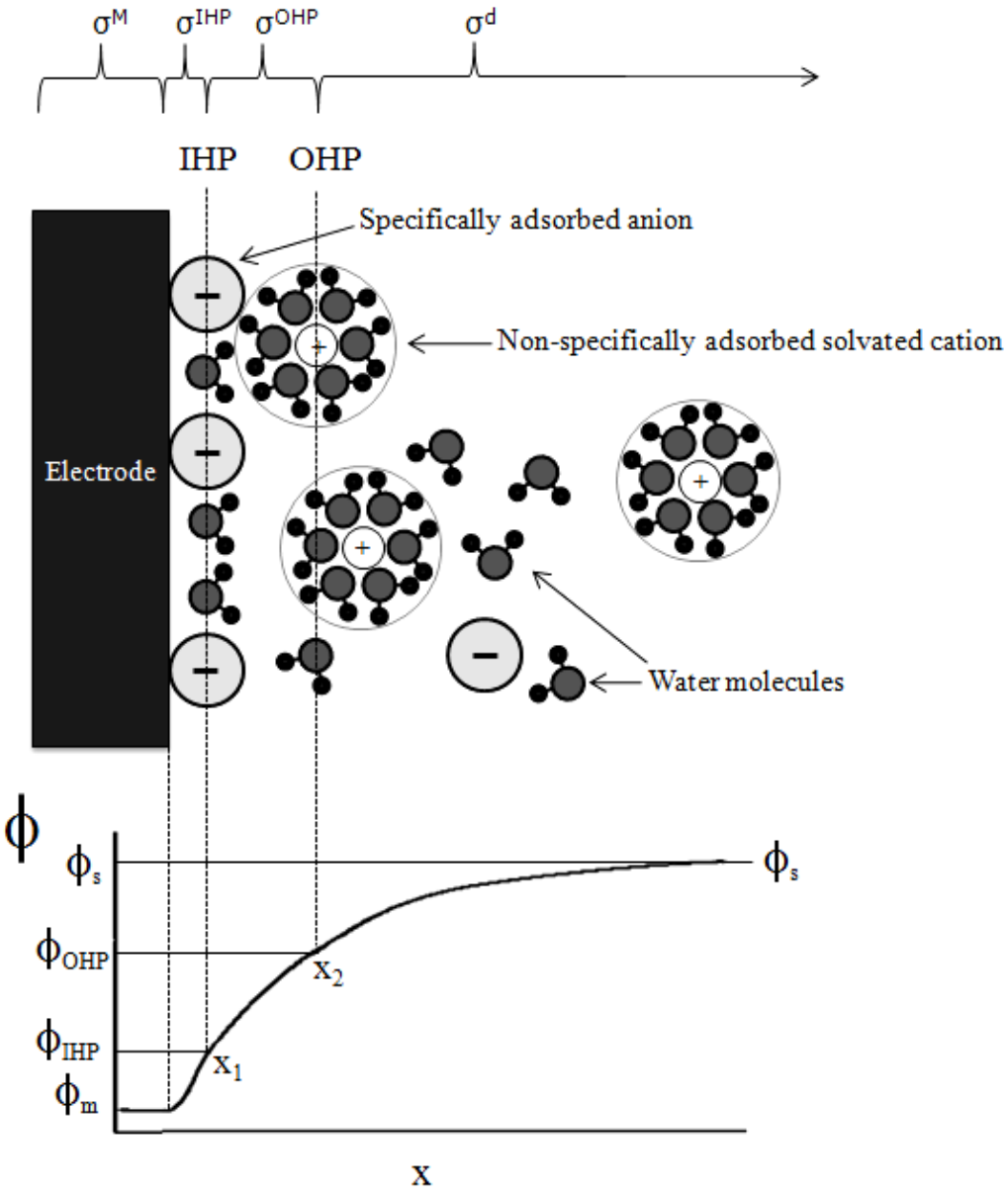

Figure 1.1 Diagram of the electrical double layer (edl) of a positively charged oxide electrode with associated potential Φ at function of distance x from the surface

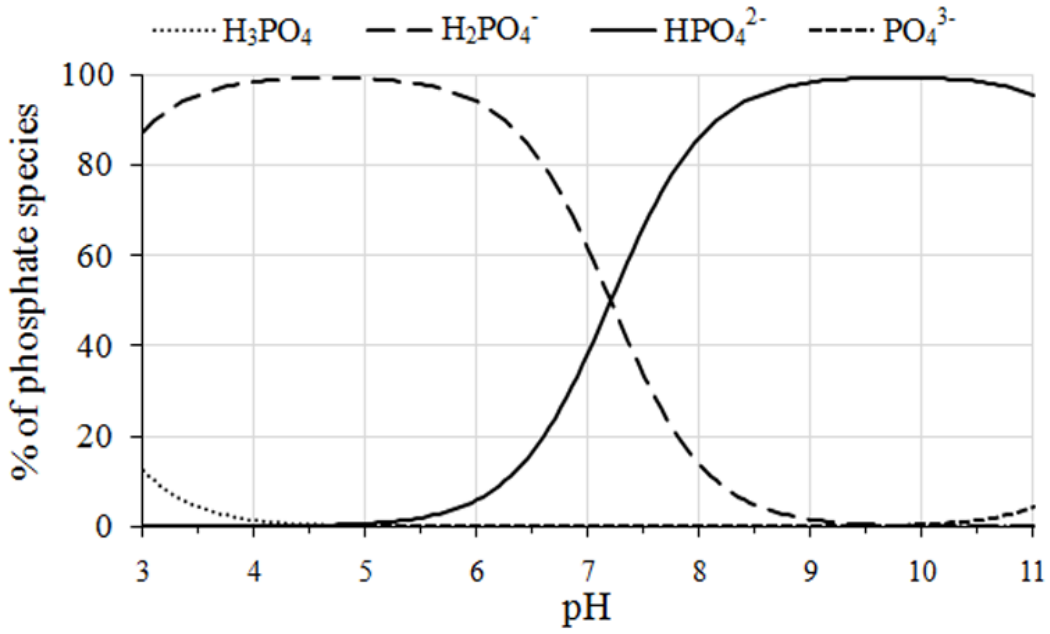

Figure 1.2 Speciation of orthophosphate over pH range 3 – 11.

CHAPTER 2

DEVELOPMENT AND EVALUATION OF A NANOPOROUS IRON (HYDR)OXIDE ELECTRODE FOR PHOSPHATE SENSING*

* A version of this chapter is published in *Electroanalysis* (2011), vol. 23(7), pp. 1718–1725, with J. J. Jackowski, M. de Souza Castilho, and M. A. Anderson as coauthors.

Abstract

Nanoporous iron (hydr)oxide electrodes were evaluated as sensitive and selective phosphate sensors using cyclic voltammetry (CV) and electrochemical impedance spectroscopy (EIS). The intensity of the anodic scan peak current (I_{ap}) of the ferrihydrite working electrode was tied to phosphate concentration at low pH. At both low and neutral pH, a hematite electrode combined with the use of EIS provided reliable sensing data for submicromolar phosphate. Nanoporous hematite working electrodes produced an impedance phase component (θ) that shifted to more capacitive values with increasing phosphate. At chosen frequencies, θ values were fitted for the range 1 nM to 0.1 mM phosphate at pH 4 and pH 7 in 5 mM $NaClO_4$, and at pH 7 in simulated lake water solution.

2.1. Introduction

The importance of phosphorus as the limiting nutrient in aquatic systems was first documented in whole lake fertilization experiments conducted by Schindler in the Ontario Experimental Lakes Area [1]. Subsequent regression analyses for other freshwater bodies from around the world showed that phosphorus loading accounted for 80% of the variance in annual

chlorophyll [2]. Excess phosphorus can lead to undesired growth of algae and other aquatic vegetation, ultimately causing the eutrophication of natural water bodies. The most readily bio-available forms of phosphorus are orthophosphates (primarily $H_2PO_4^-$ and HPO_4^{2-} in the pH range of natural waters). Currently, the most common method of phosphorus analysis depends on the conversion of various forms of phosphorus to orthophosphate with subsequent colorimetric analysis [3, 4]. This form of phosphorus analysis can be extremely time-consuming and labor intensive, and it is normally performed in a laboratory setting. The development of an *in situ* electrochemical phosphate sensor would allow for near-instantaneous measurements in freshwater, sea water, or other environmental matrices, making analysis more convenient and less expensive. A "real-time" sensor would allow for the synchronization of phosphate monitoring data with transient weather events and would facilitate rapid feedback for phosphate control strategies in farming, wastewater treatment, and industrial applications.

Due to the importance of the orthophosphate ion in the protection of the global environment, there has been accelerating progress in the development inorganic-based ion-selective phosphate sensors [5-12], as summarized most recently by Engblom [13]. The detection limit of these electrodes is typically around 1 - 10 μM, which is too high to be of use in water quality studies [14]. Using another approach, biosensors have also been developed to measure phosphate levels [13, 15]. It is apparent that these electrode sensors were designed to study biological systems rather than natural waters. Furthermore, these sensors are not as stable as their inorganic counterparts. To the best of our knowledge, there are no commercially available phosphate sensors employing any of the ion-selective or biosensor mechanisms.

Electrochemical sensors are an attractive option for detecting and measuring phosphate in aqueous media. The phosphate species themselves are electroinactive (*i.e.*, the ions themselves

do not undergo reduction and oxidation from changed potential), but inner-sphere adsorption to an electrode surface may perturb electrochemical response to an extent indicated by phosphate concentration. Sensitivity should be increased by choosing an appropriate electrode material and expanding the surface area onto which the analyte can specifically adsorb. In this case, phosphates specifically adsorb to iron (hydr)oxides with a high affinity and as potential-determining anions [16, 17]. To enhance surface area, electrodes can be fabricated via sol-gel methods to have thin-film ceramics on a conducting substrate. These films can have extensive surface area due to great nanoporosity, with a high density of micropores (less than 2 nm in diameter) and mesopores (2 – 50 nm in diameter). The high exposed surface area allows easy contact with the analyte. Nanoporous iron hydr(oxide) materials prepared from calcined xerogels have been studied extensively in this lab [18, 19], but their potential as an active surface for a sensing electrode was previously unknown.

Sensors and biosensors that use amperometric techniques have been used to detect a wide array of environmentally relevant gases such as NO [20], NO_2 [20, 21], SO_2 [22], and O_3 [23] to ppb levels, and aqueous glucose [24-26], lactate [26], and H_2O_2 [27], to submicromolar concentrations. Perturbation of impedance as an electroanalytical measurement technique has not been as extensively explored. Impedance changes can be interpreted using Nyquist plots of the imaginary and real components of impedance, and Bode plots, portraying the phase angle θ or the magnitude of impedance as a function of applied frequency of sinusoidal voltage. Janek et al. (1997) [28] found the Nyquist plots of gold electrodes modified with self-assembled monolayers (SAMs) changed as a function of $NaClO_4$ concentration. Several biosensors using impedance spectroscopy are described in a review by Berggren et al. (2000) [29].

Perchlorate (ClO_4^-) has been found to be an anion inert to metal (hydr)oxide surfaces, in that it has the least effect on the isoelectric pH or infrared spectra even at high concentrations [30-35]. Experiments of phosphate in this electrolyte are expected then to produce results indicative of electrochemical perturbation due only to specifically adsorbing phosphate, protons, and hydroxide. However, perchlorate is not a typical ion in lake water. The investigation of the effects of naturally occurring ions on electrochemical phosphate sensing is essential to the development of a sensor for real-world scenarios. Some ions found in natural waters can enter into the electrical double layer of metal oxides and may interfere with phosphate adsorption. Sodium, calcium, and potassium cations generally will not have a concentration-dependent effect on the isoelectric pH of these materials [35], although calcium phosphate may precipitate on goethite in basic solutions with high concentrations of both Ca^{2+} and PO_4^{3-} [36]. Chloride and nitrate generally have nonspecific, outer-sphere interactions with metal (hydr)oxides, as determined by electrophoretic mobility experiments [34, 37-42]. Sulfate (SO_4^{2-}) and carbonates (HCO_3^- and CO_3^{2-}), in contrast, may be specifically adsorbing and may then compete with phosphate on a metal oxide surface. Sulfate adsorption has been proposed as an outer-sphere mechanism on aluminum and iron (hydr)oxides from salt effect studies [33, 43, 44], but adsorption of sulfate has been concluded to be inner-sphere based on others' spectroscopic findings [45, 46]. Eggleston et al. (1998) [47] found evidence that sulfate on goethite is a spectrum of inner-sphere and outer-sphere adsorption behavior, while Peak et al. (1999) [48] found both processes but a predominant outer-sphere adsorption above pH 6. Regardless of the sulfate adsorption mechanism on metal oxides, phosphate still is strongly preferred over sulfate. Above pH 6, a sulfate concentration 48 times greater than phosphate was found to have no detectable effect on phosphate adsorption on goethite compared to a sulfate-free system [49].

Carbonates are believed to have a mix of inner-sphere and outer-sphere adsorption on goethite [50], although high carbonate concentrations are also required to compete with phosphate. Rahnemaie et al. (2007) [50] found that at pH 8, a solution of initially 30 mM carbonate and 0.4 mM phosphate reduced phosphate adsorption by 2.8% compared to a carbonate-free system. As the sum of carbonate and bicarbonate concentration in lakes is generally on the order of 1 mM, these ions may be the most likely to alter an electrochemical signal that results from phosphate adsorbed on metal oxide surfaces. The effects of all of these interfering ions should be taken into account for a proposed sensor.

This work investigated the perturbation of impedance as well as perturbations of cyclic voltammograms of an iron hydr(oxide) thin-film electrode upon addition of phosphate. Electrochemical analysis of the nanoporous iron oxide electrode in perchlorate electrolyte showed a correlation between phosphate and impedance. These correlations were also found to occur also in artificial lake water. These findings may contribute to the development of a new ion selective electrode (ISE) system for phosphate that can detect levels typical for natural waters that can be three orders of magnitude lower in concentration than the detection limits of electrochemical phosphate sensors developed to date.

2.2. Experimental

2.2.1. Iron (Hydr)oxide Electrode Synthesis

Electrode materials for the electrochemical phosphate sensor were prepared by dip-coating 0.50 mm thick 99.0% nickel foil substrate in an aqueous colloidal suspension (sol) of nanoparticulate α-FeOOH (goethite). The hydrated iron oxide sol was synthesized from $Fe(NO_3)_3 \cdot 9H_2O$ and $NaHCO_3$ precursors and concentrated to 40 $g \cdot L^{-1}$ using the method

developed in this laboratory from Machesky and Anderson (1986) [51], according to the procedure in Atkinson et al. (1968) [52]. The FeOOH material has an isoelectric pH of 7.8, and the mean particle size is 26.2 nm (Malvern Zetasizer 3000). Before coating, a 1 cm by 5 cm strip of Ni foil was sanded with 600 grit sandpaper, cleaned with 0.1 M NaOH and 18 MΩ·cm ultrapure water, then was placed in a 2% HNO_3 solution for 10 minutes to oxidize the substrate surface and again rinsed with ultrapure water.

Two types of iron (hydr)oxide thin-film electrodes were prepared and used in our electrochemical experiments. The first electrode, Electrode A, was prepared by dipping the oxidized Ni foil substrate into the FeOOH sol three times, withdrawing at a speed of 5.0 $mm \cdot s^{-1}$ and allowing a 1 hour drying period at 80°C between coats. The dip-coated electrode was then fired at 300°C for 1 hour to sinter the iron nanoparticle coating into a thin-film ceramic on the Ni foil support. The second electrode, Electrode B, required the cleaned and oxidized Ni foil to be heated at 300°C for 2.5 hours before coating to improve Ni substrate wettability prior to dipping in the FeOOH sol. This second electrode was withdrawn from the sol at 5.0 $mm \cdot s^{-1}$, allowed to air-dry for 2 min, then dipped and withdrawn again to a total of ten coats. The film was sintered onto the Ni substrate by firing at 400˚C for 10 hours. The pore size distribution and specific surface area of ceramics fired at 300˚C and 400˚C were determined from the N_2 adsorption isotherms at 77 K using a Micromeritics ASAP 2010 analyzer. Surface densities of Fe on the electrodes (in $g \cdot cm^{-2}$) were determined by dissolving coatings in 50% HNO_3 for 2 hours, then testing for Fe using Inductively Coupled Plasma Optical Emission Spectrometry (ICP-OES). Removal of Fe as an impurity from the uncoated Ni backing by this acid treatment process was negligible. Film thickness for Electrodes A and B were estimated from Fe surface density values, the chemical formula for goethite and/or hematite, and porosity. Crystal structures of the

ceramics produced from FeOOH sol fired at the two temperatures were characterized on a STOE Bragg–Brentano X-Ray Diffractometer.

2.2.2. Chemicals

Aqueous solutions of orthophosphates were prepared with H_3PO_4, NaH_2PO_4, and/or Na_2HPO_4, by serial dilution in a series of carefully pre-cleaned volumetric flasks and were titrated to pH 4 or pH 7 with microliter quantities of 0.1 M solutions of ACS analytical grade NaOH and $HClO_4$. Highly pure HPLC grade $NaClO_4$ was added to a final concentration of 5 or 10 mM to maintain uniform ionic strength for solutions in the 10^{-9} M to 10^{-4} M phosphate range. 10^{-4} M phosphate solutions in 0.01 M $NaClO_4$ have an ionic strength 0.99% greater (pH 4) or 1.6% greater (pH 7) or due the contribution of the phosphate ion. Ionic strengths in the 0.005 – 0.010 range are typical of those found in hard lakewater [53]. Arsenate solutions were similarly produced with Na_2HAsO_4 at 10^{-9} M to 10^{-4} M concentration in 5 mM $NaClO_4$, adjusted to pH 7. Solutions were stored in new HDPE containers pre-cleaned for analytical use.

A phosphate-free synthetic lakewater recipe was adapted from Smith (2002) [54], made from a 100x stock solution of $MgCl_4 \cdot 6H_2O$, $CaCl_2 \cdot 6H_2O$, and $Ca(NO_3)_2 \cdot 4H_2O$, a 100x stock solution of Na_2SO_4, $KHCO_3$, and Na_2CO_3, and a 1.1x solution of $CaCO_3$. Final concentrations of cations were 250 μM Na^+, 25.0 μM K^+, 945 μM Ca^{2+}, and 59.9 μM Mg^{2+}. Final concentrations of anions were 279 μM Cl^-, 30.0 μM NO_3^-, 115 μM SO_4^{2-}, and a sum 895 μM for the sum of HCO_3^- and CO_3^{2-}. The ionic strength of this solution is 0.004, within the ionic strength range typically found in lakes. Listed specifications for high-purity chemicals used in these experiments would give a maximum final phosphate concentration in the low nanomolar range for the “phosphate-free” lake water blank.

2.2.3. Apparatus and Electroanalytical Procedure

A typical three electrode electrochemical cell was used that consisted of the thin-film metal (hydr)oxide electrode as the working electrode in electrolyte solution along with a saturated calomel electrode (SCE) as the reference and a Pt counter electrode. Cyclic voltammetry (CV) and electrochemical impedance spectroscopy (EIS) techniques utilize a Princeton Applied Research VMP2-Z potentiostat with starting parameter inputs and data analysis using EC-Lab software.

In cyclic voltammetry experiments, the potential was scanned over a voltage window in which there was consistently a peak in the anodic scan at pH 4. Using Electrode A, cyclic voltammograms of prepared electrolyte solutions were obtained using a scan rate of 100 $mV \cdot s^{-1}$ over -0.2 V – 0.8 V vs. SCE in 0.01 M sodium perchlorate and concentrations of 10^{-9} M, 10^{-8} M, 10^{-7} M, 10^{-6} M, 10^{-5} M, and 10^{-3} M phosphate. Results from the CV experiments were statistically analyzed for phosphate sensitivity using multiple regression analysis and for phosphate selectivity using analysis of variance (SYSTAT software). Cyclic voltammetry was also used to contrast the coating stability of Electrodes A and B in 10^{-3} M phosphate at pH 4 by comparing the decrease in anodic peak current over several hundred voltage cycles.

The electrochemical impedance spectroscopy (EIS) experimental technique applied to the electrode/analyte system a sinusoidal potential over a chosen frequency range around one bias voltage or several bias voltage steps. In each phosphate solution, the extent the current leads or lags the voltage at an applied frequency was given in terms of the complex impedance **Z** and its components. EIS experiments to determine a relationship between impedance results and phosphate concentration were performed at pH 4 and pH 7. Electrode B was placed in 150 mL of 5 mM $NaClO_4$ electrolyte solution at the chosen pH and underwent 250 CV redox cycles in the

-0.3 – 0.8 V vs. SCE window at 150 $mV \cdot s^{-1}$ in order to clean the surface of the electrode of nonspecifically adsorbed ions. Impedance measurements were taken at stepped bias voltages in the -0.3 – 0.0 V vs. SCE range with sinus amplitude of 20 mV at frequencies 200 kHz to as low as 10 mHz, with data taken at 20 points per decade. The electrolyte solution was then replaced with 10^{-9} M phosphate and 25 CV redox cycles were applied to the system to clean the working electrode surface. Following the cleaning procedure, impedance results were measured at that concentration over the same voltage steps and frequencies. This sequence was repeated for 10 more solutions increasing concentration in half-log units to a maximum 10^{-4} M phosphate. Data were reported for the bias voltages that gave impedance features evaluated to have the greatest correlation with phosphate concentration.

In experiments testing electrochemical response of hematite electrode in simulated lake water, the iron oxide electrode tested was initially placed in 250 mL phosphate-free simulated lake water at pH 7. The potential was cycled 200 times over a -0.3 V – 0.8 V vs. SCE voltage window. The system was left at rest for 2 min, and then the potential was cycled again five times. The impedance response was measured with the same parameters as in the perchlorate experiments. Then, 252 µL of 10^{-6} M phosphate in simulated lakewater was added to the 250 mL blank, the solution was stirred with a Teflon magnetic stir bar, and 252 µL is removed, producing 250 mL of 10^{-9} M phosphate in simulated lake water solution. The solution was titrated back to pH 7 with NaOH and $HClO_4$. The electroanalytical steps were repeated at 10^{-9} M phosphate, and then 540 µL of 10^{-6} M phosphate in simulated lake water was added, the total solution is mixed, and 540 µL is removed leaving 250 mL of a $10^{-8.5}$ M phosphate solution, which was titrated to pH 7. The steps were repeated with more concentrated stock phosphate solutions to raise the

phosphate concentration for the electrochemical analysis in half-log units to a final phosphate concentration of 10^{-4} M.

2.3. Results and Discussion

2.3.1. Electrode characterization

X-ray diffraction (XRD) spectra of unsupported sol samples fired at the same conditions as the coatings confirmed the Electrode A film to be an amorphous six-line ferrihydrite, while the Electrode B thin-film was identified as hematite (α-Fe_2O_3) (Figure 2.1). FeOOH sol produced by this Fe(III)-nitrate method has been shown to produce six-line ferrihydrite at drying above 110˚C and undergoes dehydration/dehydroxylation and structural transformation to hematite upon thermal treatments above 300˚C [55].

BET experimental analyses showed an average pore diameter of 35.6 Å with 90% of pores between 13.6 and 63.4 Å for the micro- and mesoporous ferrihydrite prepared material, and a greater average pore diameter of 68.4 Å (90% range 37.5 – 88.1 Å) for mesoporous hematite prepared material. The intra-agglomerate porosity of ferrihydrite coating was high, estimated to be between 50.3% and 55.5% by volume based on BET data and the densities of the goethite starting material (4.27 $g \cdot cm^{-3}$) and hematite (5.26 $g \cdot cm^{-3}$). A lesser 32.3% porosity was calculated for the hematite material. An earlier study of this sol [18] showed a similar increase in pore radius and a decrease in porosity between the xerogel material thermally treated at 300°C and 400°C.

The specific surface areas for the two electrodes' coatings differed substantially, as the Electrode A material was found to be 267 $m^2 \cdot g^{-1}$ and Electrode B was only 37.0 $m^2 \cdot g^{-1}$; however, the low surface area for the 400˚C thermally treated material was consistent with the results of

the earlier study of this sol [18]. The thicknesses of the coatings, estimated from iron content of dissolved coatings and from BET analyses, were between 7.6 μm (if pure goethite) and 10.3 μm (if pure hematite) for Electrode A, and 5.8 μm +/- 0.6 μm for (hematite) Electrode B. The number of dip-coats was not observed to be a great factor in film thickness for the hematite electrodes, but a greater number of dips in the sol did yield a visibly more uniform final coat, and, more importantly, CV results also showed more dip-coating led to less susceptibility for iron oxide film loss after potential cycling at pH 4.

2.3.2. Stability of Electrode Coating with Potential Cycling

When placed in a 0.01 M pH 4 $NaClO_4$ solution, both Electrode A and Electrode B produced a prominent CV anodic (positive current) peak in the scan to positive voltage. We used sodium perchlorate as the initial ionic strength buffer due to the fact that the perchlorate oxyanion has been shown to have minimal propensity for specific adsorption to iron (hydr)oxides compared to other commonly used background electrolytes (*e.g.*, Cl^-, NO_3^-, and SO_4^{2-}) [30, 33-34, 56] (in which we also observed the prominent anodic peak). The reduction of ClO_4^- is kinetically negligible at this pH and voltage range [57].

The addition of 10^{-3} M phosphate increased the anodic peak current (I_{ap}) and shifted upward the potential of the anodic peak. These changes in the reduction features of a cyclic voltammogram were more pronounced using Electrode A, with its much greater surface area. However, the intensity of the anodic peak decreased as the iron oxide film decayed with hundreds of CV cycles.

A slower decay of I_{ap} with continued CV cycling indicated a more stable electrode coating. A comparison of I_{ap} of the two electrodes (Figure 2.2) indicated that the ferrihydrite

coating material (Electrode A) lost its intensity with fewer cycles than hematite material (Electrode B). This finding was consistent with the results of a study by Grygar (1995) [58] that showed that the rate of electrochemically enhanced dissolution of ferrihydrite was two orders of magnitude greater than that of hematite at -0.2 V vs. SCE in slightly acid medium. The much greater solution-exposed surface area of the Electrode A coating may also be contributing to an increased rate of dissolution.

Electrode A kept within 2.0% of its maximum anodic peak current for the first 120 voltage cycles, although after 1000 cycles, it has lost 42% of the original signal with no clear asymptote. Electrode B was more stable to voltage cycling, losing only 3.0% of its maximum signal after 1000 cycles, and 8.1% loss after 1500 cycles; however, it took an initial 200-300 cycles to reach a maximum peak current. The requirement for several voltage scans before attaining a maximum I_{ap} occurs frequently in cyclic voltammetry and can generally be attributed the clearing of other molecules, including contaminants, at the electrical double layer of the material [59]. A series of CV cycles used to remove impurities at this interface has been described as “activating” the electrode [60].

2.3.3. Electrochemical Analysis of Phosphate Using Cyclic Voltammetry

The magnitude of I_{ap} was amperometrically tied to phosphate concentration. Experiments at pH 4 showed the strongest correlation between I_{ap} and phosphate level. In cyclic voltammograms, Electrode A displayed an anodic peak current intensity that could be fitted to concentration over six orders of magnitude, from 10^{-9} to 10^{-3} M phosphate (Figure 2.3) with $R^2 = 0.999$, using a power function of negative log of molar phosphate concentration, or p(phosphate).

$$\mathbf{I_{ap}} = \boldsymbol{a} \cdot (-\mathbf{log}\,([\mathbf{phosphate}])^{-\mathbf{2}} + \boldsymbol{b} \quad (1)$$

where I_{ap} was the anodic peak current in mA, and *a* and *b* were constants that depended on variables in electrode composition (*e.g.*, minor differences in film thickness).

Although this electrode showed evidence of sensitivity to nanomolar phosphate concentration, the peak current measurement from the erosion of the coating over continued voltage cycling indicated that this may not be a good sensor for more than a small amount of data collection, particularly when I_{ap} values were very similar for submicromolar levels. An attempt to fit I_{ap} to phosphate concentration to (1) using the more redox stable Electrode B (Figure 2.4) also gave a good correlation ($R^2 = 0.977$) but resulted in "*a*" and "*b*" parameters 1 - 2 orders of magnitude less than what was previously found for Electrode A. This was likely due to lesser porosity and greater pore diameters for Electrode B (hematite), since current produced at the working electrode was directly proportional to electrode surface area [61, 62]. Electrode B did not provide a large enough difference in peak intensity to reliably distinguish phosphate concentrations below micromolar concentrations, even at greater potential scan rates. In short, in order to measure phosphate at concentrations under 10^{-3} M as a perturbation of the peak features of a cyclic voltammogram, an electrode coated using these methods can be extremely sensitive to phosphate or exceptionally stable to voltage cycling, but not both. Thus, cyclic voltammetry may not be the best choice as the sole technique of a pH 4 phosphate sensor using these iron (hydr)oxide coatings.

At circumneutral pH, cyclic voltammetry was no longer a viable option for phosphate sensing with these electrodes. Using the ferrihydrite electrode, a positive correlation between

phosphate level and I_{ap} had been found to occur in solutions at pH 4.0, 5.5, 7.0, and 8.5, even as the primary orthophosphate species shifted over this range from $H_2PO_4^-$ to HPO_4^{2-}. However, the sensitivity of the electrode using this method was decreased with increasing pH. At pH 7, cyclic voltammograms no longer gave enough of a peak difference among submicromolar phosphate concentrations for the more sensitive ferrihydrite electrode response to be calibrated to (1) with much confidence.

The adsorption of phosphate onto iron (hydr)oxide is known to affect the zeta (ζ) potential (the potential at the sheer plane, used as one measure of surface charge) [63], with the result of increased acidity at the oxide surface. Phosphate specifically adsorbs to iron hydr(oxides) as a "potential-determining ion" [64], and addition of low (micromolar) phosphate has been found to shift the isoelectric pH of an iron hydr(oxide) several pH units downward [42, 63]. Small changes in concentration of inert (*i.e.*, non-specifically adsorbing) anions such as ClO_4^-, Cl^-, and NO_3^- did not produce this effect. The finding that I_{ap} was increased both by a more acid electrolyte solution and a greater phosphate concentration supported a theory that specific adsorption of anions and protons at the electric double layer played a significant role in signal perturbation.

2.3.4. Electrochemical Analysis of Phosphate Using Electrochemical Impedance Spectroscopy

EIS experiments gave different information about the hematite electrode in phosphate solutions. Specific adsorption of the phosphate anion to the hematite coating likely changed the double layer on the surface, which then altered the resistive and capacitive features of the porous electrode. Phosphate adsorption to the hematite electrode surface was found to markedly perturb measured impedance, to the extent that 10^{-9} M phosphate could be measured over a 5 mM

$NaClO_4$ blank at pH 7. More specifically, upon application of a sinusoidal applied voltage, added phosphate changed phase angle θ of impedance Z, where:

$$\mathbf{Z} = |\mathbf{Z}|\mathbf{e}^{-i\boldsymbol{\theta}} \quad (2)$$

where |Z| is the magnitude of time-dependent impedance **Z** and is a measure of the ratio of current and voltage amplitudes, i is the imaginary unit, and θ is the phase difference between applied voltage and measured current (also known as phase(Z)).

In this case, components of Z were found to be dependent on the sinusoidal frequency and the bias voltage. At -0.24 V vs. SCE and frequencies of 200 kHz to 10 mHz, our data showed a method of accurately measuring phosphate to nanomolar concentrations. The Bode phase plot of phase(Z) vs. frequency (Figure 2.5) indicated that this system was capacitive (*i.e.*, has a negative phase angle) to varied degrees at all tested frequencies and phosphate concentrations. There was a concentration-dependent local minimum that shifted from 0.18 Hz at 3 nM to 0.14 Hz at 100 μM. A plot of phase (Z) vs. |Z| (not shown) had a concentration-dependent minimum at approximately |Z| = 5000 Ohm, which corresponded to approximately 0.2 Hz for phosphate concentrations less than 10^{-6} M. Notably, 0.2 Hz was not the frequency at the phase (Z) vs. frequency local minimum, but this was found to be the frequency at which there was a great correlation (R^2 = 0.985) between the phase angle and the log of the phosphate concentration over the full 10^{-9} M to 10^{-4} M range (Figure 2.6). The sensitivity to phosphate concentration change from this plot was seen to be one half-decade in log molar units. The electrode material remained oxidized and nearly insoluble over the duration of impedance measurements at pH 7.

Another common method of analyzing impedance data is by portraying it as a Nyquist plot, graphing the negative of the imaginary component ($-Z_{imag}$) vs. the real (Z_{real}) component of **Z**, where:

$$|\mathbf{Z}| = \sqrt{\mathbf{Z_{real}^2} + \mathbf{Z_{imag}^2}} \tag{3}$$

$$\mathbf{Z_{real}} = |\mathbf{Z}|\,\mathbf{cos}(\boldsymbol{\theta}) \tag{4}$$

$$\mathbf{Z_{imag}} = |\mathbf{Z}|\,\mathbf{sin}(\boldsymbol{\theta}) \tag{5}$$

This porous iron oxide electrode might too heterogeneous in structure to realistically attempt the common practice of mapping impedance data to equivalent circuits using these data alone. However, Nyquist plots can provide qualitative information about the system itself. The data showed a maximum negative imaginary component that increased with phosphate at concentrations between 10^{-9} M and 10^{-6} M then precipitously dropped for higher concentrations (Figure 2.7). This was not likely solely due to an ionic strength difference, since the most concentrated phosphate solution in this range had only a 3.2% increase in ionic strength over a background 5 mM $NaClO_4$ solution. The plot at higher frequencies (Figure 2.8) notably changed for increasing phosphate concentrations to resemble a Warburg-like region found in porous electrochemical double layer capacitors [65]. At 10^{-4} M phosphate, there was a "knee frequency" [66] at about 2 Hz, such that at higher frequencies more of the active surface in the pores may not be accessible to analyte migration. At lower frequencies the system was more capacitive, as evidenced by the sharp negative shift in the phase of Z at frequencies less than 2 Hz. At lesser phosphate concentrations, there was no prominent knee frequency and no sharp frequency-dependent shift to greater capacitance.

Impedance spectroscopy was also applied as an alternative to cyclic voltammetry to determine phosphate concentrations at pH 4. A survey of stepped voltages showed that, at a bias voltage of -0.04 V vs. SCE, the Bode plot of phosphate solutions in the 10^{-9} M to 10^{-4} M range (Figure 2.9) had a small window of frequencies around 0.5 Hz where the spacing between log concentration units was linear. At 0.5 Hz, a plot of these phase (Z) values with phosphate concentration yielded a lin-log relationship with $R^2 = 0.973$ for the full concentration range (Figure 2.10) with perhaps a stronger correlation at concentrations $\leq 10^{-6}$ M. The application of a simple lin-log calibration plot to these data was preferred in order establish a basis for comparison to findings at pH 7, as long as a good sensitivity still held using this type of plot for more acid solutions. A theoretical sensor might measure the components of impedance Z in a window around 0.5 Hz to quickly obtain a value that can be related to phosphate concentration with little calculation, with a sensitivity of about one half-decade log molar units. Thus, the sensitivities to phosphate of this electrode at pH 7 and pH 4 were similar. One caveat is that the electrode should not be held at the bias voltage for very long periods of time in acidic conditions. This is due to the fact that the voltage applied appeared to increase the oxide dissolution rate for the electrode material, and at this acidic pH this will eventually lead to erosion of the coating to an extent that calibration would be affected. “Knee frequency” Nyquist plot behavior, such as those found in higher phosphate concentrations at neutral pH, was discernable for low phosphate concentration solutions at pH 4, lending more evidence to the theory that surface charge plays a part in these perturbation effects.

The time required for each concentration measurement using these procedures was slightly over 6 minutes, which included 185 s for 25 CV cycles, 180 s wait time to reach a steady state current at bias voltage, and 1 s (at 2 Hz) or 8 s (0.5 Hz) for impedance measurements over a

frequency range of +/- 10% of the desired value at 20 points per decade. The time per measurement may be shortened with faster CV scan rates and the use of drift correction to curtail long wait times to reach steady state current.

2.3.5. Limitations from Hysteresis

Hysteresis in a sensor may arise from strong, irreversible binding between an analyte and the electrode surface. To determine the extent that this hematite electrode was able to measure phosphate concentrations without memory, we calibrated the electrode using impedance data to a maximum 100 nM phosphate solution, applied 25 CV cycles, then took an impedance measurement in a pH 7 phosphate-free 5 mM $NaClO_4$ blank. The blank solution was measured by the electrode as containing 9.65 nM phosphate. This indicates a small amount of phosphate was being retained by the electrode after these 25 CV cleaning cycles. More work is needed to optimize the procedure between measurements to increase reversibility of data collection while maintaining the integrity of the material over time. A thorough analysis of the reversibility limitations at very low phosphate concentrations will be necessary in order improve the performance of this sensing electrode.

2.3.6. Comparison of Phosphate Signal with Arsenate

The hematite iron oxide electrode was also used to test arsenate concentration in 5 mM $NaClO_4$ at pH 7 for the purpose of comparison to phosphate sensing results. As the arsenate anion is chemically very similar to orthophosphate, phosphate sensors tend to not have good functionality in distinguishing between the two ions [13]. Arsenate is also a potential-determining ion on iron (hydr)oxide minerals [67, 68]. A Bode phase diagram for concentrations

10^{-9} M – 10^{-4} M arsenate on the hematite electrode (Figure 2.11) showed nearly identical patterns to phosphate over the full frequency range, with phosphate tending to produce only slightly less negative phase angle values than arsenate at frequencies above the knee frequency and slightly greater phase angles at lower frequencies. At f = 0.2 Hz, a lin-log fit of the phase of impedance vs. arsenate concentration gave R^2 = 0.988, and the difference between phase values for phosphate and arsenate at this frequency were in all cases less than the spacing between log concentration units for phosphate. Thus, arsenate was expected to be an interfering anion during phosphate detection with this electrode using EIS and a single frequency measurement.

2.3.7. Electrochemical Analysis of Phosphate in Simulated Lake Water

Hematite electrodes in simulated lake water at pH 7 produced Bode phase plots that indicated that the relationship between the phase of impedance and phosphate concentration was similar the case of the electrode in $NaClO_4$ background electrolyte (Figure 2.12). In the lake water solution, sulfate and bicarbonate were anions that could theoretically compete with phosphate adsorption on the oxide surface. The concentration of sulfate (0.12 mM) and the sum of carbonate and bicarbonate (0.90 mM) were both greater than the highest phosphate concentration used (0.10 mM). However, as was the case in the inert electrolyte, a lin-log relationship between phase of impedance and phosphate concentration was present at 0.2 Hz over the full 1 nM to 0.1 mM range, with R^2 = 0.966 in this case (Figure 2.13). Still, there are notable differences in the spectra of the perchlorate electrolyte and simulated lake water. In perchlorate, low phosphate concentrations did not produce a decrease in phase angle at frequencies below 0.2 Hz, where greater phosphate concentrations did produce this effect. In the simulated lake water, the phosphate-free and all phosphate solutions did have this decline to

more capacitive phase angles at lower frequencies. It is possible that some adsorption of sulfate and/or bicarbonate may be producing the "knee frequency" type behavior at 0.2 Hz that only occurred with added phosphate in the perchlorate system. However, the addition of phosphate did still augment this feature in the lake water spectra. The result is that the phase difference among the range of phosphate concentrations was not as great, as the slope of the lin-log correlation curve was only 52% of the slope from studies in 5 mM $NaClO_4$ at pH 7. This indicated that the sensitivity of phosphate detection in solutions with competing ions may be less than in inert electrolyte. Still, half-decade log unit resolution was clearly possible over the several orders of magnitude of phosphate concentration tested.

2.4. Conclusion

We have produced nanoporous iron (hydr)oxide thin-film electrodes that showed promise as phosphate sensors. Both amorphous ferrihydrite and hematite ceramic coatings on nickel substrate were investigated. Phosphate sensing was possible through measurement of the perturbation of the electrodes' response in cyclic voltammograms and impedance spectra upon addition of phosphate.

While phosphate species are not electroactive in this potential range, the result of this analyte adsorption to the electrode surface was an increased anodic peak current in a cyclic voltammogram. This effect was most evident using the highly porous ferrihydrite electrode in a pH 4 sodium perchlorate solution, for which the current during the anodic scan was fit to a range of 10^{-9} to 10^{-3} M phosphate. However, the signal using this method of detection did notably degrade with the number of voltage cycles. When this method was attempted using the less degradable hematite electrode, or when the solution was at basic pH, the electrode failed to

produce equivalent sensitivity. Perturbation of anodic peak intensity may be the result of altered surface charge upon specific adsorption of phosphate to iron hydr(oxide), as both lowered pH and greater phosphate levels lead to a more pronounced anodic peak.

When phosphate was added to the nanoporous hematite electrode, electrochemical impedance was perturbed as a function of the phosphate concentration. Impedance spectroscopy, with cyclic voltammetric "cleaning" steps between solutions, was used to make standard curves from Bode phase plot data for the range of 10^{-9} to 10^{-4} M phosphate at pH 4 and pH 7 in 5 mM $NaClO_4$ and at pH 7 in simulated lake water that contained competing ions. In all cases, strong lin-log relationships between the phase of impedance and phosphate concentration showed evidence of sensitivity to concentration changes of one half-decade log molar units. Resolution in pH 7 simulated lake water was less than in an inert electrolyte solution. Nyquist plots showed Warburg-like behavior at high frequencies, similar to what has been observed for other nanoporous electrodes, and these features in our system are phosphate concentration dependent at pH 7.

Our electrochemical phosphate sensors showed sensitivity 2-4 orders of magnitude greater than phosphate biosensors [13], rivaling the limit of detection of high-end lab analyses using magnesium induced co-precipitation (MAGIC) [69-72] and liquid waveguide capillary cell (LWCC) [72-75] methods, but without consuming as much material or requiring as much labor. The sensitivity was possible in a solution containing common lake water ions, but more research is needed to improve limitations that result from hysteresis and to confirm selectivity of the sensor to orthophosphates over other phosphorus molecules in real lake water.

References

[1] Schindler, D. W. Eutrophication and recovery in experimental lakes: implications for lake management. *Science* **1974**, *184*, 897-899.

[2] Schindler, D. W. Factors regulating phytoplankton production and standing crop in the world's freshwaters. *Limnology and Oceanography* **1978**, *23*, 478-486.

[3] Wef, A. A. Standard methods for the examination of water and wastewater. *American Public Health Association, Washington, DC* **1995**, *16*.

[4] Spivakov, B. Y.; Maryutina, T. A.; Muntau, H. Phosphorus speciation in water and sediments. *Pure Applied Chemistry* **1999**, *71*, 2161 2176.

[5] Carey, C. M.; Riggan Jr, W. B. Cyclic polyamine ionophore for use in a dibasic phosphate-selective electrode. *Analytical Chemistry* **1994**, *66*, 3587-3591.

[6] Meruva, R. K.; Meyerhoff, M. E. Mixed potential response mechanism of cobalt electrodes toward inorganic phosphate. *Analytical Chemistry* **1996**, *68*, 2022-2026.

[7] Petrucelli, G. C.; Kawachi, E. Y.; Kubota, L. T.; Bertran, C. A. Hydroxyapatite-based electrode: a new sensor for phosphate. *Analytical Communications* **1996**, *33*, 227-229.

[8] Engblom, S. O. Determination of inorganic phosphate in a soil extract using a cobalt electrode. *Plant and Soil* **1999**, *206*, 173-179.

[9] De Marco, R.; Phan, C. Determination of phosphate in hydroponic nutrient solutions using flow injection potentiometry and a cobalt-wire phosphate ion-selective electrode. *Talanta* **2003**, *60*, 1215-1221.

[10] Shimizu, Y.; Ishikawa, A.; Iseki, K.; Takase, S. Perovskite-type oxide-based electrode: A new sensor for hydrogen-phosphate ion. *Journal of the Electrochemical Society* **2000**, *147*, 3931.

[11] Zou, Z.; Han, J.; Jang, A.; Bishop, P. L.; Ahn, C. H. A disposable on-chip phosphate sensor with planar cobalt microelectrodes on polymer substrate. *Biosensors and Bioelectronics* **2007**, *22*, 1902-1907.

[12] Cleary, J.; Slater, C.; McGraw, C.; Diamond, D. An autonomous microfluidic sensor for phosphate: on-site analysis of treated wastewater. *Sensors Journal, IEEE* **2008**, *8*, 508-515.

[13] Engblom, S. O. The phosphate sensor. *Biosensors and Bioelectronics* **1998**, *13*, 981-994.

[14] Hudson, J. J.; Taylor, W. D.; Schindler, D. W. Phosphate concentrations in lakes. *Nature* **2000**, *406*, 54-56.

[15] Kubo, I.; Satoh, D. Preparation of phosphate-binding-protein-modified electrode and its application to reagentless phosphate sensor. *Sensors and Materials* **2004**, *16*.

[16] Anderson, M. A.; Malotky, D. T. The adsorption of protolyzable anions on hydrous oxides at the isoelectric pH. *Journal of Colloid and Interface Science* **1979**, *72*, 413–427.

[17] Tejedor-Tejedor, M. I.; Anderson, M. A. Protonation of phosphate on the surface of goethite as studied by CIR-FTIR and electrophoretic mobility. *Langmuir* **1990**, *6*, 602–611.

[18] Hackley, V. A. Investigation of Structure Development in Disordered Materials: Aggregation, Gelation, and Sintering of Colloidal Iron and Titanium Dioxide, University of Wisconsin-Madison: Madison, WI, 1991.

[19] Hackley, V. A.; Anderson, M. A. Synthesis and characterization of unsupported ferric oxide ceramic membranes. *Journal of Membrane Science* **1992**, *70*, 41-51.

[20] Jacquinot, P.; Hodgson, A. W. E.; Hauser, P. C. Amperometric detection of NO and NO_2 in the ppb range with solid-polymer electrolyte membrane supported noble metal electrodes. *Analytica Chimica Acta* **2001**, *443*, 53-61.

[21] Miura, N.; Lu, G.; Yamazoe, N. High-temperature potentiometric/amperometric NO_x sensors combining stabilized zirconia with mixed-metal oxide electrode. *Sensors and Actuators B: Chemical* **1998**, *52*, 169-178.

[22] Hodgson, A. W. E.; Jacquinot, P.; Hauser, P. C. Electrochemical sensor for the detection of SO_2 in the low-ppb Range. *Analytical Chemistry* **1999**, *71*, 2831-2837.

[23] Knake, R.; Hauser, P. C. Sensitive electrochemical detection of ozone. *Analytica Chimica Acta* **2002**, *459*, 199-207.

[24] Yao, T. A chemically-modified enzyme membrane electrode as an amperometric glucose sensor. *Analytica Chimica Acta* **1983**, *148*, 27-33.

[25] Malitesta, C.; Palmisano, F.; Torsi, L.; Zambonin, P. G. Glucose fast-response amperometric sensor based on glucose oxidase immobilized in an electropolymerized poly (o-phenylenediamine) film. *Analytical Chemistry* **1990**, *62*, 2735-2740.

[26] Palmisano, F.; Rizzi, R.; Centonze, D.; Zambonin, P. G. Simultaneous monitoring of glucose and lactate by an interference and cross-talk free dual electrode amperometric biosensor based on electropolymerized thin films. *Biosensors and Bioelectronics* **2000**, *15*, 531-539.

[27] Yao, S.; Xu, J.; Wang, Y.; Chen, X.; Xu, Y.; Hu, S. A highly sensitive hydrogen peroxide amperometric sensor based on MnO_2 nanoparticles and dihexadecyl hydrogen phosphate composite film. *Analytica Chimica Acta* **2006**, *557*, 78-84.

[28] Janek, R. P.; Fawcett, W. R.; Ulman, A. Impedance spectroscopy of self-assembled monolayers on Au (111): evidence for complex double-layer structure in aqueous $NaClO_4$ at the potential of zero charge. *Journal of Physical Chemistry B* **1997**, *101*, 8550–8558.

[29] Berggren, C.; Bjarnason, B.; Johansson, G. Capacitive biosensors. *Electroanalysis* **2001**, *13*, 173–180.

[30] Dumont, F.; Van Tan, D.; Watillon, A. Study of ferric oxide hydrosols from electrophoresis, coagulation, and peptization measurements. *Journal of Colloid and Interface Science* **1976**, *55*, 678–687.

[31] Kazarinov, V.; Andreev, V.; Mayorov, A. Investigation of the adsorption properties of the TiO_2 electrode by the radioactive tracer method. *Journal of Electroanalytical Chemistry and Interfacial Electrochemistry* **1981**, *130*, 277–285.

[32] Tejedor-Tejedor, M. I.; Anderson, M. A. "In situ" ATR-Fourier transform infrared studies of the goethite (FeOOH)-aqueous solution interface. *Langmuir* **1986**, *2*, 203–210.

[33] Maneepong, S.; Wada, S. Stability of Cl^-, NO_3^-, ClO_4^-, and SO_4-surface complexes at synthetic goethite/aqueous electrolyte interfaces. *Soil Science and Plant Nutrition (Japan)* **1991**, *37*, 141-150.

[34] Rietra, R.; Hiemstra, T.; Van Riemsdijk, W. H. Electrolyte anion affinity and its effect on oxyanion adsorption on goethite. *Journal of Colloid and Interface Science* **2000**, *229*, 199-206.

[35] Bourikas, K.; Hiemstra, T.; Van Riemsdijk, W. H. Ion pair formation and primary charging behavior of titanium oxide (anatase and rutile). *Langmuir* **2001**, *17*, 749–756.

[36] Hawke, D.; Carpenter, P. D.; Hunter, K. A. Competitive adsorption of phosphate on goethite in marine electrolytes. *Environmental Science & Technology* **1989**, *23*, 187–191.

[37] Yates, D.; Healy, T. Mechanism of anion adsorption at the ferric and chromic oxide/water interfaces. *Journal of Colloid and Interface Science* **1975**, *52*, 222–228.

[38] Foissy, A.; M'pandou, A.; Lamarche, J. M.; Jaffrezic-Renault, N. Surface and diffuse-layer charge at the TiO_2-electrolyte interface. *Colloids and Surfaces* **1982**, *5*, 363–368.

[39] Giacomelli, C. E.; Avena, M. J.; De Pauli, C. P. Aspartic acid adsorption onto TiO_2 particles surface. Experimental data and model calculations. *Langmuir* **1995**, *11*, 3483–3490.

[40] Rodríguez, R.; Blesa, M. A.; Regazzoni, A. E. Surface complexation at the TiO_2 (anatase)/aqueous solution interface: chemisorption of catechol. *Journal of Colloid and Interface Science* **1996**, *177*, 122–131.

[41] Kosmulski, M.; Gustafsson, J.; Rosenholm, J. B. Correlation between the zeta potential and rheological properties of anatase dispersions. *Journal of Colloid and Interface Science* **1999**, *209*, 200–206.

[42] Antelo, J.; Avena, M.; Fiol, S.; López, R.; Arce, F. Effects of pH and ionic strength on the adsorption of phosphate and arsenate at the goethite-water interface. *Journal of Colloid and Interface Science* **2005**, *285*, 476–486.

[43] Martens, D. C.; Zelazny, L. W.; Ritchey, K. D.; Baligar, V. C.; He, L. M. Hydroxyl-sulfate exchange stoichiometry on γ-Al_2O_3 and kaolinite. *Soil Science Society of America Journal* **1996**, *60*, 442–452.

[44] He, L. M.; Martens, D. C.; Ritchey, K. D.; Baligar, V. C.; Zelazny, L. W. Ionic strength effects on sulfate and phosphate adsorption on γ-alumina and kaolinite: triple-layer model. *Soil Science Society of America Journal* **1997**, *61*, 784–793.

[45] Persson, P.; Lövgren, L. Potentiometric and spectroscopic studies of sulfate complexation at the goethite-water interface. *Geochimica et Cosmochimica Acta* **1996**, *60*, 2789–2799.

[46] Hug, S. J. In situ Fourier transform infrared measurements of sulfate adsorption on hematite in aqueous solutions. *Journal of Colloid and Interface Science* **1997**, *188*, 415–422.

[47] Eggleston, C. M.; Hug, S.; Stumm, W.; Sulzberger, B.; Dos Santos Afonso, M. Surface complexation of sulfate by hematite surfaces: FTIR and STM observations. *Geochimica et Cosmochimica Acta* **1998**, *62*, 585–593.

[48] Peak, D.; Ford, R. G.; Sparks, D. L. An in Situ ATR-FTIR Investigation of sulfate bonding mechanisms on goethite. *Journal of Colloid and Interface Science* **1999**, *218*, 289–299.

[49] Geelhoed, J. S.; Hiemstra, T.; Van Riemsdijk, W. H. Phosphate and sulfate adsorption on goethite: Single anion and competitive adsorption. *Geochimica et Cosmochimica Acta* **1997**, *61*, 2389–2396.

[50] Rahnemaie, R.; Hiemstra, T.; van Riemsdijk, W. H. Carbonate adsorption on goethite in competition with phosphate. *Journal of Colloid and Interface Science* **2007**, *315*, 415–425.

[51] Machesky, M. L.; Anderson, M. A. Calorimetric acid-base titrations of aqueous goethite and rutile suspensions. *Langmuir* **1986**, *2*, 582–587.

[52] Atkinson, R. J.; Posner, A. M.; Quirk, J. P. Crystal nucleation in Fe(III) solutions and hydroxide gels. *Journal of Inorganic and Nuclear Chemistry* **1968**, *30*, 2371-2374.

[53] Garrels, R. M.; Mackenzie, F. T. In *Equilibrium Concepts in Natural Water Systems*; Advances in Chemistry; American Chemical Society, 1967; Vol. 67, pp. 222-242.

[54] Smith, E. J.; Davison, W.; Hamilton-Taylor, J. Methods for preparing synthetic freshwaters. *Water Research* **2002**, *36*, 1286–1296.

[55] Schwertmann, U.; Friedl, J.; Stanjek, H. From Fe(III) ions to ferrihydrite and then to hematite. *Journal of Colloid and Interface Science* **1999**, *209*, 215-223.

[56] Amhamdi, H.; Dumont, F.; Buess-Herman, C. Effect of urea on the stability of ferric oxide hydrosols. *Colloids and Surfaces A: Physicochemical and Engineering Aspects* **1997**, *125*, 1-3.

[57] Lang, G. G.; Horanyi, G. Some interesting aspects of the catalytic and electrocatalytic reduction of perchlorate ions. *Journal of Electroanalytical Chemistry* **2003**, *552*, 197-211.

[58] Grygar, T. Kinetics of electrochemical reductive dissolution of iron (III) hydroxy-oxides. *Collection of Czechoslovak Chemical Communications* **1995**, *60*, 1261–1273.

[59] Bard, A. J.; Faulkner, L. R. *Electrochemical Methods: Fundamentals and Applications*; 2nd ed.; John Wiley & Sons, 2001.

[60] Gilman, S. In *Electroanalytical Chemistry*; Arnold: London, 1967; Vol. 2, pp. 111-192.

[61] Randles, J. E. B. A cathode ray polarograph. part II.—the current-voltage curves. *Transactions of the Faraday Society* **1948**, *44*, 327-338.

[62] Sevcik, A. Oscillographic polarography with periodical triangular voltage. *Collection of Czechoslovak Chemical Communications* **1948**, *13*, 349-377.

[63] Hansmann, D. D.; Anderson, M. A. Using electrophoresis in modeling sulfate, selenite, and phosphate adsorption onto goethite. *Environmental Science & Technology* **1985**, *19*, 544–551.

[64] Breeuwsma, A.; Lyklema, J. Physical and chemical adsorption of ions in the electrical double layer on hematite (α-Fe_2O_3). *Journal of Colloid and Interface Science* **1973**, *43*, 437–448.

[65] de Levie, R. On porous electrodes in electrolyte solutions: I. Capacitance effects. *Electrochimica Acta* **1963**, *8*, 751-780.

[66] Conway, B. E. Electrochemical supercapacitors: scientific fundamentals and technological applications; Springer, 1999.

[67] Hsia, T. H.; Lo, S. L.; Lin, C. F.; Lee, D. Y. Characterization of arsenate adsorption on hydrous iron oxide using chemical and physical methods. *Colloids and Surfaces A: Physicochemical and Engineering Aspects* **1994**, *85*, 1-7.

[68] Manning, B. A.; Goldberg, S. Modeling competitive adsorption of arsenate with phosphate and molybdate on oxide minerals. *Soil Science Society of America Journal* **1996**, *60*, 121-131.

[69] Karl, D. M.; Tien, G. MAGIC: A sensitive and precise method for measuring dissolved phosphorus in aquatic environments. *Limnology and Oceanography* **1992**, *37*, 105-116.

[70] Rimmelin, P.; Moutin, T. Re-examination of the MAGIC method to determine low orthophosphate concentration in seawater. *Analytica Chimica Acta* **2005**, *548*, 174-182.

[71] Anagnostou, E.; Sherrell, R. M. A MAGIC method for sub-nanomolar orthophosphate determination in freshwater. *Limnology and Oceanography: Methods* **2008**, *6*, 64–74.

[72] Li, Q. P.; Hansell, D. A. Intercomparison and coupling of magnesium-induced co-precipitation and long-path liquid-waveguide capillary cell techniques for trace analysis of phosphate in seawater. *Analytica Chimica Acta* **2008**, *611*, 68–72.

[73] Zhang, J. Z.; Chi, J. Automated analysis of nanomolar concentrations of phosphate in natural waters with liquid waveguide. *Environmental Science & Technology* **2002**, *36*, 1048-1053.

[74] Gimbert, L. J.; Haygarth, P. M.; Worsfold, P. J. Determination of nanomolar concentrations of phosphate in natural waters using flow injection with a long path length liquid waveguide capillary cell and solid-state spectrophotometric detection. *Talanta* **2007**, *71*, 1624-1628.

[75] Patey, M. D.; Rijkenberg, M. J. A.; Statham, P. J.; Stinchcombe, M. C.; Achterberg, E. P.; Mowlem, M. Determination of nitrate and phosphate in seawater at nanomolar concentrations. *TrAC Trends in Analytical Chemistry* **2008**, *27*, 169-182.

Figures

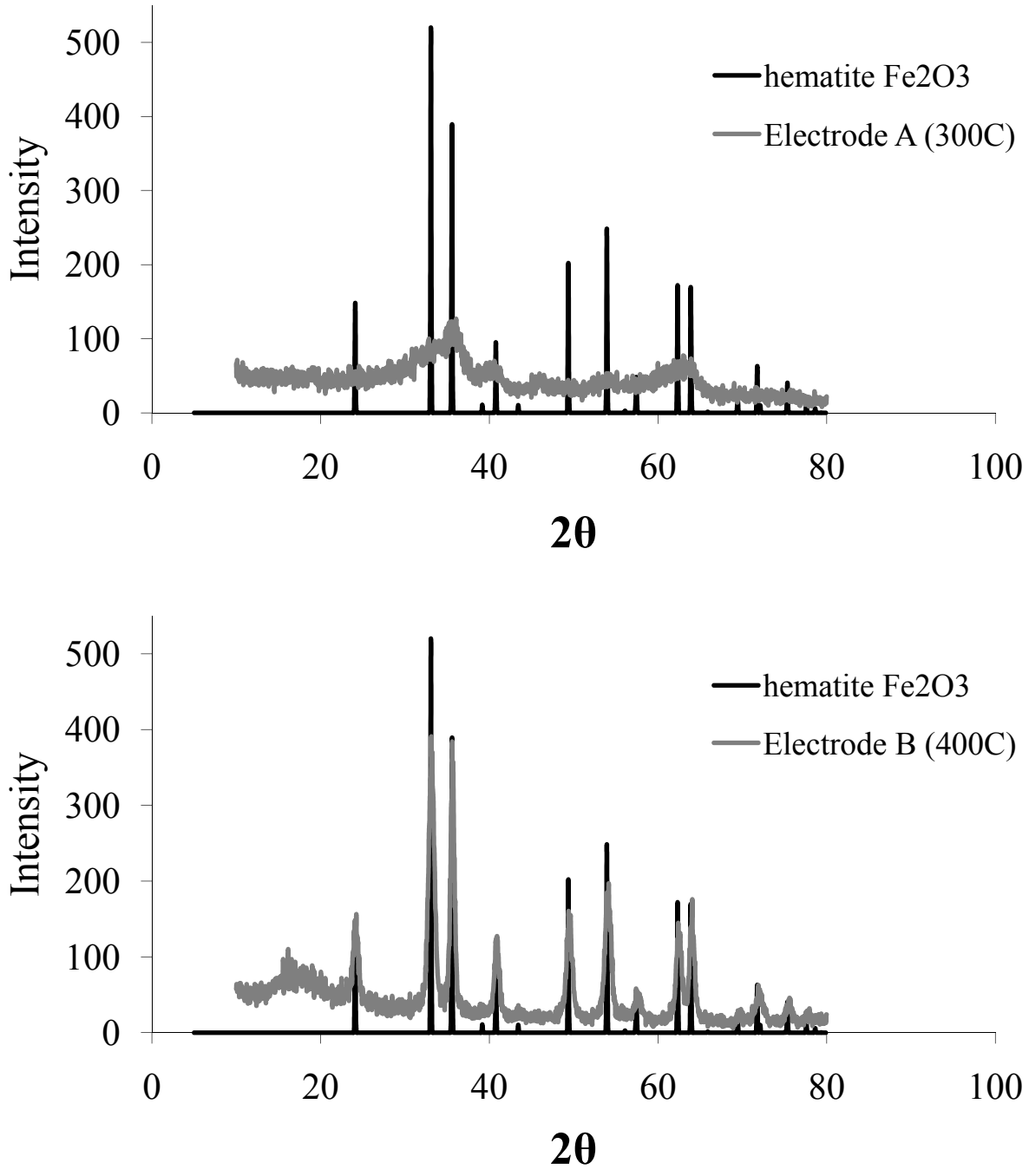

Figure 2.1 X-ray diffraction peak profiles of pure hematite (α-Fe_2O_3) compared to Electrode A (*above*) and Electrode B (*below*).

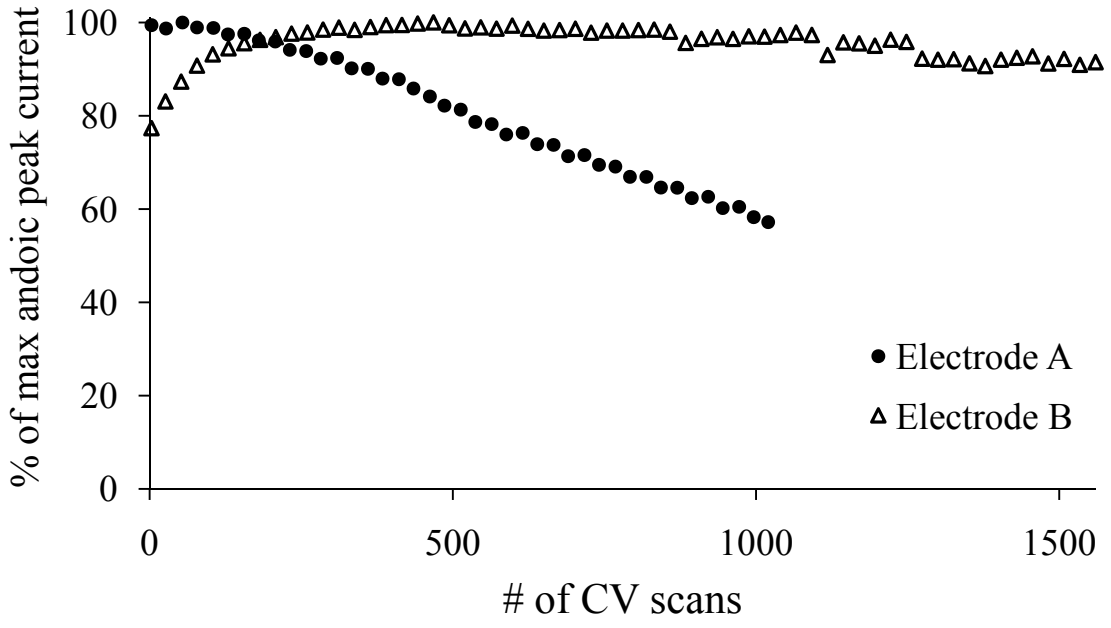

Figure 2.2 Decay in anodic peak current (I_{ap}) with repeated potential cycling, as a percent of maximum I_{ap} value, for Electrode A (amorphous ferrihydrite) and Electrode B (hematite) in 10^{-3} M phosphate, 0.01 M $NaClO_4$, pH 4. Cyclic voltammetric scans are -0.2 V – 0.8 V vs. SCE at 100 $mV \cdot s^{-1}$.

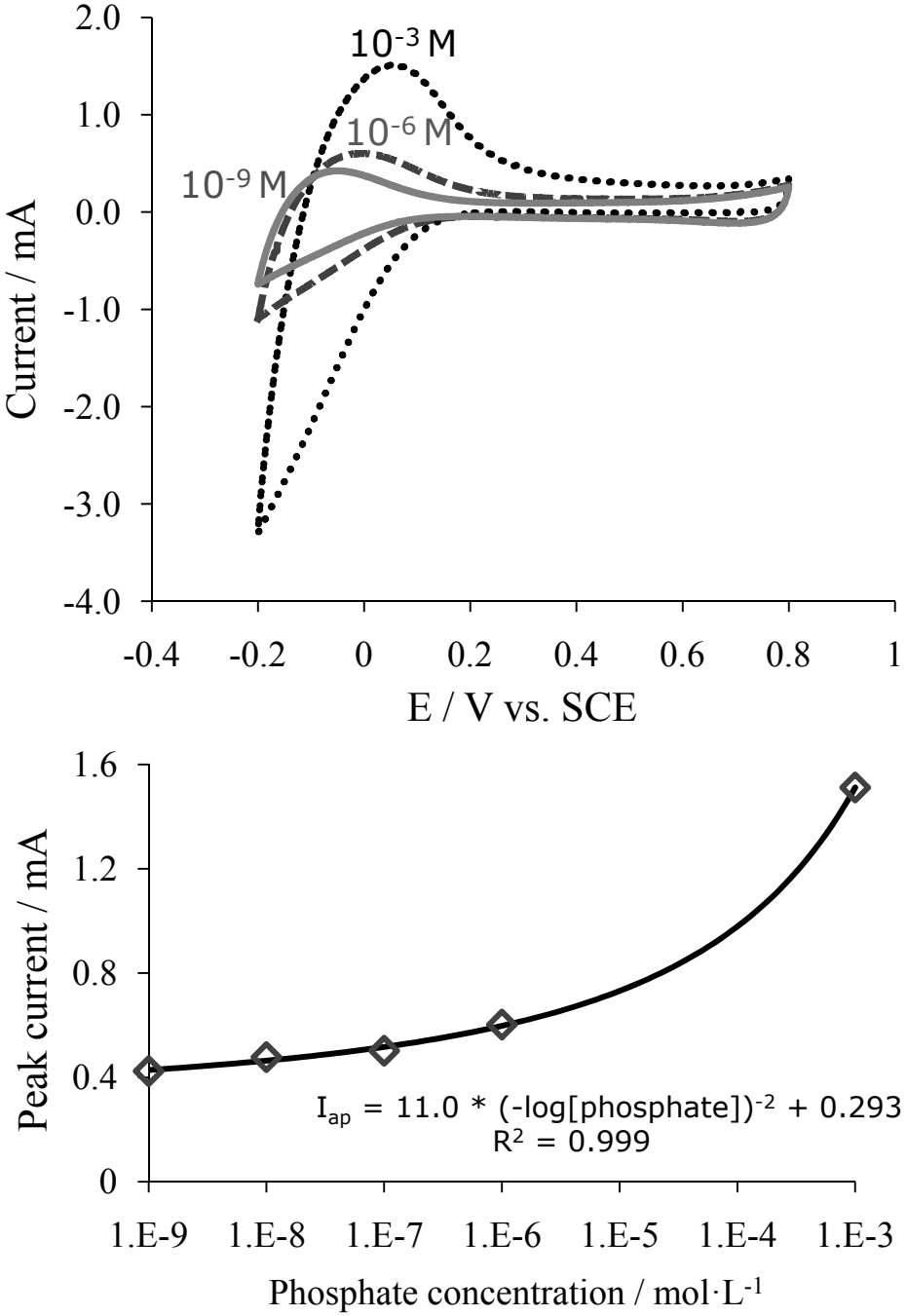

Figure 2.3 (*above*) Electrode A cyclic voltammograms of increasing phosphate concentration in 0.01 M $NaClO_4$, pH 4; (*below*) Fit of anodic peak current values for 10^{-9} – 10^{-3} M phosphate using Equation (1).

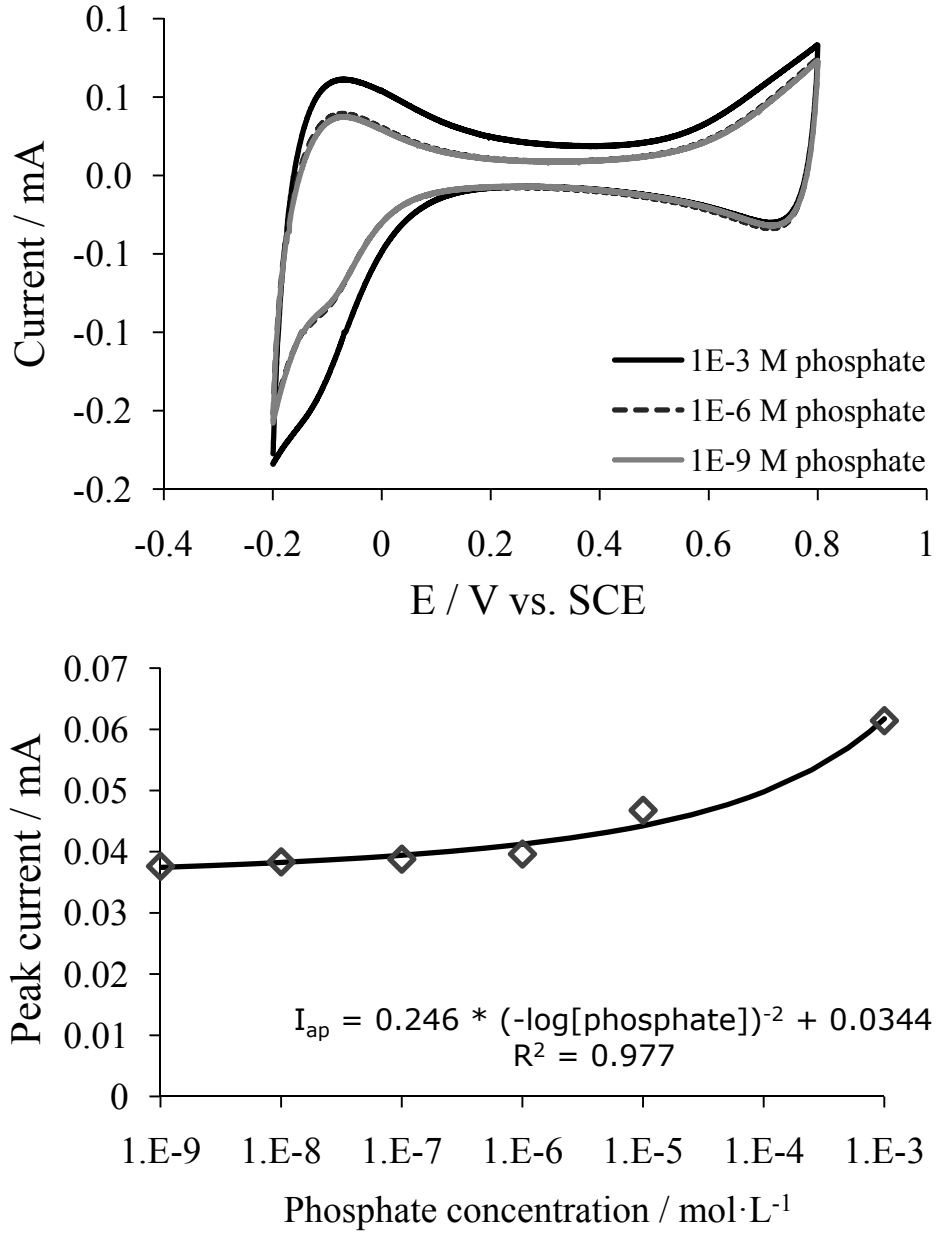

Figure 2.4 (*above*) Electrode B cyclic voltammograms of increasing phosphate concentration in 0.01 M $NaClO_4$, pH 4; (*below*) Fit of anodic peak current values for 10^{-9} – 10^{-3} M phosphate using Equation (1).

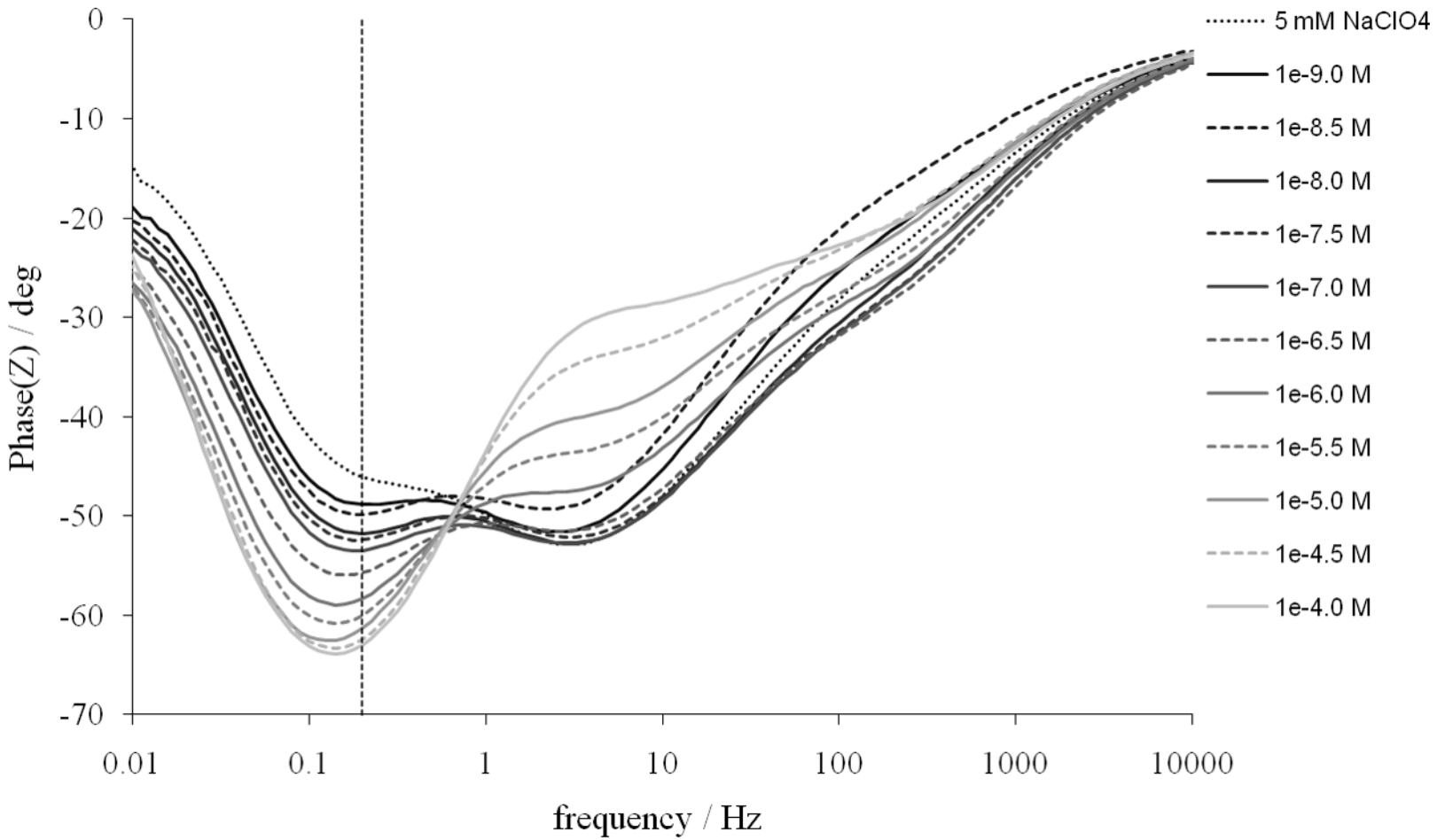

Figure 2.5 Bode phase plot for 10^{-9} – 10^{-4} M phosphate in 5 mM $NaClO_4$, pH 7, at bias voltage -0.24 V vs. SCE over the frequency range of 10 mHz – 10 kHz, with dotted line indicating 0.2 Hz.

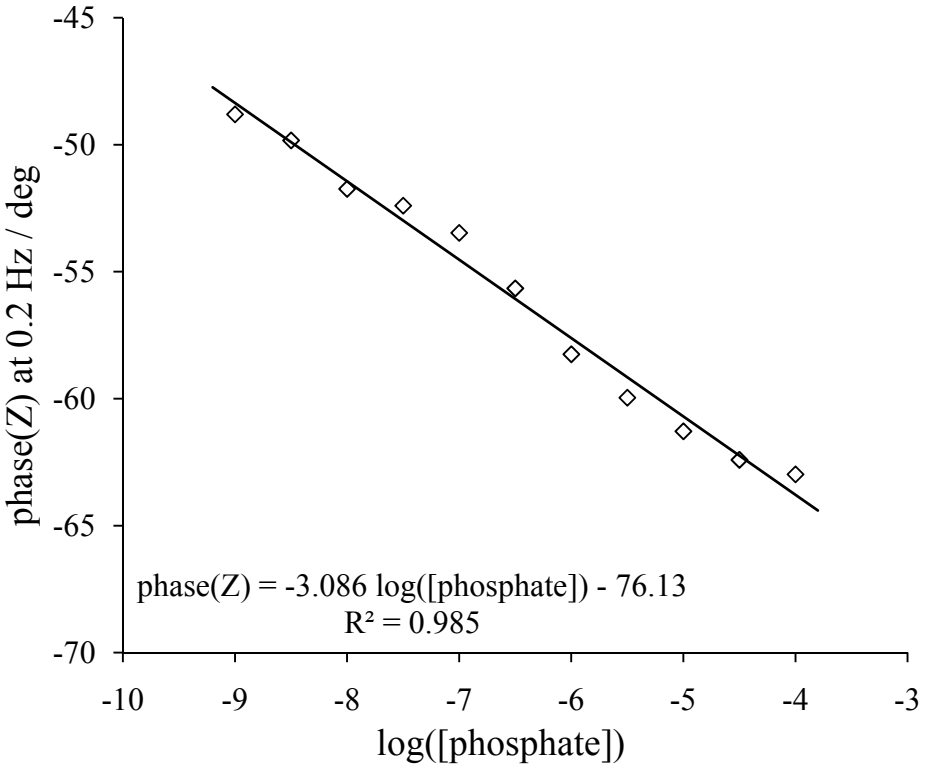

Figure 2.6 Fit of the phase of impedance vs. the log of molar phosphate concentration at $f = 0.2$ Hz for $10^{-9} – 10^{-4}$ M phosphate in 5 mM $NaClO_4$, pH 7.

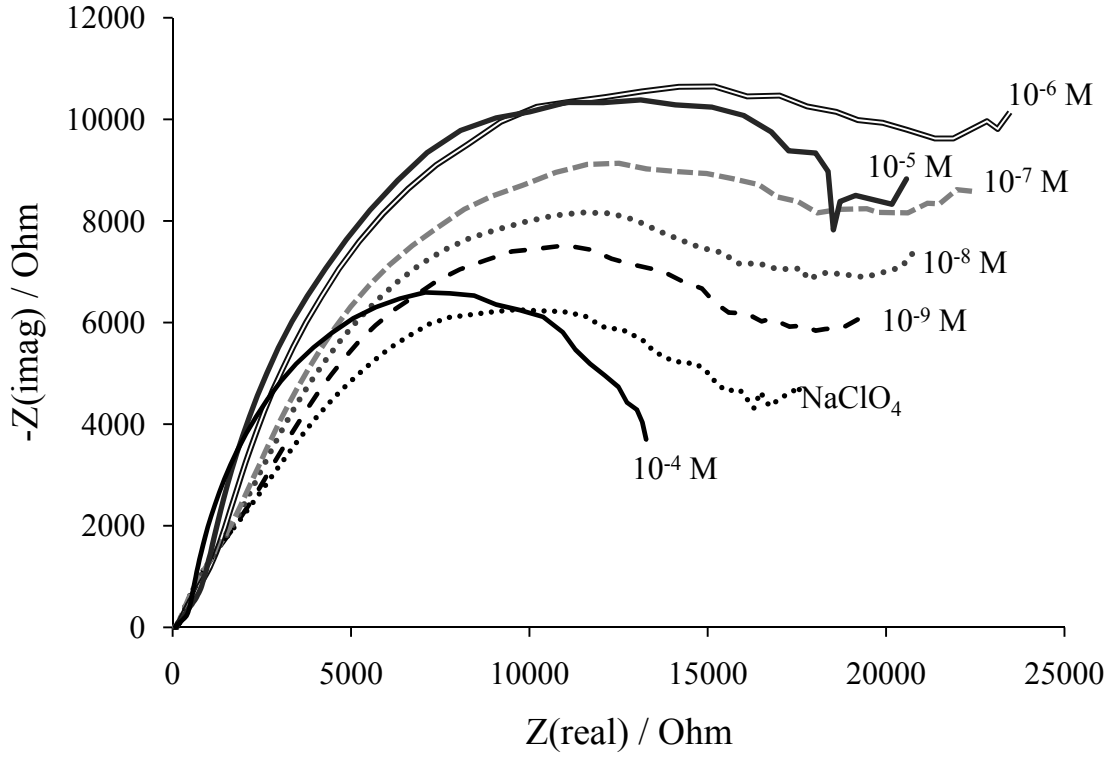

Figure 2.7 Nyquist plot for 10^{-9} – 10^{-4} M phosphate in 5 mM $NaClO_4$, pH 7, over the frequency range 200 kHz to 5 mHz.

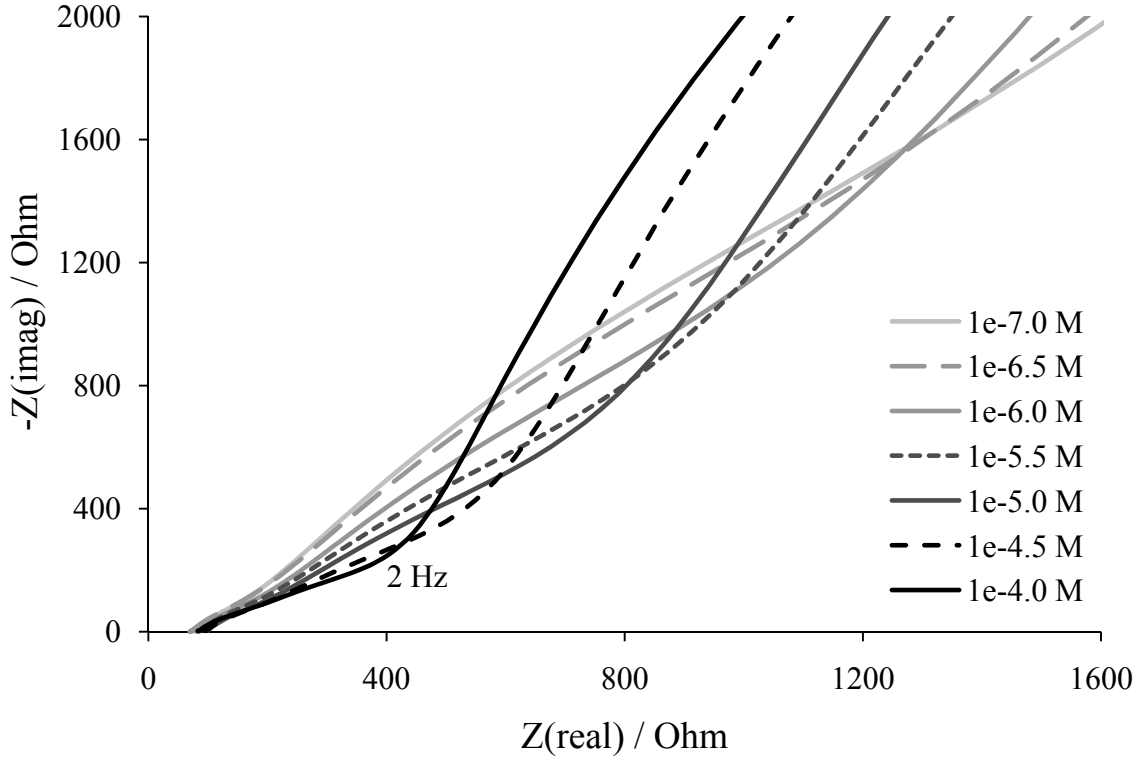

Figure 2.8 Nyquist plot for 10^{-7} – 10^{-4} M phosphate in 5 mM $NaClO_4$, pH 7, at high frequencies, with f = 2 Hz indicated for 10^{-4} M phosphate curve.

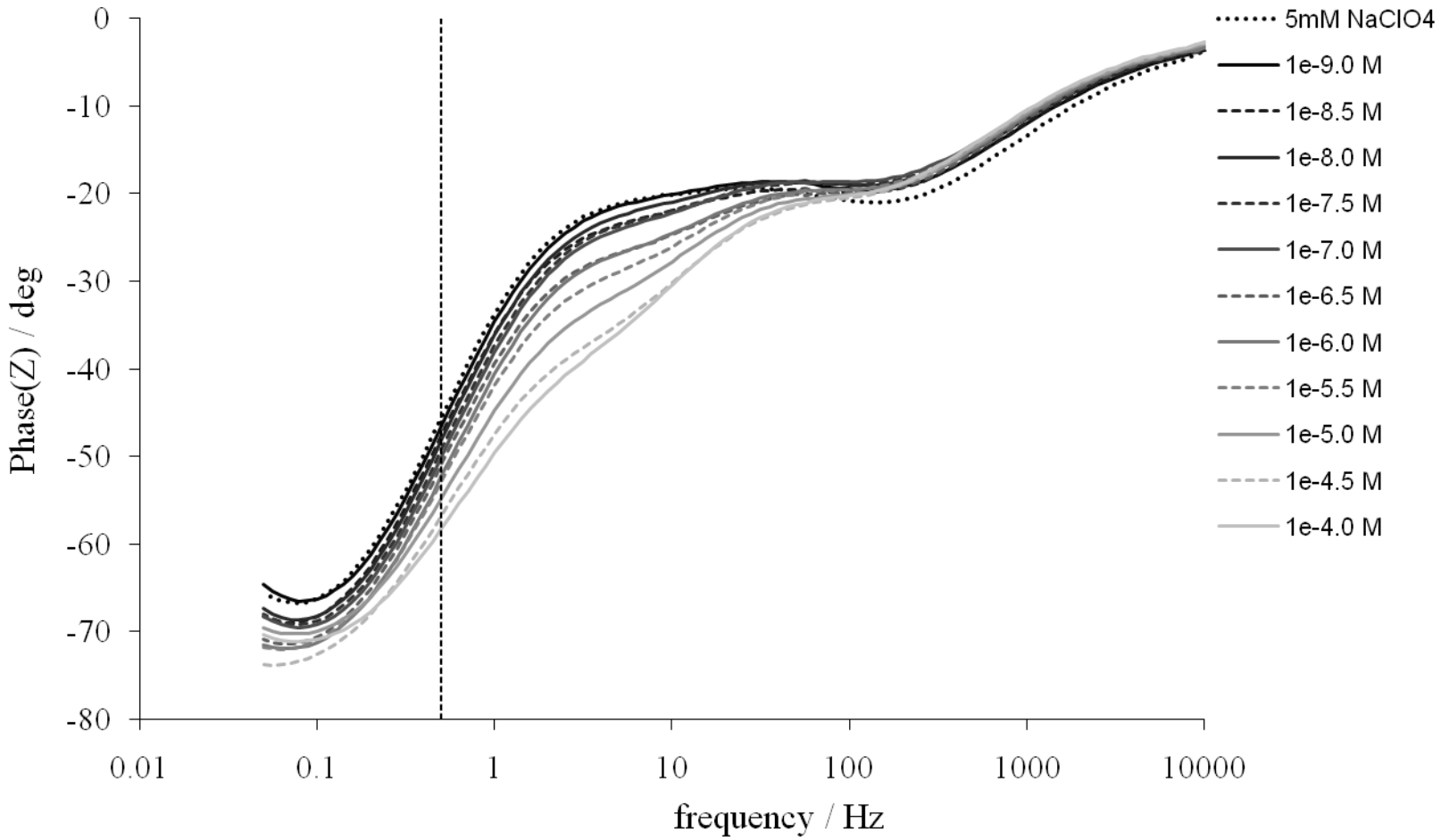

Figure 2.9 Bode phase plot for 10^{-9} – 10^{-4} M phosphate in 5 mM $NaClO_4$, pH 4, at bias voltage -0.04 V vs. SCE over the frequency range of 50 mHz – 10 kHz, with dotted line indicating 0.5 Hz.

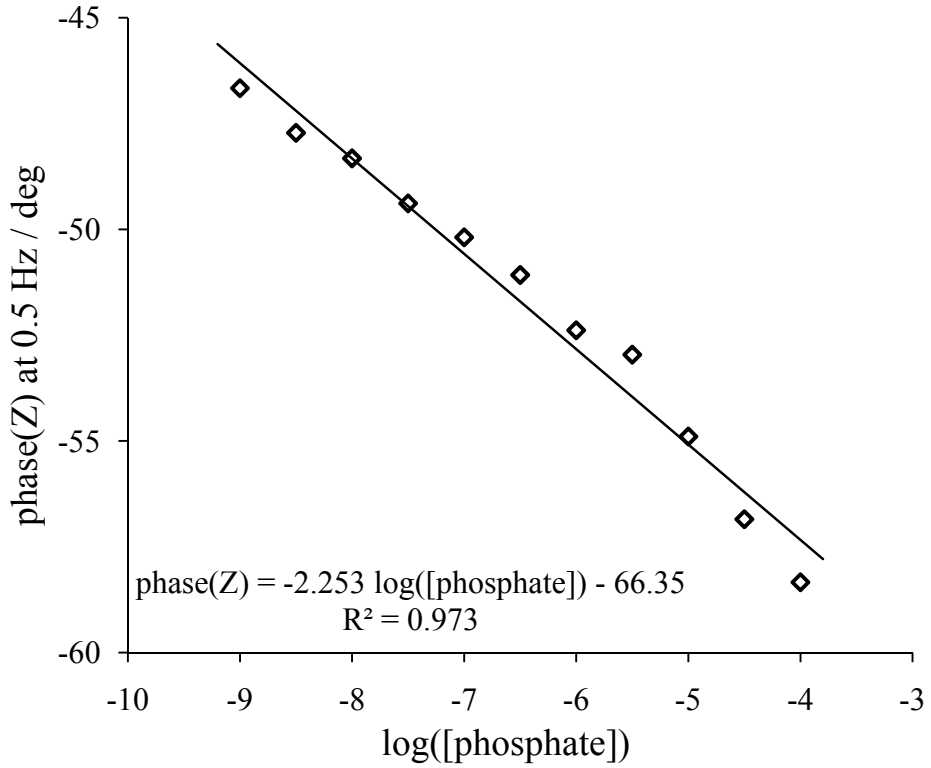

Figure 2.10 Fit of the phase of impedance vs. the log of molar phosphate concentration at f = 0.5 Hz, at bias voltage -0.04 V vs. SCE, for 10^{-9} – 10^{-4} M phosphate in 5 mM $NaClO_4$, pH 4.

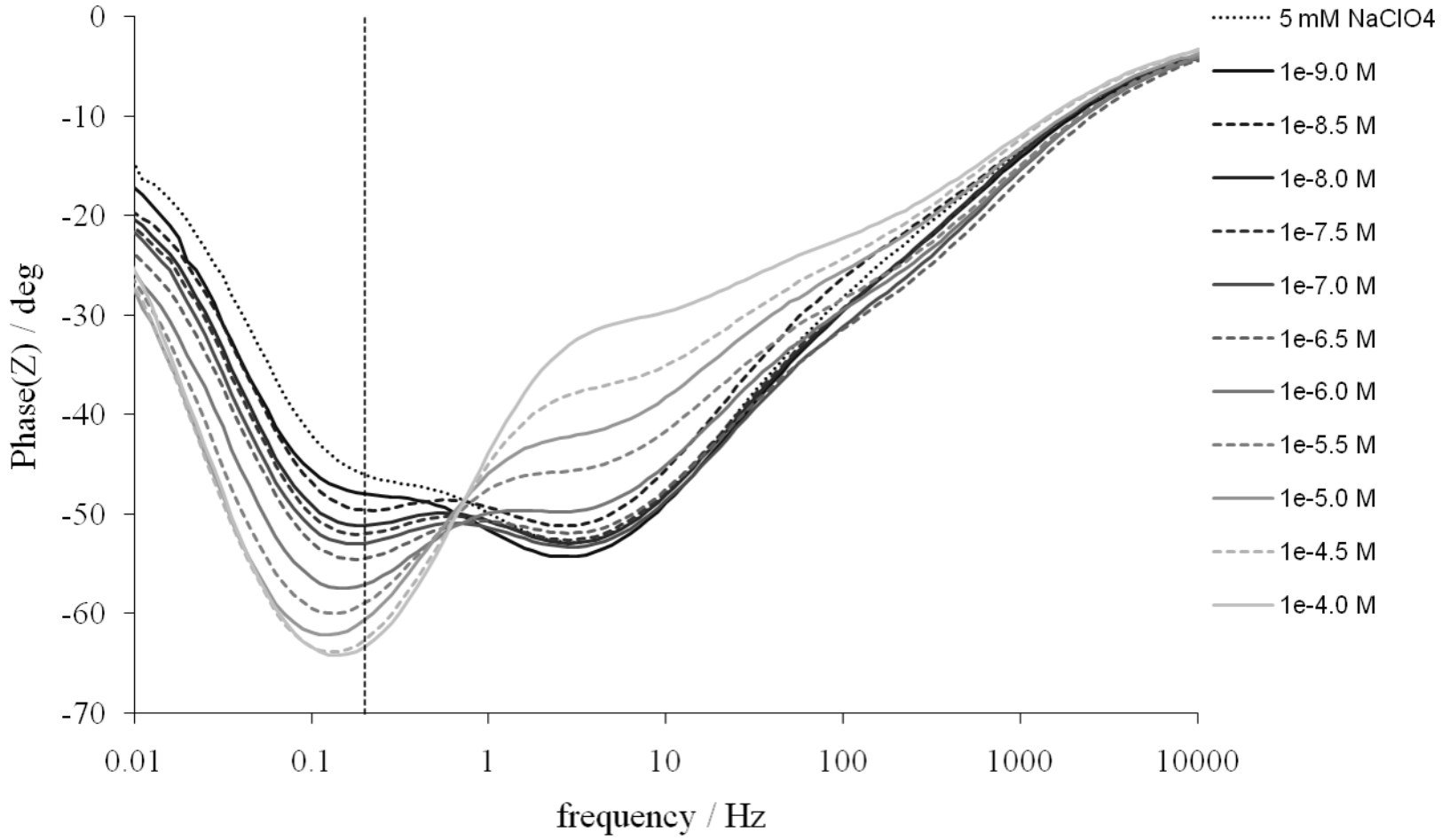

Figure 2.11 Bode phase plot for 10^{-9} – 10^{-4} M arsenate in 5 mM $NaClO_4$, pH 7, at bias voltage -0.24 V vs. SCE over the frequency range of 10 mHz – 10 kHz, with dotted line indicating 0.2 Hz.

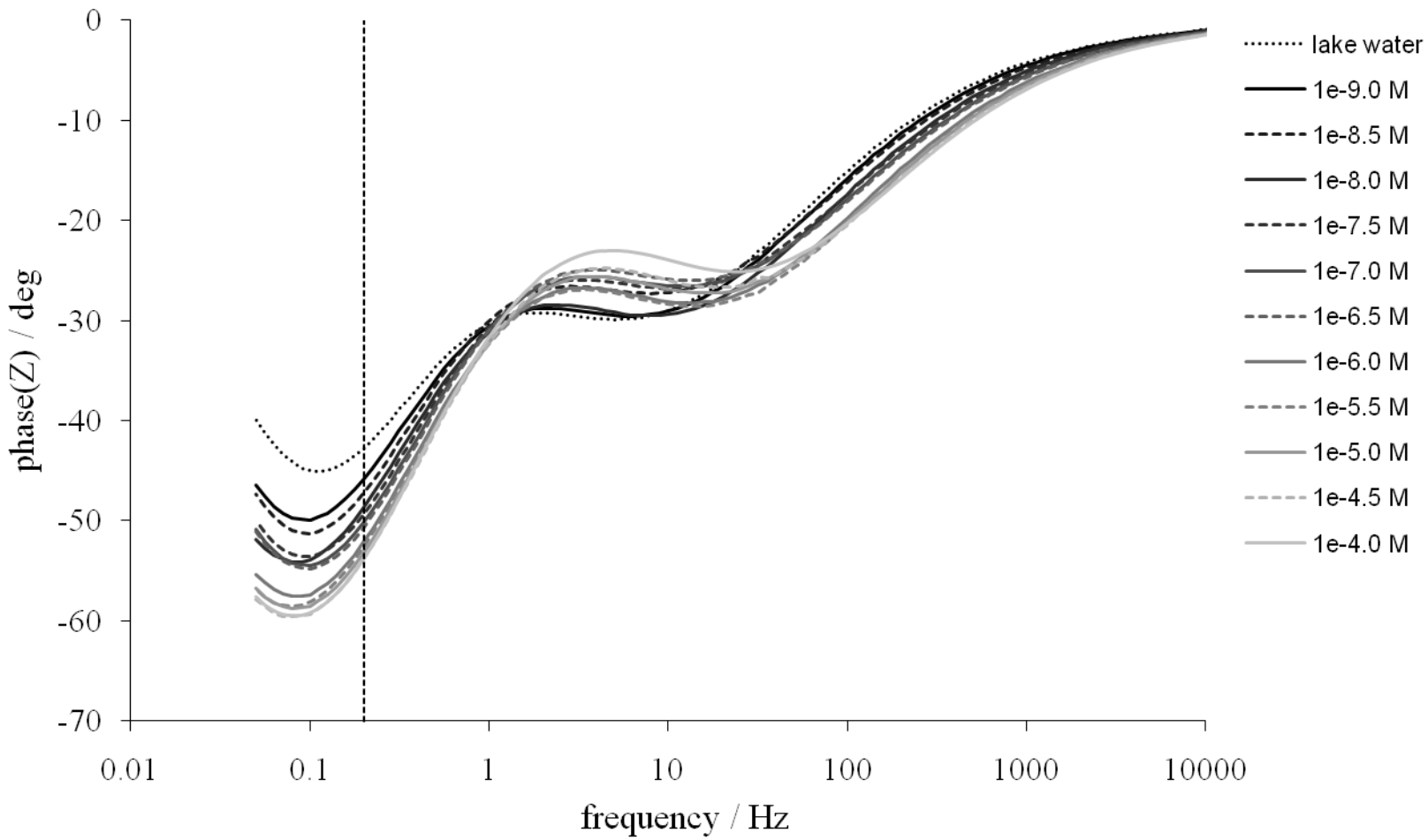

Figure 2.12 Bode phase plot for 10^{-9} – 10^{-4} M phosphate in simulated lake water, pH 7, at bias voltage -0.24 V vs. SCE over the frequency range of 50 mHz – 10 kHz, with dotted line indicating 0.2 Hz.

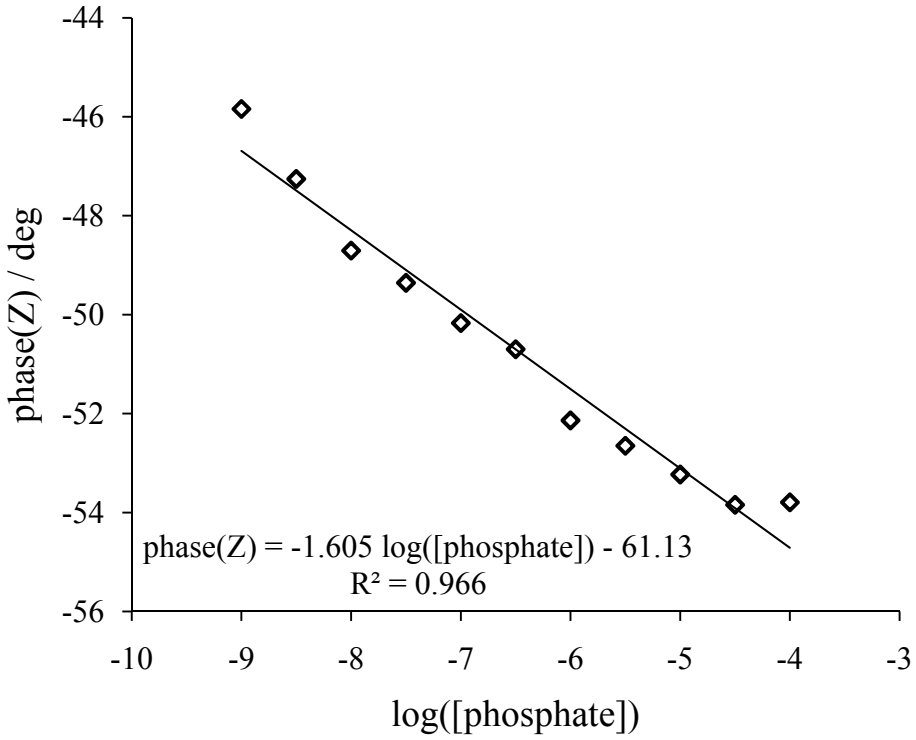

Figure 2.13 Fit of the phase of impedance vs. the log of molar phosphate concentration at f = 0.2 Hz for 10^{-9} –10^{-4} M phosphate in simulated lake water, pH 7.

CHAPTER 3

EFFECTS OF pH ON PHOSPHATE ADSORPTION TO HEMATITE AS STUDIED WITH CYCLIC VOLTAMMETRY AND ELECTROCHEMICAL IMPEDANCE SPECTROSCOPY*

* A version of this chapter will be submitted to the *Journal of the Electrochemical Society*, with R. E. Pérez-Roa and M. A. Anderson as co-authors.

Abstract

Nanoporous hematite (α-Fe_2O_3) coated electrodes were applied for the investigation of the electrochemical effects of pH on adsorption of the phosphate ion to iron oxide in concentrations commonly found in natural waters. The hematite electrode was tested with cyclic voltammetry (CV) and electrochemical impedance spectroscopy (EIS) methods in $NaClO_4$ solution and in 10^{-8} – 10^{-4} M phosphate over the pH range 6.00 – 8.75. In cyclic voltammograms, the current features attributed to specific adsorption of H^+ or OH^- were accentuated by phosphate addition. Impedance studies indicated that hematite behaved like a blocking electrode with deviations to blocking behavior occurring at higher pH and with increased phosphate. Resultant spectra were modeled with an analog electric circuit with a resistor in series with three parallel lines consisting of resistive, capacitive, and constant phase elements (CPEs) highlighting processes over sections of the applied EIS frequency range. This analysis of the phosphate-hematite system may assist with the production of an electrochemical sensor for phosphate at environmentally relevant pH.

3.1 Introduction

Phosphorus is one of the essential nutrients for the development of life. However, in some cases it becomes a significant water pollutant, even at submicromolar levels. Excess phosphorus in aquatic systems can lead to periods of eutrophication that disrupt the balance of local ecosystems and are detrimental to water quality. Inorganic orthophosphate anions, generally $H_2PO_4^-$ and HPO_4^{2-} in the pH range of natural waters, are phosphorus species that are readily metabolized by cells. Thus, phosphates are especially relevant when monitoring environmental systems. Phosphates are ubiquitous in water systems and can lead to eutrophic conditions in lakes at concentrations greater than 0.2 μM [1].

Phosphate binds with high affinity to iron oxides such as hematite (α-Fe_2O_3) that are common in weathered soils and sediments. These oxides have been the focus of several studies of phosphate adsorption, as phosphate strongly competes for adsorption sites over environmentally relevant ions such as chloride, sulfate, nitrate, and carbonates [2-6]. When combined with experimental potentiometric studies [7-10] and/or IR spectroscopic results [11-15], surface complexation models (SCM) have been widely applied to investigate speciation and configuration of phosphates bound to these iron (hydr)oxides over a range of pH and surface coverage values. Most of these SCM studies have used the iron oxy-hydroxide goethite (α-FeOOH) [7-12] as the adsorbent. However, many researchers have additionally evaluated phosphate adsorption onto hematite [16-22], an oxide less susceptible to reductive dissolution [23, 24]. As most of these studies are based on adsorption isotherm data, their range of applicability lies above the micromolar level, as the required thermodynamic equilibrium is difficult to establish at lower concentrations due to detection limit constraints. Geelhoed et al. (1997) [25] measured submicromolar phosphate solution adsorption to goethite in batch

experiments using radiolabeled ^{32}P, but minimum solution concentrations were still 0.4 μM and 4 μM for pH 7 and 8.5 respectively. In non-eutrophic environmental samples, however, it is relevant to understand phosphate adsorption at ranges at least one order of magnitude below 1 μM at circumneutral and slightly basic pH.

As phosphate is adsorbed on iron (hydr)oxides in an inner-sphere mechanism, the charge in the electrical double layer (edl) would be expected to alter the electrochemistry at the surface. Phosphate is considered a potential-determining ion on iron (hydr)oxides [8, 26], and concentrations as low as 10 μM have been found to decrease the isoelectric point (iep) of goethite by five pH units below its natural point of zero charge (pzc) [9]. This effect should be detectable by commonly used techniques such as cyclic voltammetry (CV) or electrochemical impedance spectroscopy (EIS).

Perturbation of impedance, as measured by electrochemical impedance spectroscopy, seems correlated with concentration of specific analytes using specialized electrodes, although this work has been generally limited to electrodes modified with self-assembled monolayers (SAMs) [27]. We have found in our earlier study that nanoporous hematite coated electrodes are sensitive indicators of phosphate concentration using impedance and amperometric methods [28]. Analysis of the results of EIS experiments showed that there were changes in Bode phase diagrams that could be tied to phosphate concentration at pH 7 over the range 1 nM - 0.1 mM (10^{-9} – 10^{-4} M) in a 5 mM $NaClO_4$ electrolyte solution. Furthermore, we found that the intensity of a current peak in cyclic voltammograms had sensitivity to phosphate concentration at pH 4. However, this peak decreased in magnitude and phosphate sensitivity at pH 7. As our prior results were obtained for a pH range unlikely to be found in environmental samples, this study

attempts to analyze in detail the sensitivity of our hematite electrode with respect to phosphate adsorption over a greater range of environmentally relevant pH (6.00 – 8.75).

3.2 Experimental

Electrode materials with hematite thin-film coatings were produced via sol-gel methods on nickel substrate. A 40 $g \cdot L^{-1}$ aqueous colloidal suspension (sol) of nanoparticulate iron oxide was synthesized via a method adapted from the procedure in Atkinson et al. (1968) [29]. A basic solution of 500 mL 0.24 M $NaHCO_3$ was titrated at a rate of 3 $mL \cdot min^{-1}$ into a solution of 40.4 g $Fe(NO_3)_3 \cdot 9H_2O$ in 500 mL 18 $M\Omega \cdot cm$ ultrapure H_2O stirred with a Teflon stir bar, and the resultant mixture was left to stir for two additional hours at room temperature. The suspension was then microwaved in a Teflon bottle until boiling then quickly cooled in an ice bath. Microwaving of sol precursor solutions is known to force hydrolysis and produce homogenous precipitation into a stable nanoparticulate suspension [30, 31]. This suspension was next placed in a dialysis bag and dialyzed twice in water that has been titrated to pH 3.5 with HNO_3. The dialyzed sol was concentrated to a final volume of 200 mL by injection through a pervaporation cell using a Masterflex peristaltic pump. The sol was then passed through a 0.45 μm filter membrane and stored in a glass bottle stored away from light.

Electrode materials were prepared by dip-coating 5 cm by 1 cm by 0.5 mm strips of conductive 99.0% nickel foil into the sol followed by thermal treatment. Prior to coating, the Ni foil substrate was finely sanded, rinsed with 0.1 M NaOH and ultrapure water, placed in 2% HNO_3 solution for 10 minutes and again rinsed with ultrapure water. The Ni substrate was then kept in an oven 250˚C for two hours for oxidizing the surface to make it more hydrophilic. This provided for a thinner, more consistent coating. As the temperature of the oven cooled to 100˚C,

the Ni strip was removed and dipped lengthwise into the sol, then it was withdrawn from the sol at 5.0 $mm \cdot s^{-1}$. The coating was allowed to air dry at room temperature, then dipped, withdrawn, and allowed to dry again for a total 10 coats. The xerogel coating was fired at 400˚C for ten hours to sinter porous metal oxide ceramic coating onto the substrate. A surrogate xerogel was produced by allowing the sol to dry in a weighing boat but otherwise fired under the same conditions, and this was used to characterize the pore size distribution and specific surface area of these materials as determined from the N_2 adsorption isotherms at 77 K using a Micromeritics ASAP 2010 analyzer. Specific surface area of the iron oxide ceramic on Ni substrate was also analyzed for specific surface area using BET calculations from the N_2 adsorption isotherms. Electrode surfaces were examined with scanning electron microscopy (SEM) on a LEO 1530 FESEM. The iron oxide ceramic crystal structure had been previously characterized on a STOE Bragg–Brentano X-Ray Diffractometer.

Aqueous solutions of orthophosphates were prepared with NaH_2PO_4 by serial dilution in a series of pre-cleaned volumetric flasks. 99.99% trace-metal basis $NaClO_4$ was added to a final concentration of 5 mM in solutions in the 10^{-8} M to 10^{-4} M phosphate range in order to maintain constant ionic strength. Perchlorate was chosen as the background anion due to its comparatively little ability to adsorb to iron oxides as compared to other common electrolyte anions such as nitrate and chloride [3, 5, 11]. The ionic strength of 0.005 is typical of what is found in hard lake water. Between electrochemical measurements at each phosphate concentration, solutions were titrated with microliter quantities of 0.1 M solutions of ACS analytical grade NaOH and $HClO_4$. Due to the slight contribution of the phosphate ion at 10^{-4} M, ionic strength increases by 2.2% at pH 6.00 and 5.0% at pH 8.75. However, these effects were less than 1% for phosphate concentrations of 10^{-5} M and less.

Cyclic voltammetry (CV) and electrochemical impedance spectroscopy (EIS) measurements were performed in a three-electrode system controlled by a Princeton Applied Research VMP2-Z potentiostat. Parameter input and data output analysis were performed using EC-Lab V.10.18 (Bio-Logic USA) software. The area of the working electrode exposed to analyte 3 cm^2. Voltage of working electrode was measured against a saturated calomel (SCE) reference electrode, with Pt serving as the counter electrode. A pH electrode was also added to the apparatus. The electrodes were inserted into a beaker with a 250 mL volume of 5 mM $NaClO_4$ titrated with 0.1 M $HClO_4$ to pH 6.50 in a 22˚C environment. Then, the voltage was swept 200 times over a range -0.3 V – 0.8 V vs. SCE using a scan rate of 150 $mV \cdot s^{-1}$ to clean the electrode surface of adsorbed impurities. The initial cleaning step produced cyclic voltammograms that traced over themselves, such that the trace of voltammograms was no longer dependent on cycle number. The potential was then swept over the voltage window five more times, and data from the fifth cyclic voltammogram was recorded for analysis. For experiments testing the effects of bias voltage, a stepped potential electrochemical impedance spectroscopy (SPEIS) procedure was used. The potential was held at -0.20 V vs. SCE for three minutes, and then EIS was performed by applying sinusoidal waves of ± 20 mV in magnitude recorded over a frequency range 10 kHz to 10 mHz, with 20 points per decade collected for analysis. This procedure was repeated at -0.24 V and -0.28 V. After CV and EIS steps, the pH was adjusted with NaOH upward at 0.50 unit increments and the measurements repeated. This continued to a final pH of 8.50. Then, the electrodes were placed in a solution containing 10^{-4} M phosphate and 5 mM in $NaClO_4$ and titrated to pH 6.00. CV cycling followed by EIS measurements at bias voltages -0.28 V, -0.24 V, and -0.20 V vs. SCE was then repeated.

A bias voltage of -0.24 V vs. SCE was chosen for the main set of EIS and CV experiments in a range of phosphate concentrations in a 5 mM $NaClO_4$, with a range of pH values between 6.00 and 8.75. First, we conducted CV and EIS in the 5 mM $NaClO_4$ blank solution with an applied sinusoidal voltage and output recorded over the frequency range 10 kHz to 50 mHz. The starting pH for these experiments was 6.00, with adjustment upward at 0.25 unit increments between measurements. This continued to a final pH of 8.75, after which the electrodes were removed, rinsed, and placed in a 10^{-8} M phosphate solution, with the sequence repeated. This was continued using 10-fold (*i.e.*, 1-log unit) phosphate concentration increments until measurements had been made for all pH (6.00 – 8.75) and phosphate concentrations (10^{-8} M – 10^{-4} M).

Data were analyzed using Microsoft Excel, the electrochemical software EC-Lab, and the statistical software R [32]. EIS data was separated in their impedance modulus and phase angle for their qualitative assessment. The data were rendered in Bode phase diagrams that plot the phase angle (θ) of impedance (Z) against the applied frequency of the potential at this AC perturbation. The phase angle can be determined by the real (Z_{real}) and imaginary (Z_{imag}) components of the complex impedance, following Equation 1:

$$\theta = \tan^{-1}\frac{Z_{imag}}{Z_{real}} \quad (1)$$

Further analyses of EIS spectra were first performed following guidelines provided by Orazem et al. (2006) [33]. The impedance data were separated into their real and imaginary components and plotted against the corresponding frequencies, in log-log coordinates. For each

spectrum, a solution resistance was determined as the asymptotic limit of the real impedance at high frequencies. Finally, the impedance data, this time expressed as modulus |Z| and phase angle θ, were fitted to a model found empirically using EC-Lab.

3.3 Results and Discussion

3.3.1 Electrode Characterization

X-ray diffraction studies confirmed that hematite (α-Fe_2O_3) was the mineral phase of the ceramic produced from this iron oxide sol sintered at 400˚C. This was in agreement with studies showing that iron (hydr)oxide sol produced via the Fe(III)-nitrate method undergoes dehydration/dehydroxylation and structural transformation from amorphous ferrihydrite to hematite upon thermal treatments above 300˚C [34]. The crushed hematite ceramic in 5 mM $NaClO_4$ was found to have an isoelectric pH of 8.1, which is within the range of 7.6 - 9.1 compiled for lab-prepared hematite samples by Kosmulski (2009) [35]. For comparative purposes, the unfired sol has an isoelectric pH of 7.8 with mean colloid particle size 3.5 nm (Malvern Zetasizer 3000).

From BET analysis, we determined that our electrodes provided an average surface area of 0.0980 m^2 for 3.0 cm by 1.0 cm sections that would be exposed to the analyte. Since the thin coatings did not provide a great quantity of mass available for the BET analysis, the surface area was evaluated by a different method using calculations from: 1) the specific surface area and porosity of a greater mass of the substrate-free ceramic, and 2) the amount of Fe that is dissolved from the electrode with HNO_3 as analyzed with Inductively Coupled Plasma Optical Emission Spectrometry (ICP-OES). Using this alternative method for calculating electrode surface area, a mass of 2.88 mg Fe was determined per electrode coating, corresponding to a total mass of

coating of 4.11 mg Fe_2O_3 using a hematite density of 5.26 $g \cdot cm^{-3}$. The specific surface area of the substrate-free ceramic was found to be 37.0 $m^2 \cdot g^{-1}$, thus the calculated electrode surface area exposed to solution was 0.152 m^2. The BET-determined porosity of the substrate-free ceramic was 32.3%, giving a calculated mean film thickness of 5.8 μm. This was not far removed from the mean film thickness 13.8 μm (range 6.5 – 20.9 μm) measured by viewing cross-section images of a prepared electrode with SEM (Figure 3.1). As viewed in the micrograph, the film on the electrode substrate did not have uniform thickness, and at 1000x magnification a great amount of heterogeneity and rough structure is visible that was likely indicative of the porosity. The mean pore diameter of the unsupported iron oxide ceramic was 68.4 Å (90% range 37.5 – 88.1 Å), indicating a mesoporous coating.

Adsorption isotherms of phosphate on the iron (hydr)oxide goethite as measured by Strauss et al. [36] and Antelo et al. [9] and extrapolated to our electrode surface area show that 10^{-4} M phosphate would nearly saturate this electrode at pH 6 – 9. However, lower phosphate concentrations (*i.e.*, 10^{-5} M and below) likely would not. Work by Huang et al. [22] using hematite also show that 10^{-4} M phosphate will be close to saturation for our surface, taking into account that their study had a total hematite surface area approximately four times greater than that of the exposed surface of our electrodes.

3.3.2 Cyclic Voltammograms

A nanoporous hematite electrode in 5 mM $NaClO_4$, free of added phosphate, produced features in cyclic voltammograms over the range pH 6.00 – 8.75 as seen in Figure 3.2. With an anodic potential sweep toward positive potential, one can see that the general features obtained were an initial current increase from surface charging with no anodic peak current and, at

potentials greater than 0.0 V vs. SCE, a broad increase in current. When the voltage sweep was reversed at the switching potential of +0.8 V vs. SCE, the current dropped to negative values and produced a cathodic peak. The current again diminished as the cathodic potential sweep reaches voltages less than 0.0 V vs. SCE.

The features of these cyclic voltammograms were pH dependent. It is generally considered that perchlorate anions absorb to iron (hydr)oxides in a nonspecific way; the perchlorate anion does not enter the Stern layer nor does it notably change the features of the electrical double layer beyond charge screening [9]. Oxidation of perchlorate to chloride at circumneutral pH was expected to be negligible due to great kinetic restraints on this reaction [37], and measurable surface catalysis for this reaction was not expected as perchlorate is separated from the iron oxide by at least one solvation layer. The sodium ion was also not expected to affect electrochemical features beyond ionic strength effects, due to its strong energy of hydration preventing specific adsorption with the mineral surface. Therefore, features in the cyclic voltammograms of the sodium perchlorate-only solution have been attributed to specifically adsorbing H^+ and OH^-, the concentrations of which are titrated and calculated from the pH of the solution.

In the perchlorate system, a cathodic voltage sweep produced a negative current toward the oxidizing end of the window at -0.3 V vs. SCE. When the potential sweep direction was switched, the current rose to positive values, with a maximum at the positive potential switching point of the anodic sweep at +0.8 V vs. SCE. At a lesser pH, the current at -0.3 V vs. SCE was more negative than in the case with a greater pH, and the current charging after this low-voltage switching potential was greater over the anodic sweep at potentials less than 0.0 V vs. SCE. The isoelectric pH of the hematite material in 5 mM $NaClO_4$ has been shown to be 8.1. Therefore, at

lower pH the surface was expected to be positively charged. However, this electrostatic repulsion may be mitigated by a negative potential applied to the electrode and a greater H^+ concentration at the lower pH. This effect of more H^+ adsorbing to the electrode may have resulted in a more negative current at the end of the cathodic sweep window and a greater charging, perhaps attributed to H^+ adsorption, at the start of the anodic sweep. However, as the potential was raised during the anodic sweep, the surface became more electrostatically repulsive to H^+ such that the electrode at pH 6.00 produced current at a lesser rate and to a lesser maximum.

The cathodic peak produced after the high-voltage switching potential at +0.8 V vs. SCE was greatly affected by pH. The sweep toward negative potential produced a more negative cathodic peak current (I_{cp}) for greater pH. As current is by definition a change in charge with time, the current differences are attributable to a Faradaic electron transfer and/or ion migration at the electrode surface. As perchlorate and sodium were not expected to penetrate the electrical double layer, the increase in charging during the anodic sweep and greater magnitude I_{cp} in higher pH solutions might be the result of hydroxide anion adsorption and desorption. This was probably due to a greater concentration of OH^- in the bulk solution and/or a less positive or else negative hematite electrode surface, or alternatively a partial quasi-reversible electron transfer at the hematite surface oxidizing OH^- and generating H_2O and O_2. At greater pH, the potential at which the cathodic peak occurs further into the cathodic sweep (*i.e.*, at lesser voltage), and this might be the result of kinetic factors in the decrease of surface coverage of OH^- from a porous surface.

The addition of 10^{-8} – 10^{-4} M phosphate to the system significantly altered the cyclic voltammograms produced by the hematite electrode. Changes from the perchlorate system were phosphate concentration dependent and manifested themselves differently as a function of pH.

Cyclic voltammograms for phosphate concentrations (C_{PO4}) 10^{-8} – 10^{-4} M after subtracting the perchlorate-only voltammogram are shown for pH 6.00 (Figure 3.3) and pH 8.75 (Figure 3.4). In acidic solution, phosphate altered the CV features in the low-potential region similar to decreasing pH, where effects of increased C_{PO4} at high potentials more resembled those of increasing pH. At basic pH, phosphate does not change the low-potential region, but greater C_{PO4} still parallels the effects of increasing pH in the phosphate-free system. Over intermediate solution pH values, the general trend observed was that the magnitude of current with respect to all CV features increased with increased phosphate concentration.

Ion competition between phosphate and OH^- is proposed to be the cause of many of the differences between Figure 3.3 and Figure 3.4. At pH 6.00, 94% of phosphate in bulk solution will be monobasic $H_2PO_4^-$, the same charge as inert perchlorate. However, phosphate, like OH^-, is specifically adsorbing, and C_{PO4} at pH 6.00 will be several orders of magnitude greater than OH^- concentration. The perturbation on cyclic voltammograms was found to be significantly more than might be expected from adding only a slightly greater concentration of an inert monobasic anion. In fact, at pH 6.00, where OH^- concentration is relatively low, phosphate produced a discernable anodic peak at approximately -0.15 V vs. SCE for C_{PO4} greater than or equal to 10^{-7} M, where no anodic peak appeared in the perchlorate-only solution above pH 4.00. The magnitude of this anodic current peak, I_{ap}, increased with increasing C_{PO4}. At pH 8.75, OH^- concentration fell within the range of C_{PO4} used in this study (although phosphate will be 97.2% dibasic HPO_4^{2-}) and thus OH^- may function as a significant competing ion on the hematite surface. Effects at low potential were diminished at greater pH, as OH^- concentration increased, such that at pH 7.50 and above, there was no anodic current peak at any C_{PO4}. By pH 8.75, the

difference was negligible for all phosphate concentrations in the low-potential features of a phosphate solution as compared with a perchlorate-only solution.

It should be noted that the phosphate anion itself is electroinactive in these experiments (*i.e.*, it will not undergo reduction or oxidation over this potential window). However, specific adsorption of phosphate is expected to alter the charge properties at the electrical double layer of the hematite surface. In experimental work by Antelo et al. [9] that used a goethite surface area 2.7 times the electrodes in our work, the addition of only 10^{-5} M phosphate was shown to shift the isoelectric pH over five units downward. Similarly, 10^{-6} M arsenate (an anion with ion speciation similar to phosphate and similar adsorption behavior on oxides [38]) was found to shift the isoelectric value below pH 6.00. Thus, it does not seem unreasonable that 10^{-6} M - 10^{-4} M phosphate produces a negatively charged surface attractive to H^+ over the pH range from 6.00 – 8.75. The attraction of H^+ may be additionally augmented by the electric field produced by low voltages applied to the electrode. A hematite surface modified by a high surface coverage of phosphate at solution concentrations greater than or equal to 10^{-6} M might be attracting H^+ as the potential is lowered and also facilitating the release of protons as the potential was raised to positive values. The result of this interaction may be the cause of the charging and peak effects at low potential. As the hydroxide anion competes with phosphate at greater pH, the effects of phosphate adsorption in the low-potential region are negated. Therefore, this section of the curve becomes more similar to a system in which H^+ and OH^- are the only two potential determining species.

In the high-potential region of voltammograms, a 10^{-4} M C_{PO4} solution produced greater effects over perchlorate-only cyclic voltammograms than did 10^{-5}, 10^{-6}, 10^{-7}, or 10^{-8} M C_{PO4} at all pH values. However, trends with increasing phosphate concentration were more consistent and

greater in magnitude at higher pH (as in Figure 3.4) than at low pH (Figure 3.3). At pH 6.00, added solution C_{PO4} is equal to or orders of magnitude greater than the OH^- concentration, but phosphate is strongly adsorbed at low pH and may be less likely to undergo reversible electrosorption and desorption over cycling. At greater pH values, the predominant phosphate species is dibasic, the hematite surface has more negative charge, and a greater concentration of OH^- compete with phosphate. Under these conditions, it is possible that reversible sorption at high applied potential may be favorable when compared to strong phosphate adsorption. This be analogous as to how some phosphate can undergo some desorption at high solution pH [36, 39], as a greater local concentration of OH^- at high applied potential is raised likely facilitates phosphate desorption. At pH 8.75, low phosphate concentrations such as 10^{-7} and 10^{-8} M C_{PO4} appeared to produce less polarization in the high-potential region than in a perchlorate system. The reason for this phenomenon is less clear, but it might be related with strong phosphate adsorption. At concentrations less than 10^{-6} M, phosphate might not have great enough surface coverage to fully alter the surface electrochemistry, yet there is still enough adsorbed to act as a blocking layer against OH^- adsorption.

Changes in cyclic voltammograms at a constant C_{PO4} and titrated pH could be compared to the perchlorate-only voltammograms. Perturbations over the perchlorate voltammograms were most evident at high phosphate concentrations. At C_{PO4} 10^{-4} M with the perchlorate CV subtracted (Figure 3.5), the anodic peak was even more prominent than cathodic peak at pH 6.00, but a pattern emerged at increasing pH of a lesser or non-discernable anodic peak and a more prominent cathodic peak. This pattern is also seen for 10^{-5} M and 10^{-6} M phosphate to a lesser extent (data not shown). At C_{PO4} 10^{-7} and 10^{-8} M, noise predominated over distinguishable features such that the effects of pH were not so clear.

3.3.3 Charge Storage

Integration under a cyclic voltammogram provides a measure of charge (Q) stored following Equation 2, in units of mA·h:

$$Q = \frac{1}{\nu_s}\int_{E_1}^{E_2}(I_A - I_C)\cdot dE \quad (2)$$

where ν_s is the scan rate, I_A and I_C are anodic and cathodic current, and E_1 and E_2 are initial and final voltage. This equation is also applicable for calculating the excess charge stored in the phosphate-containing systems, by integrating the perchlorate-subtracted effective voltammograms like those shown in Figures 3.3 – 3.5. In order to distinguish the anodic from the cathodic effects, these charge calculations were partitioned at 0.20 V vs. SCE. This potential was chosen as the subtracted voltammograms (cf. Figures 3.3 – 3.5) show a rather small current around this voltage, although charge calculations did not significantly change when the cutoff value was set at any value between 0.10 and 0.30 V vs. SCE. The result of this analysis of the low-potential region is in Figure 3.6. This region has excess charge well correlated to phosphate over the full 10^{-8} M – 10^{-4} M range at pH less than 7.00. The excess charge over a perchlorate system is slightly negative at low pH and low C_{PO4}, possibly indicating competing processes with H^+ in this section (either thermodynamic or kinetic) when the voltage is swept at low potentials. At increasing pH, the anodic peak vanishes, and the difference in calculated excess charge of this section no longer shows discernable phosphate dependence. Qualitative trends with C_{PO4} over the pH range show more variability in the high potential region (data not shown). Although excess charge would not be expected to provide a reliable quantitative standard curve over a wide pH

and C_{PO4} range, the addition of electrochemical impedance spectroscopic methods in the low-potential region were expected to give more useful information when phosphate and the proton were more likely the indicators of electrochemical perturbations on the electrode.

3.3.4 Electrochemical Impedance Spectroscopy

The CV analysis suggested that care had to be taken on selecting a bias potential for EIS. As lower pH values seemed to enhance currents and charge storage in the low potential region, impedance data should reflect similar trends, yielding lower moduli when the pH is low and when the bias potential is below the 0.20 V vs. SCE threshold. In this study, the bias potential used for the core of EIS experiments was chosen as close in proximity to the negative switching potential in cyclic voltammograms. Low voltage bias potentials are in the region in cyclic voltammograms for which charge in excess of the perchlorate-only system was correlated with phosphate. Even within this low potential region, bias voltage selected did have an effect on impedance results. In 5 mM $NaClO_4$ solution, a bias voltage of -0.20 V vs. SCE produced a shift to more capacitive behavior (*i.e.*, θ values closer to -90˚) that occurred below a lesser frequency than was the case for -0.24 or -0.28 V vs. SCE (Figure 3.7). This occurred in a perchlorate-only solution and in 10^{-4} M phosphate. More positive bias voltage also led to a maximum capacitive-type behavior, as evidenced in a Bode phase plot by a local minimum in θ at a frequency less than 1 Hz, although in all cases the phase angle rose again at frequencies below this minimum. However, at -0.20 V vs. SCE, capacitance at low frequencies was particularly pH-dependent, where C_{PO4} dependence was low at pH values greater than 7.50. Bias voltages of -0.24 V and -0.28 V vs. SCE comparatively showed less pH dependence in a Bode phase diagram (data not shown), although -0.24 V vs. SCE might produce better resolution between log-unit C_{PO4}. In an

earlier study, -0.24 V vs. SCE was chosen as a bias voltage due to reliable correlation between phase and C_{PO4} at pH 7.00 at the frequency 0.2 Hz. In this work, when the same frequency and bias voltage were applied, the lin-log relationship between θ and C_{PO4} over the range 10^{-8} – 10^{-4} M had a coefficient of correlation (R^2) greater than 0.930 over the pH range 6.75 – 8.25. The resolution between log-unit concentrations was 1.0 – 1.5 degrees. However, the correlation was bad further away from neutral pH, as R^2 was only 0.109 at pH 6.00 and was 0.864 at pH 8.75.

A qualitative analysis of the EIS spectra was performed upon separating real and imaginary impedance components [33] and plotting in logarithmic plots against frequency. Figure 3.8 shows these results for the perchlorate-only solution and those obtained for $C_{PO4} = 10^{-4}$ M, at pH values of 6.00 and 8.00. Overall, there was an effect of both pH and phosphate concentration on both parts of the impedance, although these effects are more noticeable at low pH values. The spectra showed very little difference in the high frequency range, particularly for the imaginary parts of the impedance spectra. Phosphate concentrations induced a change in slope around the 10-Hz decade in the low pH range; smaller variations can be also observed at high pH, but at lower frequencies. In general, the core of the results, particularly for the experiments with no phosphate added, resembled a straight diagonal line with negative slope in the imaginary spectra, and a diagonal line followed by a horizontal one in the real part [33]. This pattern is associated with a blocking electrode, as both components of the impedance increase with decreasing frequencies. The solution resistance, taken as the asymptotic high-frequency limit of the real impedance, ranged between 80 and 110 Ω in these experiments. Departures from this ideal blocking behavior may be indicative of processes in parallel; moreover, they may indicate the presence of characteristic frequencies, potentially associated with adsorption and

desorption processes. In these results, deviations from the blocking electrode pattern were greater as pH decreased and C_{PO4} increased. At $C_{PO4} = 10^{-4}$ M and pH 6.00, an inflection point appeared at about 100 Hz; whereas a second feature seemed to develop at the low end of the scanned frequency range, as this curve slightly bent from its upward pattern. These two features are also observed at different values of pH and C_{PO4}, but at lower magnitudes and frequencies. Altogether, these observations could be interpreted by an electric circuit model of the solution resistance in series with three parallel lines, two of them representing the two features found in the imaginary impedance plot, and a third one indicating the blocking-like pattern that dominates this system. The resulting model circuit was comprised of 7 components, and the total impedance could be represented as shown in Equation 3:

$$Z_{total} = R_S + (Z_{Q1}^{-1} + \left(R_2 + Z_{Q2}\right)^{-1} + \ (R_3 + (R_4^{-1} + Z_{C4}^{-1})^{-1})^{-1})^{-1} \quad (3)$$

A schematic of the electronic circuit analog is shown in Figure 3.9. The model provided a good fit for all the impedance spectra recorded, including the electrolyte-only data, particularly at frequencies greater than 10 Hz (Figure 3.10). At lower frequencies, the model circuit still captured the features of the experimental data, although the fit tended to overestimate θ between 0.1 – 10 Hz and underestimate the θ as capacitance decreased at frequencies less than 0.1 Hz. Although values for impedance differed somewhat from electrode to electrode, this model circuit provided similar good fits for data from an earlier study of a similarly-prepared hematite electrode in pH 7.00 phosphate solutions in perchlorate electrolyte [28].

This equivalent circuit model consists in a resistor (R_S) in series with three parallel lines. R_S accounts for the solution resistance. The element shown in the upper line (Q_1) corresponds to

the blocking-like element and may be associated with double-layer capacitance. In the equivalent circuit, Q represents a constant phase element (CPE) component, with an impedance (Z_{CPE}) that is defined as:

$$Z_{CPE} = [Q' \cdot (2\pi f)^{\alpha}]^{-1} = [2\pi Q \cdot f^{\alpha}]^{-1} \quad (4)$$

where Q' is the magnitude of the CPE in terms of angular frequency, f is frequency, and α is the CPE coefficient. Q' was calculated from Q, the magnitude of the CPE that was produced by the modeling program as a best fit to the equivalent circuit. The unitless CPE coefficient α is between 0 and 1, where a value of 1 produces a pure capacitive element (C) from which the impedance of a capacitor may be calculated. However, the use of value other than 1 seemed appropriate for characterizing this circuit component, particularly for elements with characteristic frequencies in the high frequency range. The porous nature of the hematite electrode may produce a series of capacitive time constants, which taken altogether might yield a CPE instead of an ideal capacitor [40, 41]. Two fitting parameters are associated with a CPE, in this case Q_1 and α_1, the latter in close proximity to the negative of the high frequency slope of the imaginary impedance plot (cf. Figure 3.8). This element is dominant at the upper portion of the sampled frequencies (>100 Hz). Using a CPE instead of a capacitor to model the double layer seemed appropriate. The second line is a combination in series of a resistor (R_2) with a CPE (Q_2, α_2). This line represents the feature in the imaginary impedance plot appearing at about 100 Hz. Both of these lines act as blocking electrodes at the low frequency limit, suggesting that they are associated with interfacial capacitive phenomena. Interestingly, both CPE coefficients (α_1 and α_2) gave good fit to our data when set to 0.7, possibly suggesting that similar geometric

considerations are involved in these elements. The third line is a sub-circuit composed by a resistor (R_3) in series with a resistor (R_4) and a capacitor (C_4) placed in parallel. This line determines the impedance response in the low frequency limit ($Z = R_s + R_3 + R_4$ when $f \rightarrow 0$), taking into consideration the downward bending of the imaginary impedance observed at high C_{PO4} and low pH. Remarkably, the best fit equivalent circuit for this hematite electrode was very similar to the circuit analog that represented electrical response of porous hydrous ruthenium oxides in a study by Sugimoto et al. (2005) [42]. The hydrous RuO_2 equivalent circuit had a resistor in series with three parallel components consisting of resistors, capacitors, and CPEs, but a Warburg element was substituted for Q_2 in the second line. A CPE proved to be a better fit than a Warburg element for our hematite data, although both CPEs and Warburg elements may indicate effects of diffusion in the system. The other differences between the circuits of the two porous metal oxides were that the CPE Q_1 in the hematite model was designated a pure capacitor in the hydrous RuO_2 model, and C_4 was designated a CPE.

Figure 3.11 shows the value of selected circuit elements with respect to pH and phosphate concentration. Overall, pH seemed to increase most of the values associated with resistance and decrease the values of capacitance and CPE coefficients. It is important to remember that the impedance associated with capacitors and CPE are proportional to their inverse values. Therefore, high pH values increased the impedance of all the elements of the circuit. This observation agreed with what could be expected from the CV data, in which current outputs were greater with decreasing pH at negative voltages, considering that EIS measurements were performed at -0.24 V vs. SCE. In general, increasing C_{PO4} reduced the value of resistive elements and increased capacitance and Q values, although this trend did not continue in the sample with no phosphate added. Interestingly, most of the trends show that the

data at 10^{-8} M C_{PO4} behaves halfway between phosphate-less solutions and 10^{-7} M C_{PO4}, suggesting the possibility that the phosphate coverage at 10^{-8} M was low enough that the hematite surface experienced a competing scheme between protons and phosphate ions for determining the surface potential. Values for R_s fluctuated between 80 and 110 Ω and were consistent with the observations obtained in Figure 3.8. Similarly, Q_1 ranged from 55 to 61 $\mu F \cdot s^{\alpha-1}$, with little (<5%) variation with pH and a slightly more consistent upward trend with C_{PO4}. However, as these variations were too small to draw conclusions, plots of these variables are not shown here. The resistor element R_2 also shows a rather flat profile for $C_{PO4} \leq 10^{-6}$ M, with values between 800 and 900 Ω. A slightly upward trend with increasing pH was found for $C_{PO4} = 10^{-5}$ M, in which R_2 went from 826 Ω at pH = 6.00 to 996 Ω at pH = 8.75. At $C_{PO4} = 10^{-4}$ M, R_2 had a minimum value of 691 Ω at pH = 6.00 that increased until pH 8.25, reaching a maximum of 1043 Ω and then leveling out. Q_2, however, increased with phosphate concentration and decreased with pH. The effect of phosphate on Q_2 is noticeable at low pH for $C_{PO4} \geq 10^{-5}$ M. As pH values increased, Q_2 tended to approach a value of 50 $\mu F \cdot s^{\alpha-1}$ regardless of the phosphate concentration, and this is close to the values obtained for Q_1. These trends may suggest that the R_2/Q_2 line represents adsorption of the monobasic phosphate species, as its impedance increases with pH until reaching a maximum, at which the concentration of these species in bulk solution becomes negligible far above the pK_a at 7.2. The pH-dependent effects of the R_2/Q_2 line may also be a result of a decreasing hematite surface charge, particularly the reduced change in zeta potential at pH values above the isoelectric pH of 8.1. Regarding the sub-circuit $R_3/R_4/C_4$, dependence on pH and phosphate concentration was observed for R_3, particularly at the lower end of tested pH values. As in the case of Q_2, as pH increases, the values for this element tended to group. R_4 also showed an upward trend with pH, but unlike R_3, the

relationship with phosphate was not as clear except for $C_{PO4} = 10^{-4}$ M. With $C_{PO4} = 10^{-5}$ M, R_4 rose from 24 kΩ, that was close to the resistances obtained for lower C_{PO4}, to 180 kΩ, the largest value obtained (even above the 149 kΩ calculated for $C_{PO4} = 10^{-4}$ M). C_4 is not displayed as its values remained rather constant in the range $0.12 - 0.15$ mF for $C_{PO4} \leq 10^{-5}$ M, with a slight decreasing trend with pH. At 10^{-4} M, the capacitance decreased from 0.25 mF at pH = 6 to 0.12 mF at pH = 8.75. The trends were similar to those described for Q_2. This sub-circuit $R_3/R_4/C_4$ determined the low-frequency behavior; it may represent similar processes as those observed in the line R_2/Q_2, but at different spatial scales, as both lines followed similar trends. In simple terms, the electrode behaved as if it were performing some sort of charge transfer at low pH, reversing this trend towards a blocking electrode as pH increased. Interestingly, the impedance of the 'blocking' line R_2/Q_2 seemed to reach an asymptotic value, whereas the impedance of the 'reacting' line $R_3/R_4/C_4$ continuously increased with pH, therefore its relevance in the overall impedance switched from controlling it at low pH to becoming negligible at the upper limit of the pH range. The full set of output data for the fit of impedance spectra to the hematite electrode equivalent circuit can be found in Appendix A.

3.4 Conclusion

Nanoporous hematite (α-Fe_2O_3) coated electrodes show electrochemical response to phosphate anion concentration in a pH dependent manner as measured with cyclic voltammetry and electrochemical impedance spectroscopy. In cyclic voltammograms, pH-dependent current response of the electrode in perchlorate (a non-specifically adsorbing ion on iron oxides) was accentuated with addition of phosphate (a specifically adsorbing, potential-determining ion). At pH 6.00, cyclic voltammograms with an anodic current peak that increased in magnitude with

phosphate concentration, likely indicating a contributory effect of phosphate adsorption on proton mobility. However, the difference in charge stored, as determined by integrating the low-potential region, could not be resolved to submicromolar phosphate concentrations due to the level of signal noise at low phosphate in neutral or basic pH solutions. The high potential region of cyclic voltammograms produced a cathodic peak that showed pH and phosphate concentration dependence over the full range tested, attributed to competition between phosphate and H^+/OH^- adsorption in this region. However, but no resolution among low phosphate concentrations was observed from integrated values for the high-potential area of the voltammogram.

Electrochemical impedance spectra of the hematite electrode at low potential bias voltages also showed a pH dependence in both perchlorate and phosphate solutions. The phosphate analyte caused the electrode to become more capacitive at low applied frequencies. In an earlier study, we had found that at pH 7.00 this electrode produced a strong lin-log correlation between phase of impedance and phosphate concentration at frequency 0.2 Hz. Our present work has found that the same correlation exists over a larger pH range of 6.75 – 8.25 for phosphate concentrations in the 10 nM – 0.10 mM range. The features in the electrochemical impedance spectra over the phosphate concentration and pH range used in this work were modeled to an equivalent circuit consisting of seven components. The circuit had a resistive element representing the solution resistance and then three lines in series representing electrode behaviors over high, mid, and low frequencies. Our understanding of the system in terms of model circuit components, including CPE components, provided a more complete depiction of the complexity of the pH-phosphate interactions in the water/hematite system. Although impedance component values vary somewhat from electrode to electrode, trends are shared and this circuit model could be used to fit our earlier data. A practical application for the understanding of phosphate

adsorption on hematite would be the development of a novel electrochemical sensor that is sensitive to submicromolar phosphate.

References

[1] Sigee, D. C. Freshwater Microbiology: *Biodiversity and Dynamic Interactions of Microorganisms in the Aquatic Environment*; Wiley, 2005.

[2] Dumont, F.; Van Tan, D.; Watillon, A. Study of ferric oxide hydrosols from electrophoresis, coagulation, and peptization measurements. *Journal of Colloid and Interface Science* **1976**, 55, 678–687.

[3] Maneepong, S.; Wada, S. Stability of Cl^-, NO_3^-, ClO_4^-, and SO_4^- surface complexes at synthetic goethite/aqueous electrolyte interfaces. *Soil Science and Plant Nutrition (Japan)* **1991**, 37, 141–150.

[4] Amhamdi, H.; Dumont, F.; Buess-Herman, C. Effect of urea on the stability of ferric oxide hydrosols. *Colloids and Surfaces A: Physicochemical and Engineering Aspects* **1997**, 125, 1–3.

[5] Rietra, R.; Hiemstra, T.; Van Riemsdijk, W. H. Electrolyte anion affinity and its effect on oxyanion adsorption on goethite. *Journal of Colloid and Interface Science* **2000**, 229, 199–206.

[6] Rahnemaie, R.; Hiemstra, T.; van Riemsdijk, W. H. Carbonate adsorption on goethite in competition with phosphate. *Journal of Colloid and Interface Science* **2007**, 315, 415–425.

[7] Hansmann, D. D.; Anderson, M. A. Using electrophoresis in modeling sulfate, selenite, and phosphate adsorption onto goethite. *Environmental Science & Technology* **1985**, 19, 544–551.

[8] Tejedor-Tejedor, M. I.; Anderson, M. A. Protonation of phosphate on the surface of goethite as studied by CIR-FTIR and electrophoretic mobility. *Langmuir* **1990**, 6, 602–611.

[9] Antelo, J.; Avena, M.; Fiol, S.; López, R.; Arce, F. Effects of pH and ionic strength on the adsorption of phosphate and arsenate at the goethite-water interface. *Journal of Colloid and Interface Science* **2005**, 285, 476–486.

[10] Zhong, B.; Stanforth, R.; Wu, S.; Chen, J. P. Proton interaction in phosphate adsorption onto goethite. *Journal of Colloid and Interface Science* **2007**, 308, 40–48.

[11] Tejedor-Tejedor, M. I.; Anderson, M. A. "In situ" ATR-Fourier transform infrared studies of the goethite (α-FeOOH)-aqueous solution interface. *Langmuir* **1986**, 2, 203–210.

[12] Persson, P.; Nilsson, N.; Sjoberg, S. Structure and bonding of orthophosphate ions at the iron oxide-aqueous interface. *Journal of Colloid and Interface Science* **1996**, 177, 263–275.

[13] Arai, Y.; Sparks, D. L. ATR-FTIR spectroscopic investigation on phosphate adsorption mechanisms at the ferrihydrite-water interface. *Journal of Colloid and Interface Science* **2001**, 241, 317–326.

[14] Dimirkou, A.; Ioannou, A.; Doula, M. Preparation, characterization and sorption properties for phosphates of hematite, bentonite and bentonite-hematite systems. *Advances in Colloid and Interface Science* **2002**, 97, 37–60.

[15] Luengo, C.; Brigante, M.; Antelo, J.; Avena, M. Kinetics of phosphate adsorption on goethite: Comparing batch adsorption and ATR-IR measurements. *Journal of Colloid and Interface Science* **2006**, 300, 511–518.

[16] Madrid, L.; Arambarri, P. Adsorption of phosphate by two iron oxides in relation to their porosity. *European Journal of Soil Science* **1985**, 36, 523–530.

[17] Ioannou, A.; Dimirkou, A. Phosphate Adsorption on hematite, kaolinite, and kaolinite-hematite (kh) systems as described by a constant capacitance model. *Journal of Colloid and Interface Science* **1997**, 192, 119–128.

[18] Horanyi, G.; Joo, P. Some peculiarities in the specific adsorption of phosphate ions on hematite and γ-Al_2O_3 as reflected by radiotracer studies. *Journal of Colloid and Interface Science* **2002**, 247, 12–17.

[19] Huang, X. Intersection of isotherms for phosphate adsorption on hematite. *Journal of Colloid and Interface Science* **2004**, 271, 296–307.

[20] Elzinga, E. J.; Sparks, D. L. Phosphate adsorption onto hematite: An in situ ATR-FTIR investigation of the effects of pH and loading level on the mode of phosphate surface complexation. *Journal of Colloid and Interface Science* **2007**, 308, 53–70.

[21] Gimsing, A. L.; Borggaard, O. K. Phosphate and glyphosate adsorption by hematite and ferrihydrite and comparison with other variable-charge minerals. *Clays and Clay Minerals* **2007**, 55, 108–114.

[22] Huang, X.; Foster, G. D.; Honeychuck, R. V.; Schreifels, J. A. The maximum of phosphate adsorption at pH 4.0: why it appears on aluminum oxides but not on iron oxides. *Langmuir* **2009**, 25, 4450–4461.

[23] LaKind, J. S.; Stone, A. T. Reductive dissolution of goethite by phenolic reductants. *Geochimica et Cosmochimica Acta* **1989**, 53, 961–971.

[24] Grygar, T. Kinetics of electrochemical reductive dissolution of iron (III) hydroxy-oxides. *Collection of Czechoslovak Chemical Communications* **1995**, 60, 1261–1273.

[25] Geelhoed, J. S.; Hiemstra, T.; Van Riemsdijk, W. H. Phosphate and sulfate adsorption on goethite: Single anion and competitive adsorption. *Geochimica et Cosmochimica Acta* **1997**, 61, 2389–2396.

[26] Anderson, M. A.; Malotky, D. T. The adsorption of protolyzable anions on hydrous oxides at the isoelectric pH. *Journal of Colloid and Interface Science* **1979**, 72, 413–427.

[27] Berggren, C.; Bjarnason, B.; Johansson, G. Capacitive biosensors. *Electroanalysis* **2001**, 13, 173–180.

[28] Moss, R. E.; Jackowski, J. J.; de Souza Castilho, M.; Anderson, M. A. Development and evaluation of a nanoporous iron (hydr)oxide electrode for phosphate sensing. *Electroanalysis* **2011**, 23, 1718–1725.

[29] Atkinson, R. J.; Posner, A. M.; Quirk, J. P. Crystal nucleation in Fe(III) solutions and hydroxide gels. *Journal of Inorganic and Nuclear Chemistry* **1968**, 30, 2371–2374.

[30] Acarbas, O.; Ozenbas, M. Preparation of iron oxide nanoparticles by microwave synthesis and their characterization. *Journal of Nanoscience and Nanotechnology* **2008**, 8, 655–659.

[31] Hu, L.; Percheron, A.; Chaumont, D.; Brachais, C. H. Microwave-assisted one-step hydrothermal synthesis of pure iron oxide nanoparticles: magnetite, maghemite and hematite. *Journal of Sol-Gel Science and Technology* **2011**, 1–8.

[32] R Team. R: A language and environment for statistical computing. R Foundation for Statistical Computing.Vienna, Austria **2010**.

[33] Orazem, M. E.; Pébère, N.; Tribollet, B. Enhanced graphical representation of electrochemical impedance data. *Journal of the Electrochemical Society* **2006**, 153, B129–B136.

[34] Schwertmann, U.; Friedl, J.; Stanjek, H. From Fe (III) ions to ferrihydrite and then to hematite. *Journal of Colloid and Interface Science* **1999**, 209, 215–223.

[35] Kosmulski, M. Compilation of PZC and IEP of sparingly soluble metal oxides and hydroxides from literature. *Advances in Colloid and Interface Science* **2009**, 152, 14–25.

[36] Strauss, R.; Brümmer, G.; Barrow, N. Effects of crystallinity of goethite: II. Rates of sorption and desorption of phosphate. *European Journal of Soil Science* **1997**, 48, 101–114.

[37] Urbansky, E. T. Perchlorate chemistry: implications for analysis and remediation. *Bioremediation Journal* **1998**, 2, 81–95.

[38] Hiemstra, T.; Van Riemsdijk, W. H. Surface structural ion adsorption modeling of competitive binding of oxyanions by metal (hydr)oxides. *Journal of Colloid and Interface Science* **1999**, 210, 182–193.

[39] Chitrakar, R.; Tezuka, S.; Sonoda, A.; Sakane, K.; Ooi, K.; Hirotsu, T. Phosphate adsorption on synthetic goethite and akaganeite. *Journal of Colloid and Interface Science* **2006**, 298, 602–608.

[40] Nyikos, L.; Pajkossy, T. Fractal dimension and fractional power frequency-dependent impedance of blocking electrodes. *Electrochimica Acta* **1985**, 30, 1533–1540.

[41] Pajkossy, T. Impedance spectroscopy at interfaces of metals and aqueous solutions—Surface roughness, CPE and related issues. *Solid State Ionics* **2005**, 176, 1997–2003.

[42] Sugimoto, W.; Iwata, H.; Yokoshima, K.; Murakami, Y.; Takasu, Y. Proton and electron conductivity in hydrous ruthenium oxides evaluated by electrochemical impedance spectroscopy: the origin of large capacitance. *The Journal of Physical Chemistry B* **2005**, 109, 7330–7338.

Figures

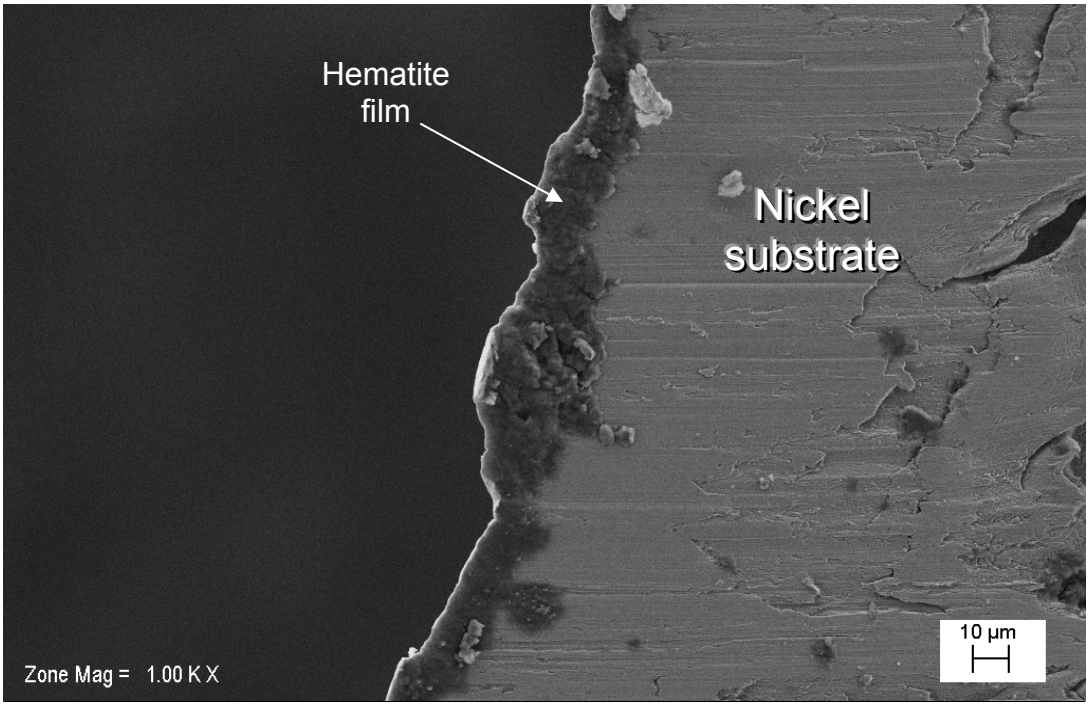

Figure 3.1 Scanning electron micrograph of hematite electrode edge at 1000x magnification.

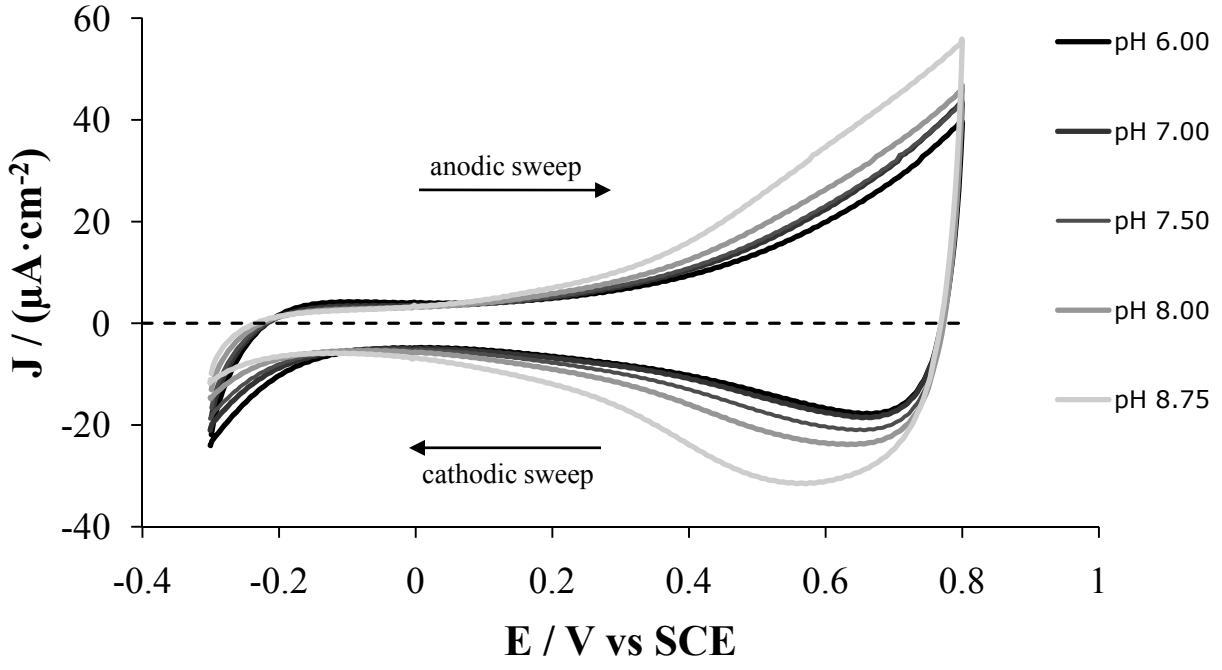

Figure 3.2 Cyclic voltammograms of blank solutions containing 5 mM $NaClO_4$ at selected pH.

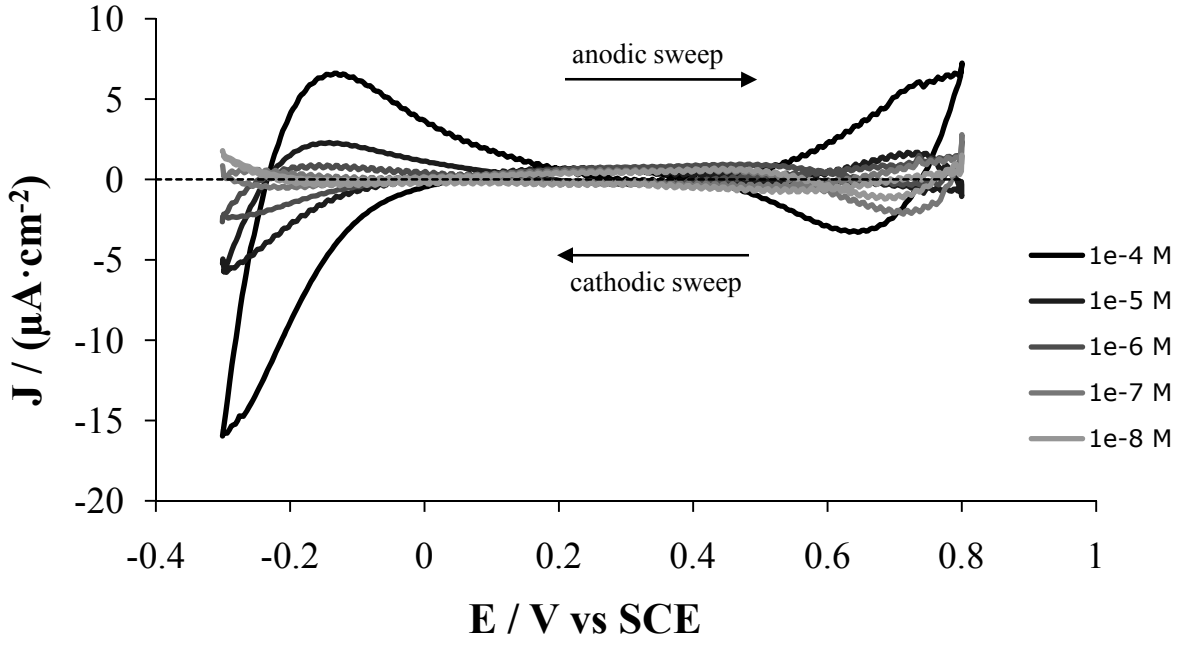

Figure 3.3 Cyclic voltammograms at pH 6.00, phosphate concentrations 10^{-8} – 10^{-4} M after subtraction of $NaClO_4$ voltammograms.

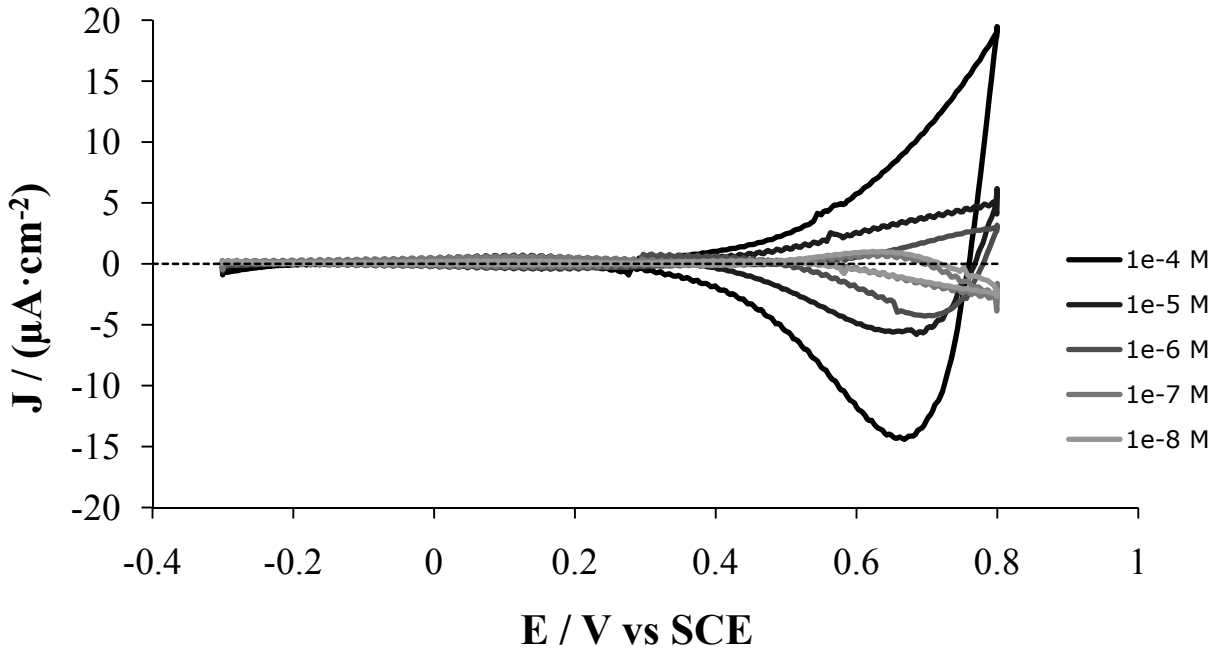

Figure 3.4 Cyclic voltammograms at pH 8.75, phosphate concentrations 10^{-8} – 10^{-4} M after subtraction of $NaClO_4$ voltammograms.

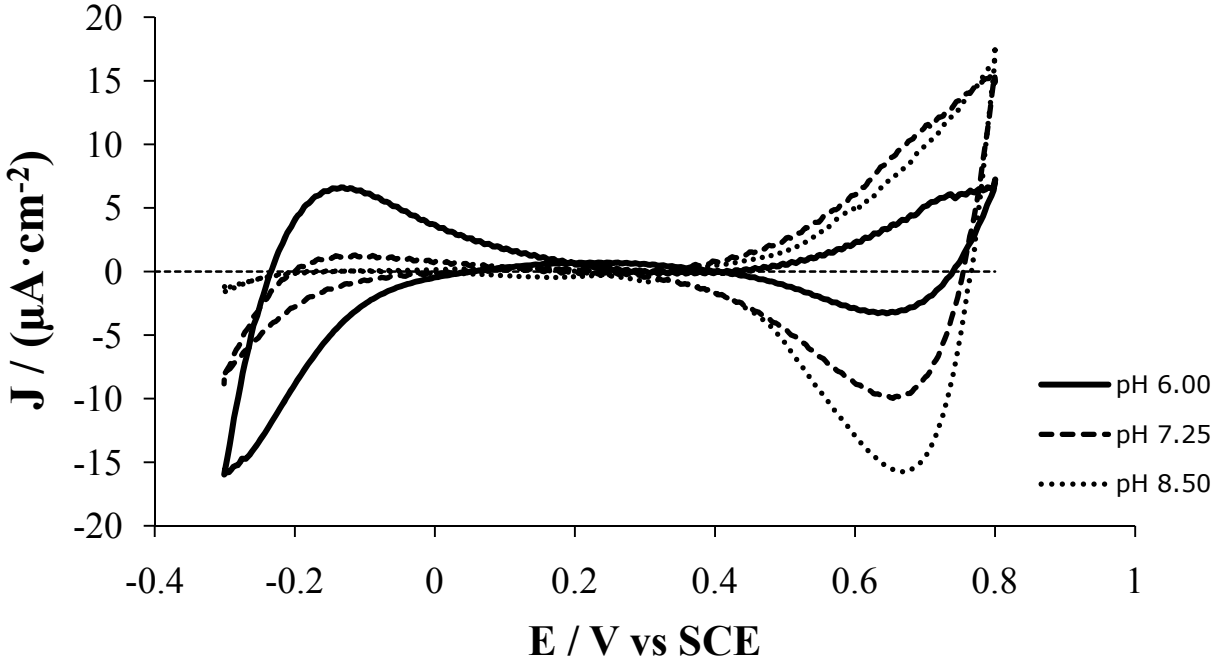

Figure 3.5 Cyclic voltammograms of 10^{-4} M phosphate at three pH values after subtraction of $NaClO_4$ voltammograms.

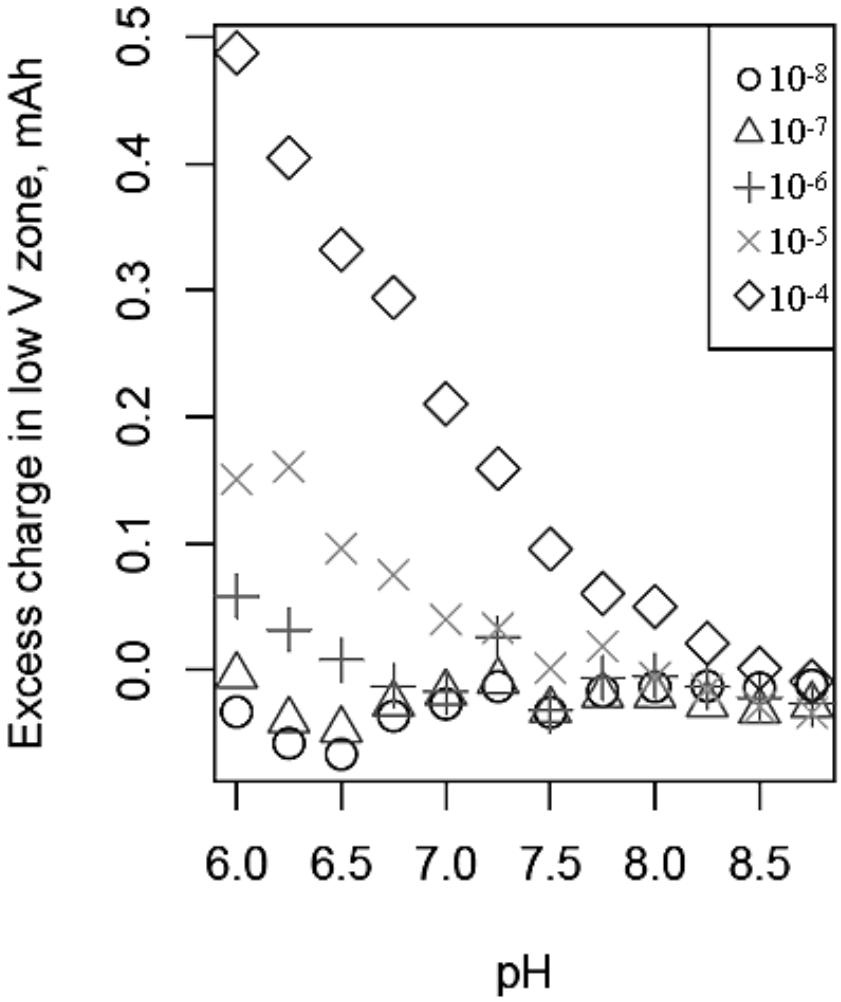

Figure 3.6 Excess charge held by the hematite electrode in phosphate-containing solutions (10^{-8} – 10^{-4} M) in the low voltage zone, E < 0.2 V vs. SCE.

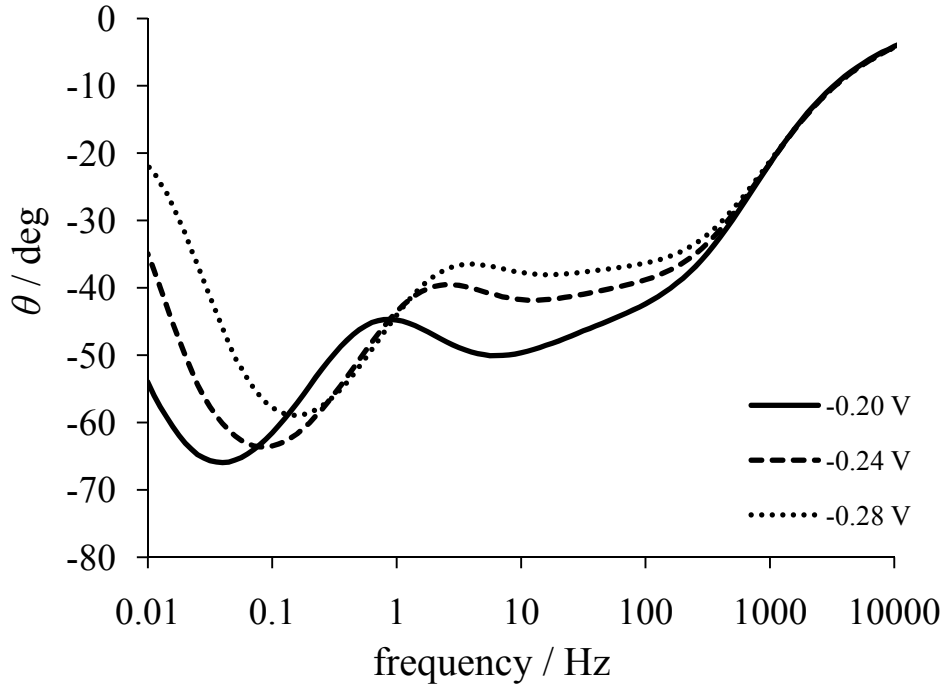

Figure 3.7 Effect of bias potential on the Bode phase plot obtained by EIS in 5 mM $NaClO_4$, pH 7.00.

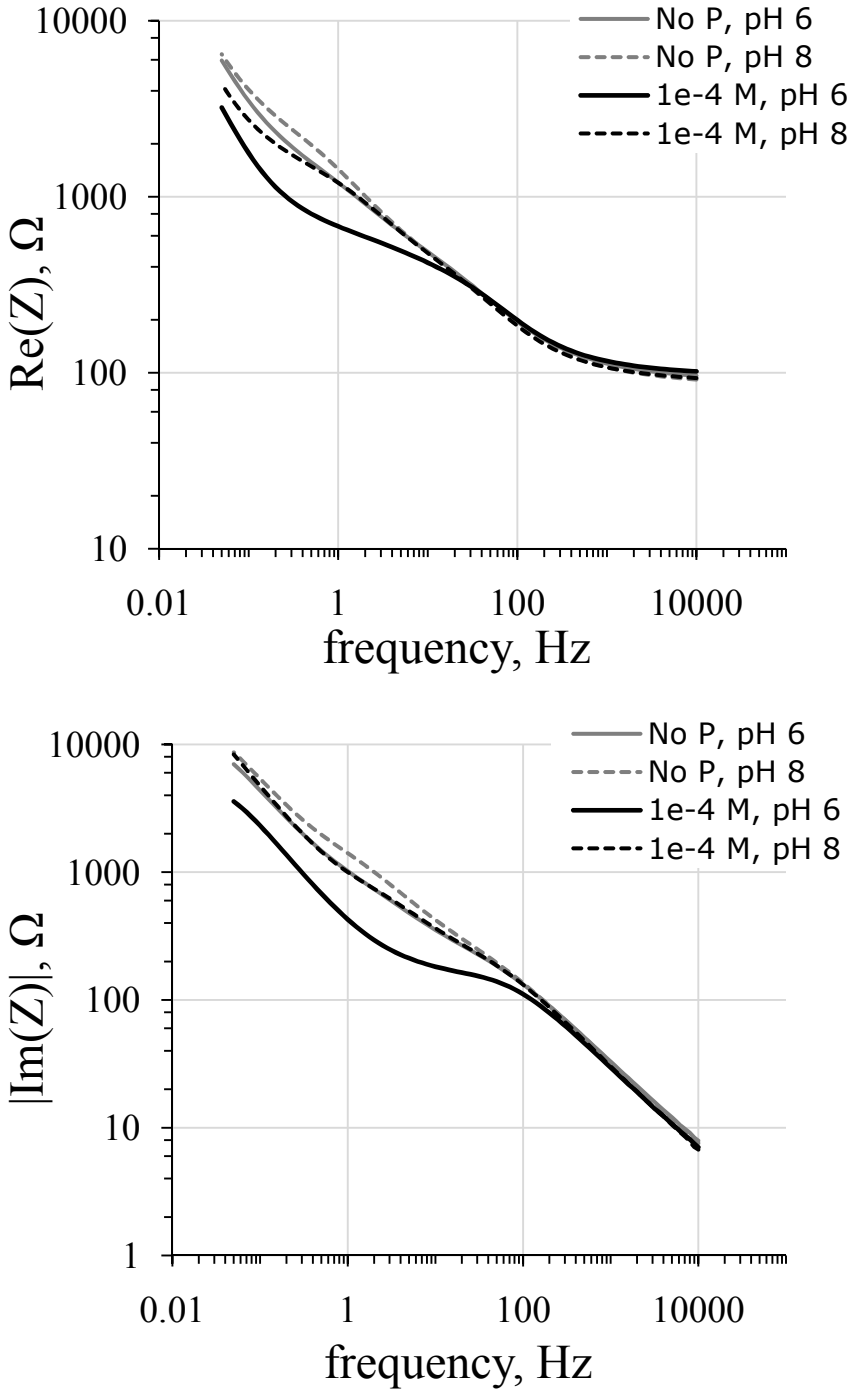

Figure 3.8 Real (*above*) and imaginary (*below*) impedance of a phosphate-free and 10^{-4} M phosphate system at pH 6.00 and 8.75.

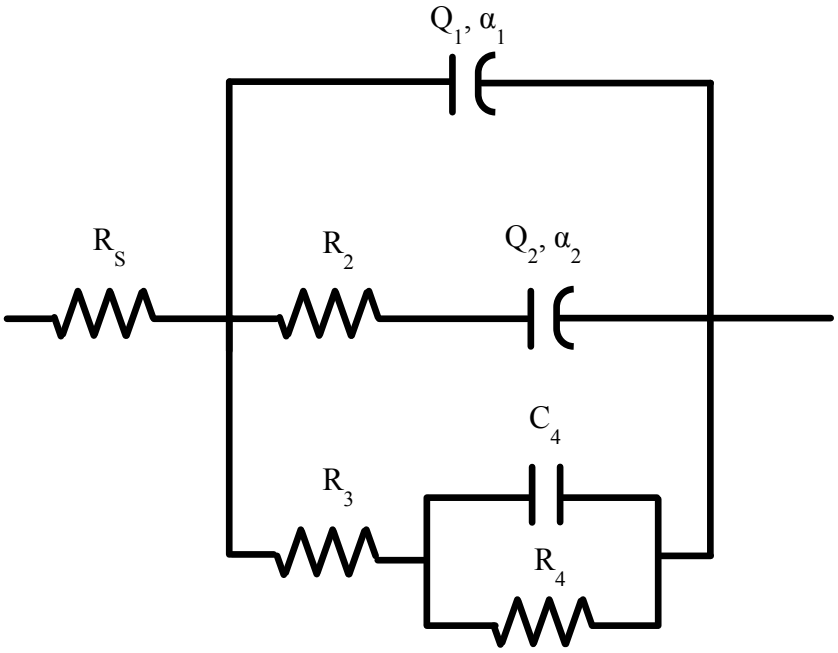

Figure 3.9 Graphical representation of the equivalent circuit analog for the hematite electrode.

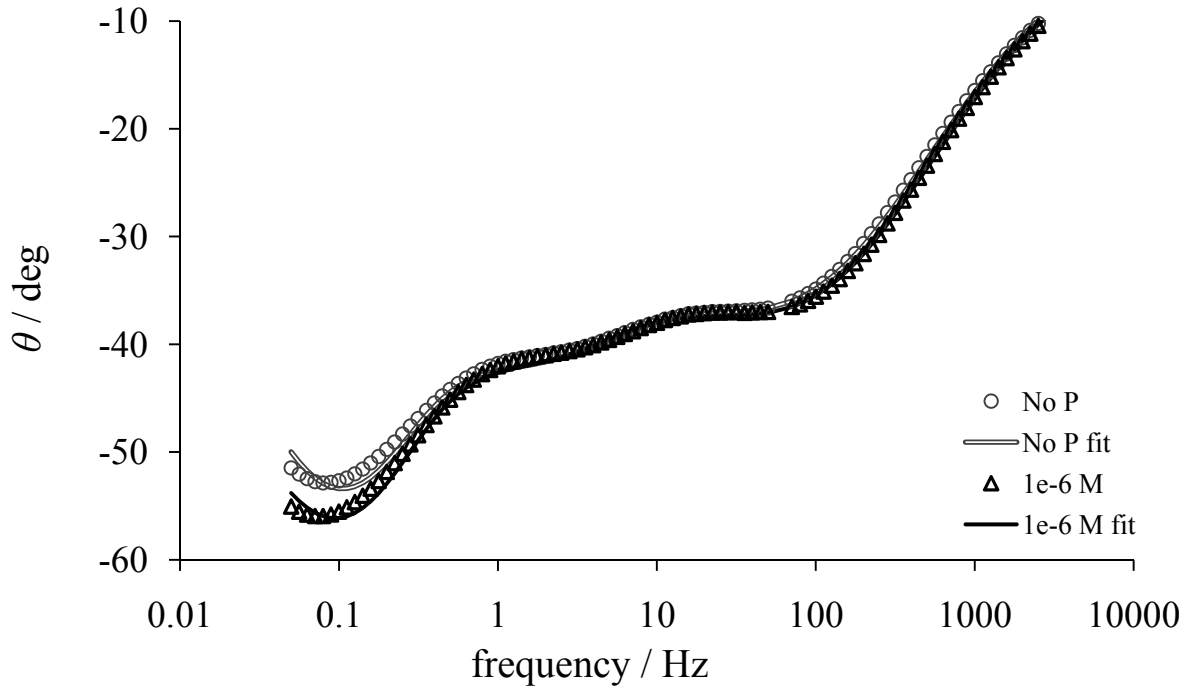

Figure 3.10 Bode phase plot of experimental EIS data with best fit from the equivalent circuit for 5 mM $NaClO_4$ and 10^{-6} M phosphate, pH 7.00.

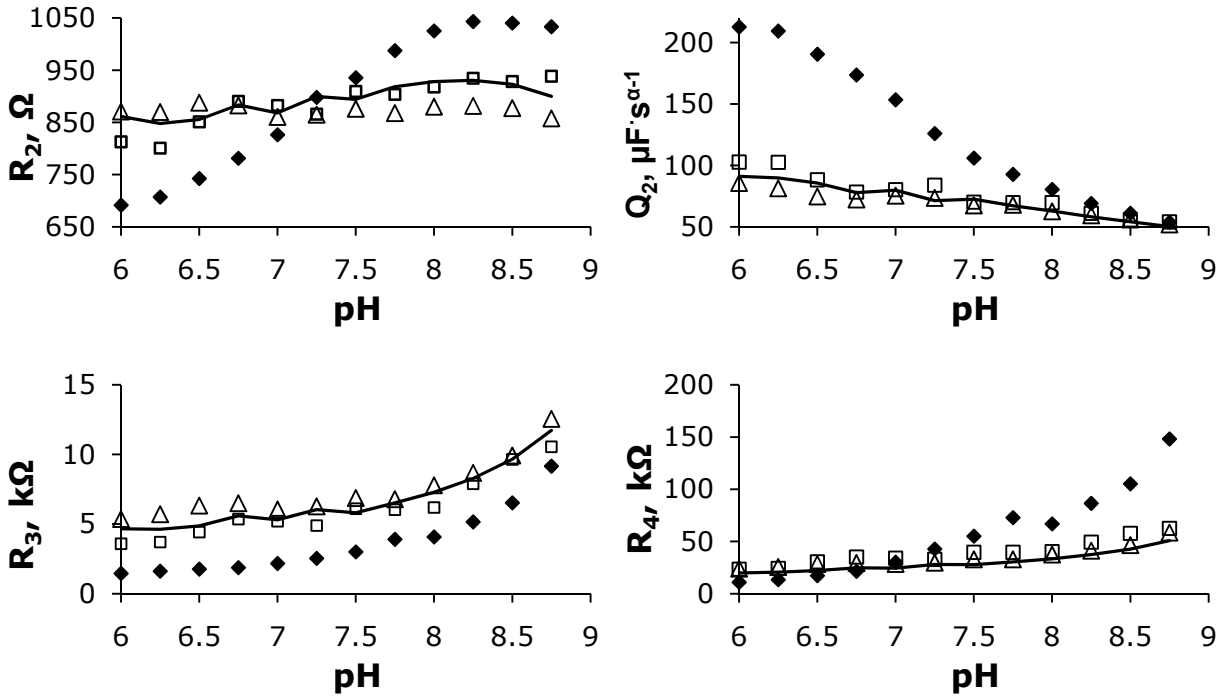

Figure 3.11 Values of selected equivalent circuit components R_2, Q_2, R_3, and R_4 as a function of pH and C_{PO4}. Phosphate concentrations are △ 10^{-8} M, □ 10^{-6} M, ♦ 10^{-4} M. The solid line represents phosphate-free system values.

CHAPTER 4

ELECTROCHEMICAL RESPONSE OF TITANIA, ZIRCONIA, AND ALUMINA ELECTRODES TO PHOSPHATE*

* A version of this chapter will be submitted to *Sensors and Actuators B: Chemical*, with R. E. Pérez-Roa and M. A. Anderson as co-authors.

Abstract

To aid in the development of an electrochemical orthophosphate sensor, metal oxides were tested for sensitivity to the phosphate analyte. Titania (TiO_2), zirconia (ZrO_2) and alumina (γ-Al_2O_3) coated electrodes produced via sol-gel methods were compared as sensing materials for this purpose. Perturbations of cyclic voltammograms and electrochemical impedance spectra indicated the effects of phosphate addition over the pH range 6.00 – 8.75. Potential cycling of the titania and zirconia electrodes produced cathodic features that showed competition between the phosphate ion and OH^-. However, the alumina electrode did not show a voltammogram response to phosphate, possibly indicating an electrochemical process different from the other metal oxides. Both lower pH and greater phosphate concentration increased capacitance for all metal oxides tested. No Faradaic reaction was evident from the high frequency behavior in Nyquist plots, although features typical of porous electrodes were evident for titania and alumina. Titania and zirconia electrodes produced a lin-log relationship between the phase of impedance and phosphate concentration, and the relationship was strong in titania over the full pH range tested. Titania also showed lesser memory effects with respect to the signal coming from phosphate adsorption than did zirconia. For these reasons, titania is recommended for future study as a

material that may be applied for purposes of developing a sensor for submicromolar orthophosphate.

4.1. Introduction

Phosphorus was shown to be a limiting nutrient for algal growth in lake experiments by Schindler in the 1970s [1, 2]. Excess phosphorus input can lead to states of eutrophication in aquatic bodies, where algal blooms may imbalance local ecosystems to the detriment of overall water quality. The most easily metabolized forms of phosphorus by cells are the inorganic orthophosphates, primarily HPO_4^{2-} and $H_2PO_4^-$ at environmental pH. U.S. Environmental Protection Agency guidelines have established recommendations for phosphate levels in lakes to be less than 0.05 ppm as P [3], corresponding to 1.6 μM phosphate. However, maximum phosphate levels to avoid eutrophic conditions may be lower than this; the Organisation for Economic Cooperation and Development (1982) suggested an upper limit for non-eutrophic lakes at 0.035 ppm in total phosphorus [4]. Actual phosphate concentrations may be 2 – 3 orders of magnitude less than the total phosphorus, corresponding to healthy lake water phosphate concentrations possibly at nanomolar (10^{-9} M) levels [5]. Thus, practical real-time, in situ monitoring of water that is not highly eutrophic would require a sensor that can measure submicromolar phosphate. Unfortunately, a sensitive phosphate sensor for these real-world applications does not yet exist.

Generally, phosphate concentrations are determined via reagent-based colorimetric methods with a UV-visible light spectrophotometer, in a laborious process that normally takes place away from the water source. Portable commercial colorimetric phosphate sensors have been developed with detection limits 0.05 – 0.10 $mg \cdot L^{-1}$ P as phosphate (1.6 – 3.2 μM) [6].

These reagent-based optical methods are more useful for wastewater monitoring where phosphate concentrations are often more than one micromolar. More sensitive colorimetric phosphate detection methods include liquid waveguide capillary cells (LWCC) with 1 - 2 meter long path lengths for light through the sample [7-10], and the magnesium induced co-precipitation (MAGIC) method that includes pre-concentration steps [9, 11-13]. However, these methods may be impractical for common use in real water samples due to bulky equipment and long wait times for chemical equilibrium to be established with the reagent.

In contrast to reagent-based phosphate detection, some researchers investigated electrochemical sensors for phosphate, with a summary of earlier efforts detailed in Engblom (1998) [14]. Many of these have been based on voltammetric changes upon phosphate adsorption, with detection limits still generally above one micromolar. Some advancement was made with amperometric biosensors that detect a current change with reduction of O_2 catalyzed by enzyme-bound phosphate, and these are proposed to detect submicromolar phosphate [15]. However, the sensor would have limited applications in a lake water system because the sensor environment needs to be buffered to prevent degrading the enzyme coating.

Phosphate specifically adsorbs to metal oxides, hydroxides, and oxyhydroxides (collectively called metal (hydr)oxides) at the solid/solution interface in a space charge region referred to generally as the electrical double layer. Specific, inner-sphere adsorption of phosphate onto these minerals changes surface electrochemistry. Electrophoretic mobility experiments show a shift downward in the isoelectric pH with phosphate adsorption for iron (hydr)oxides [16-25], aluminum (hydr)oxides [26], titanium dioxide [26,27], and zirconium dioxide [28]. On these materials, the phosphate anion can be considered potential-determining, as the

electrochemical properties of the oxide surfaces are chemically modified by phosphate adsorption.

Nanoporous materials produced via sol-gel methods can yield a high specific surface area, sometimes hundreds of m^2 per gram. With this large exposure of a mineral surface to analyte, capacitive effects of ion adsorption into the electrical double layer of an electrode may be amplified. Using an electrode with a nanoporous hematite (α-Fe_2O_3) coating, submicromolar phosphate caused measurable perturbations in results from cyclic voltammetry (CV) and electrochemical impedance spectroscopy (EIS) [cf. Chapter 3] over a range of circumneutral pH. Response of the hematite electrode with phosphate indicated that metal oxide coatings with high surface areas may be applied for sensitive phosphate detection. In that study, metal oxides other than hematite were not tested. To build upon earlier work, we have investigated the effects of phosphate on TiO_2, ZrO_2, and γ-Al_2O_3 coated electrodes so as to compare these results with our earlier hematite studies. As an electrochemical sensor should have high sensitivity to the analyte, applicability over a range of pH, and negligible hysteresis of measurement, we investigate these issues in order to judge which, if any, of these metal oxides is optimal for electrochemical phosphate sensing.

4.2. Experimental

4.2.1. Sol Preparation

Titania (TiO_2) sol was produced in a method detailed in Xu [29]. A 1:12 dilute aqueous solution of titanium isopropoxide, $Ti(OPr^i)_4$ (Aldrich), was acidified with concentrated HNO_3, and the precipitate was stirred with a Teflon stir bar continuously for three days at room temperature until peptized into a stable titanium dioxide nanoparticulate suspension. A portion of

the colloidal suspension was dialyzed twice in 18 MΩ·cm ultrapure H_2O, and the solution was then passed through a 0.45μ filter membrane to allow only nanoparticulate colloids in the final suspension (sol). The titania sol had a final density of 20.0 $g \cdot L^{-1}$ with a pH of 3.56. TiO_2 particles were found to have mean diameter 27.1 nm (Malvern Zetasizer). Zirconia (ZrO_2) sol was prepared with HNO_3 acidified and peptized 1:15 dilute aqueous zirconium propoxide, $Zr(OPr^n)_4$ (Gelest, Inc.) in a method analogous to preparation of the titania sol. This method produced a zirconia sol at pH 2.27 with particulate density of 14 $g \cdot L^{-1}$ and mean particle size 40.1 nm. Both sols were stored in glass bottles at room temperature.

An alumina (AlOOH) sol was produced from aluminum tri-sec-butoxide, ATSB (Gelest, Inc.), in a method adapted from Anderson (1988) [30]. 121 mL of ATSB were diluted with 129 mL 2-butanol, and the mixture added to 1036 mL of 80˚C heated ultrapure water and stirred with a Teflon stir bar for 1 - 2 hours. The stirred solution was acidified with 22.7 mL of 1.6 M HNO_3, and 2-butanol was evaporated from the resulting suspension by mixing at 80˚C for 4 hours. The remaining colloidal solution was refluxed for 12 hours, then allowed to cool and passed through: 1) a Type A/E glass fiber filter, 2) a 8μ filter membrane, and 3) a 0.45μ filter membrane. The final sol had a pH of 3.74, with density of 34.5 $g \cdot L^{-1}$ and mean particle size 26.2 nm. The sol was stored in a glass bottle at room temperature.

4.2.2. Electrode Preparation and Characterization

Coated electrode materials were prepared by dip-coating 1.0 cm by 5.0 cm by 0.5 mm segments of conductive 99.0% nickel foil in titania, zirconia, or alumina sols followed by thermal treatment. Prior to coating, the Ni foil was finely sanded, rinsed with 0.1 M NaOH and 18 MΩ·cm ultrapure water, placed in 2% HNO_3 solution for 10 min and again rinsed with

ultrapure water. The Ni support was heated at 250˚C for 2 h to improve hydrophilicity (wetting) of the surface for a thinner, more consistent coating. Upon cooling, the supports were dip-coated by lengthwise placement into and subsequent withdrawal from the sol at 5.0 $mm \cdot s^{-1}$. The coating was then allowed to air dry into a supported xerogel at 22˚C. For zirconia and alumina electrodes, the dip-coating process was repeated for a total of 5 (zirconia) or 10 (alumina) coats. The xerogel film was fired at 500˚C for ten hours to sinter the porous metal oxide ceramic coating onto the substrate. The pore size distribution and specific surface area of ceramics fired at these temperatures and times were determined from the N_2 adsorption isotherms at 77 K using a Micromeritics ASAP 2010 analyzer. Electrode surfaces were examined with a scanning electron microscope (SEM) on a LEO 1530 FESEM.

4.2.3. Chemicals

Aqueous solutions of orthophosphates were prepared with Na_2HPO_4 by serial dilution in a series of carefully pre-cleaned volumetric flasks. Each solution contains $NaClO_4$ electrolyte to maintain uniform ionic strength while the electrode response to phosphate were tested. All chemicals were chosen for specifications of negligible phosphate impurities.

In the first set of experiments, phosphate solutions were prepared in a sodium perchlorate electrolyte. 99.99% trace-metal basis $NaClO_4 \cdot xH_2O$ was added to a final concentration of 5 mM in solutions in the 10^{-8} M to 10^{-4} M phosphate range. Between electrochemical measurements at each phosphate concentration, solutions were titrated in 0.25 pH unit increments between pH 6.00 - 8.75 with microliter quantities of 0.1 M solutions of ACS analytical grade NaOH and $HClO_4$. Due the contribution of the phosphate ion, 10^{-4} M phosphate increased the ionic strength somewhat over the background electrolyte; the effect is an ionic

strength increase of 2.2% at pH 6 and 5.0% at pH 8.75. Ionic strength was increased by less than 1% for phosphate concentrations of 10^{-5} M and lower.

4.2.4. Apparatus and Electroanalytical Procedure

The electroanalytical protocol was similar to the one used in a previous study of the effects of pH and phosphate concentration on the electrochemical response of a hematite electrode [cf. Chapter 3]. Briefly, a three electrode electrochemical apparatus consisted of the thin-film working electrode, a saturated calomel reference electrode (SCE) placed 5 mm away from the working electrode, and a Pt counter electrode that completed the circuit in 250 mL of blank or phosphate-containing electrolyte solution in a pre-cleaned glass container. Cyclic voltammetry and electrochemical impedance spectroscopy techniques utilize a Princeton Applied Research VMP2-Z potentiostat with starting parameter inputs and data analysis using BioLogic EC-Lab V10.18 software.

In experiments testing metal oxide electrode response to phosphate in 5 mM $NaClO_4$, the three electrode system is first placed in 250 mL phosphate-free perchlorate solution titrated with $HClO_4$ to pH 6.00, kept in an illuminated environment at 22˚C. The electrode is scanned 200 times at the rate 150 $mV \cdot s^{-1}$ over the voltage window -0.3 V – 0.8 V vs. SCE; this initial cycling was found to provide more consistent cyclic voltammograms for an iron oxide electrode at pH 7.00, attributed to clearing the surface of interfering ions without degrading the oxide coating [31]. The system was left at rest for 2 min to return to the open circuit potential then was cyclically scanned five times with a 150 $mV \cdot s^{-1}$ scan rate over -0.3 V – 0.8 V vs. SCE, with output saved from the fifth scan. For the EIS phase of the experiment, the voltage was first held at -0.24 V vs. SCE for 3 min, then an alternating sinusoidal peak-to-peak potential of ± 20 mV

was applied over a bias potential of -0.24 V vs. SCE. The recorded frequency range for this sinusoidal potential application was 10 kHz to 0.05 Hz. After the CV and EIS measurements of the pH 6.00 phosphate-free perchlorate solution, the pH is titrated upward 0.25 units with 0.1 M NaOH and the sample again underwent five CV cycles and an electrochemical impedance scan over the frequency range. These steps were repeated until measurement at a final pH of 8.75. Then, the 5 mM $NaClO_4$ solution was replaced by 250 mL of 10^{-8} M phosphate (in 5 mM $NaClO_4$) at pH 6.00, and the steps of 1) five CV cycles, 2) EIS measurement, 3) pH raised by 0.25 units, were repeated for this phosphate concentration until pH 8.75. The solution was again replaced, and the measurements were made for 10^{-7} M, 10^{-6} M, 10^{-5} M, and 10^{-4} M phosphate. Memory effects for the titania and zirconia electrodes in phosphate were analyzed by EIS. For one electrode of each metal oxide, impedance measurements were made in 250 mL of solutions of phosphate in 5 mM $NaClO_4$ electrolyte titrated to pH 8.50. Phosphate solutions were 10^{-9} – 10^{-6} M in half-decade molar log units of concentration, and five potential cycles over -0.3 V – 0.8 V vs. SCE between each concentration measurement were measured. Lin-log standard curves were produced plotting θ vs. phosphate concentration at a frequency predetermined to be well correlated with phosphate; this was 10 Hz for titania and 0.2 Hz for zirconia. After performing the test at 10^{-6} M, the electrodes were placed and re-tested in a 250 mL beaker of 5 mM $NaClO_4$, pH 8.50. The resultant θ at the chosen frequency was compared to the standard curve for a measure of recovery of pristine electrochemical signal.

4.3. Results and Discussion

4.3.1. Electrode Coating

Unsupported titania, zirconia, and alumina produced from sols as prepared by those in our studies have been previously investigated for characteristics such as mineral structure, specific surface area, and porosity. However, the characteristics of films less than 1 μm thick bound to a substrate may be different from the unsupported ceramic [32]. It is not trivial to obtain information for specific surface area and porosity in supported thin porous films. Still, characterizing unsupported films can provide qualitative information at minimum.

Titania sol fired at 500˚C has been confirmed by X-ray diffraction studies to be primarily anatase TiO_2 in structure, with a small fraction of rutile TiO_2 structure that becomes more predominant at sintering above 500˚C [32]. Zirconia sol fired at 500˚C produced a cubic and/or tetragonal ZrO_2 structure [32]. Alumina sol sintered at 500˚C resulted in a gamma phase aluminum oxide (γ-Al_2O_3) ceramic [30]. All three metal oxides were categorized with BET surface area analyses as mesoporous. The titania unsupported film in this work had a specific surface area of 75.7 $m^2 \cdot g^{-1}$ with an average pore diameter of 6.90 nm and 35.5% intra-agglomerate porosity. The unsupported zirconia ceramic had pores with mean diameter 4.80 nm, but it had a low specific surface area (11.0 $m^2 \cdot g^{-1}$) and had only 6.38% porosity. However, where the specific surface area and porosity can be very low for unsupported ZrO_2 fired at temperatures above 400˚C, ZrO_2 thin films on a substrate are believed to have greater surface area and porosity, possibly due to interactions between the support and the thin film limiting mobility of the mineral required for the collapse of the nanoporous structure [32]. Alumina had the greatest porosity and smallest pores of the three oxides. Unsupported alumina had a BET specific surface area 290.4 $m^2 \cdot g^{-1}$, mean pore diameter 3.91 nm, and 52.9% porosity.

Coatings were evaluated with a scanning electron microscope to view the homogeneity of the electrode surface. A supported titania film on the nickel substrate (Figure 4.1) showed pits where there was more roughness or porosity than could easily be seen for other parts of the ceramic, and the ceramic had minor surface cracks. The supported zirconia ceramic film (Figure 4.2) and alumina film (Figure 4.3) both showed surface pores or roughness, although the alumina had a finer structure that would provide a greater surface area. The thickness was difficult to determine for a thin film on a rough substrate. Thickness of metal oxide thin films is dependent on the substrate, solvent and nanoparticulate density in the sol, number of dip-coats, withdrawal speed during dip-coating, as well as firing temperature and time [33]. Measurement of thickness for titania, zirconia, and alumina films were attempted using scanning electron microscopy. However, cross-sectional images from the electrode did not provide conclusive information. Ellipsometry studies by Innocenzi et al. (1992) [34] et al. found film thickness in the 60 – 115 nm range for titania and 65 – 85 nm range for zirconia for a single dip coat on a glass substrate, used as a surrogate for the Ni substrate. Using SEM, Ayral et al. [35] determined a 50 nm thick alumina film for a single dip coat on smooth glass. Based on trends in film thickness with withdrawal speed, sol density and number of dip-coats, our oxide films on these substrates (with 1 – 10 dip coats per electrode) are estimated to have a total thickness in the range of 100 – 500 nm.

Our and others' studies have determined isoelectric pH for metal oxide ceramics produced via sol-gel methods from the same sol precursors and with the same sintering temperatures [32, 36-38]. The isoelectric pH for these oxide ceramics from these studies are in the order alumina > hematite > zirconia > titania. Values and references are listed in Table 4.1.

4.3.2. Electrochemical Analysis

4.3.2.1. Titania

In the absence of phosphate, titania coated electrodes produced cyclic voltammograms with anodic and cathodic features that were perturbed by pH titration or addition of phosphate. The reduction of Ti(IV) to a Ti(III) product within the film is not thermodynamically favored within the potential cycling envelope (-0.3 – 0.8 V vs. SCE) over any of the pH range tested [39]. As was the case with hematite, adsorption and desorption of specifically adsorbing ions appeared to change current response to a potential sweep without a classic Nernstian phenomenon. In the case of a perchlorate only system (Figure 4.4), cyclic voltammograms showed charging effects at the switching potentials of -0.3 V and +0.8 V vs. SCE. This behavior was generally independent of pH. However, in the cathodic sweep, the perchlorate system produced a curve that not only increased in area (*i.e.*, magnitude of current over the voltage scan) with greater pH but also showed evidence of a cathodic peak at pH values greater than 8.00, possibly related to OH^- desorption from the surface.

In the region of the cyclic voltammogram above 0.1 V vs. SCE, response of the titania electrode to phosphate was dependent on pH. At high pH, a cathodic peak present in the $NaClO_4$ system at 0.35 V vs. SCE became less prominent in 10^{-6} M phosphate (Figure 4.5). The phosphate anion may compete with OH^- at the surface of titania, and a peak due to electrosorption of phosphate and concomitant desorption of OH^- might be decreased when the phosphate is comparable to OH^- in concentration. Furthermore, at low pH, 10^{-6} M phosphate produced a cathodic peak closer to the positive switching potential, and this peak disappeared at higher pH, when there was greater OH^- concentration. Thus, it seems likely that the two ions produced their own peaks. At 10^{-4} M phosphate (Figure 4.6), the cathodic peak attributed to OH^-

desorption was no longer discernable, although the hydroxide ion might have caused the phosphate cathodic peak to appear to be shifting to lower potentials.

In a cyclic voltammogram of the titania electrode at pH 6.00 (Figure 4.7), the cathodic sweep behavior attributed to phosphate on the surface of titania showed current response that was dependent on phosphate concentration over the range 10^{-8} M – 10^{-4} M. This correlation continued through pH 7.25 (Figure 4.8). At greater pH, when OH^- was at concentrations that could compete with phosphate, the correlation was no longer clear over a wide range of phosphate levels. At pH 8.50 (Figure 4.9), lower phosphate concentrations produced cathodic current from the titania electrode that appeared as a mix of the phosphate and OH^- desorption peaks, where at 10^{-5} M and 10^{-4} M the phosphate peaks predominated. Therefore, with the titania electrode, cyclic voltammetry could not easily be used as a method to monitor phosphate concentration over a basic pH region.

Titania electrodes were further analyzed with electrochemical impedance spectroscopy to analyze AC response of the material in perchlorate and phosphate solutions. Graphical Nyquist plots mapped the complex impedance **Z** in terms of the negative of its imaginary component versus its real impedance term where:

$$\mathbf{Z} = Z_{\text{real}} + jZ_{\text{imag}} \tag{1}$$

in which Z_{real} and Z_{imag} are the real and imaginary components of impedance, and j is the imaginary unit equal to $\sqrt{-1}$.

The Nyquist plots in perchlorate solution at pH 6.00, 7.25, and 8.50 (Figure 4.10) showed a pH-dependence with a blocking-type (*i.e.*, capacitor-like) electrode behavior, as indicated by a

steep slope at mid to low frequencies. However, there appeared to be low frequency reactive-type (*i.e.*, Randles circuit-like) behavior, as the Nyquist plot approached semicircular curvature at low frequencies. The curvature of the Nyquist plot appeared to be more significant at greater pH. With careful examination of the plot at high frequencies (Figure 4.11), one could detect a bend that often occurs in Nyquist plots for porous electrodes, including nanoporous metal oxides [40]. However, at all pH, there was no apparent high-frequency semicircular arc that would have been indicative of Faradaic charge transfer. Addition of phosphate to the system also produced Nyquist plots that also did not appear to have a high-frequency semicircular arc. Nelson et al. (2000) [41] did observe the high-frequency arc in mesoporous TiO_2 material, but they found that addition of phosphate eliminated this feature. The disappearance was attributed to a reduction in electron transfer resistance. Also in that work, increased acidity and phosphate adsorption were also found to have similar effects on conductivity [41]. At a constant pH, there was a steeper slope in the Nyquist plot with increasing phosphate concentration, indicating that the electrode was be more capacitive over mid and low frequencies (Figure 4.12). This increase in capacitive behavior was similar to the effect of lowering pH in the phosphate-free system. Capacitive behavior is indicative of charge separation at the electrochemical double layer, and phosphate adsorption onto the oxide might be expected to produce this feature. Although inner-sphere adsorption of phosphate onto titania does occur above the isoelectric pH [42] of 6.0 (median for all anatase samples [43]) or 6.7 (for sol-gel derived ceramic [38]), surface coverage is greater at lower pH [42]. The charge separation between the surface and the anion was likely more pronounced at lower pH, when the oxide has greater surface protonation. Low pH, high phosphate solutions resulted in the most capacitive electrode behavior of all the solutions tested.

Bode phase plots were produced as a graphical representation of the experimentally determined angular phase of impedance (θ) versus the applied frequency (f), where:

$$\theta = \tan^{-1}\left(\frac{Z_{imag}}{Z_{real}}\right) \quad (2)$$

In our previous studies involving a hematite electrode, Bode phase plots at the bias voltage -0.24 vs. SCE showed dependence of θ on pH and phosphate concentration [cf. Chapter 3]. In that case, there was a frequency (0.2 Hz) at which θ showed little pH dependence while still retaining a strong correlation to phosphate concentration. In contrast, a Bode phase plot of the titania electrode in 5 mM $NaClO_4$ (Figure 4.13) indicated that impedance has pH dependence over the full lower frequency range (0.1 - 100 Hz) of a minimum 1.9 degrees between pH 6.00 and 8.75. The electrode was more capacitive at low pH and in high phosphate concentration, as evidenced by a more negative θ. The phase of impedance using the titania electrode can be well correlated to 10^{-8} M – 10^{-4} M phosphate with the same lin-log relationship seen for the hematite electrode. In this case, 10 Hz is the frequency at which θ was recorded. Unlike in cyclic voltammograms, the correlation between electrochemical signal and phosphate concentration remained strong at high pH, with $R^2 \geq 0.919$ or greater for the full pH range 6.00 – 8.75. However, the pH would have to be known and constant in order to use this 1-frequency calibration. For example, a Bode phase plot of the titania electrode at pH 8.50 (Figure 4.14) had $R^2 = 0.998$ for the lin-log correlation between θ and 10^{-8} – 10^{-4} M phosphate. However, the shift of θ between 10^{-8} and 10^{-4} M phosphate was only 6.28% greater than the shift caused by

adjusting the pH from 8.50 to 6.00 while keeping phosphate constant. Still, a 1-log unit increase in phosphate concentration shifted θ more than a decrease of one pH unit.

4.3.2.2. Zirconia

The zirconia electrode in perchlorate and phosphate solutions gave current response similar to the titania electrode in potential cycling and electrochemical impedance spectroscopy experiments. In cyclic voltammograms, the zirconia electrode in perchlorate solutions of pH 8.00 and greater had a current dip at approximately 0.40 V vs. SCE (Figure 4.15) that was likely the result of OH^- lability. At 10^{-6} M phosphate (Figure 4.16), that same cathodic peak is still present in the cyclic voltammogram at high pH, but another peak, attributed to the added phosphate, occurred closer to the positive switching potential. At 10^{-4} M phosphate (Figure 4.17), the greatest concentration tested, the only cathodic peak appeared to either only be the result of phosphate or alternatively was a blend of phosphate and OH^- effects. Again, these features indicated competition between the two anions. At pH 6.00, a cyclic voltammogram gave evidence of a section of the high potential region where current response could be tied to phosphate concentration over the 10^{-8} – 10^{-4} M range (Figure 4.18). However, unlike titania, the straightforward correlation between phosphate and a cathodic current did not continue from the low into the intermediate pH range.

Patterns in the electrochemical impedance spectra of the zirconia electrode were often similar to those of the titania electrode. Still, some differences arose from dissimilarity in porosity between the two metal oxide films. In 5 mM $NaClO_4$, the zirconia electrode produced almost no high-frequency bend in a Nyquist plot that would have been indicative of electrolyte penetration into pores [44, 45]. This agreed with the earlier finding of low specific pore density

for the unsupported ceramic. However, like titania, the zirconia electrode displayed non-ideal capacitor-like behavior at intermediate frequency and some evidence of reactive-type curvature at low frequencies. In acidic solutions, the electrode had more capacitive θ as viewed in Bode phase plots (Figure 4.19). Nyquist plots of the electrode in perchlorate showed a reduction in the steepness of the curve over mid – low frequencies with higher pH, (Figure 4.20) but addition of 10^{-4} M phosphate reduced the prominence of this feature in a constant pH solution (Figure 4.21). Again similarly to TiO_2, phosphate adsorption onto ZrO_2 is increased at low pH [46], and the zirconia electrode was most capacitive in solutions with both low pH and high levels of phosphate.

As with the titania electrode, it would be difficult to separate what changes in components of capacitance of the zirconia electrode are due to a pH change or due to differences in phosphate concentration. The applied frequency 0.2 Hz produced an impedance phase angle θ that correlated well to phosphate concentration 10^{-8} – 10^{-4} M in the same lin-log relationship that was clear for hematite and titania, with $R^2 \geq 0.914$ for the full pH range tested. However, the resolution among phosphate concentrations was best at high pH. The frequency 0.2 Hz was the same used in an earlier study for the hematite electrode. At pH 8.50, a Bode phase plot representation showed good resolution of 5 mM $NaClO_4$ and the range of phosphate concentrations (Figure 4.22), with $R^2 = 0.981$ in a lin-log fit of the data at this frequency. However, pH would still have to be known in order to use these 1-frequency standard curves for phosphate determination. For example, from a starting solution of 5 mM $NaClO_4$ at pH 8.50, the shift in θ would be the same for an addition to phosphate to 10^{-6} M (pH kept constant) or a pH decrease to 7.00 (phosphate concentration kept constant).

4.3.2.3. Alumina

Cyclic voltammograms of the alumina electrode in perchlorate solution produced very little current and no distinct peaks. However, the magnitude of the anodic and cathodic current increased somewhat at higher pH, when the concentration of adsorbing hydroxide anion was expected to increase (Figure 4.23). At all pH values, addition of phosphate at concentrations as great as 10^{-4} M did very little to perturb the cyclic voltammogram. Phosphate has an equal or greater maximum surface coverage on alumina than iron oxides for samples of similar surface area [47, 48] with decreased surface coverage at increasing pH for both oxides [48], and phosphate specifically adsorbs to both [16, 49]. However, unlike the previously studied case of hematite [31], phosphate adsorption onto the alumina electrode did not appear to influence mobility of charge that would have resulted in differences in voltammograms. This might indicate that perturbations of current response to a potential sweep comprised of more than just chemisorption of the phosphate ion, and electronic properties of the alumina material itself might have played a role in electrochemical response.

Plots of electrochemical impedance spectra of the alumina electrode also showed mid- and low-frequency capacitance trends that were similar to the other oxides tested. However, the magnitude of impedance at low frequencies was approximately twice as great as was the case with titania or zirconia. Sugimoto et al. (2005) [40] attributed highly capacitive behavior in a hydrated RuO_2 as the result of ionic resistance when micropores were not easily accessible. Caldararu et al. (2001) [50] found that proton (H^+) conductivity was the source of electrical conductivity in γ-Al_2O_3 below 400˚C. It seems likely that the pore structure difference of the material is a significant cause of the difference in impedance among the metal oxides. The Nyquist plot of the alumina electrode in 5 mM $NaClO_4$ (Figure 4.24) again had pH-dependent

impedance in the low frequency region, and in Nyquist plots it appeared that all pH over the 6.00 – 8.75 range produced blocking electrode behavior.

Also visible in the Nyquist plot was the high-frequency bend typical of a nanoporous system that had also been seen for the hematite and titania electrodes. High frequency EIS behavior is not mass transfer controlled [51], and the pH independence of this bend indicated that electronic conductance was not altered. Like the other oxides in this study, the Bode phase plot of this system (Figure 4.25) showed that more acidic solutions produced a more capacitive system with more negative θ over the 50 mHz – 100 Hz frequency range, again highlighting the importance of the proton in the electrochemical properties of this and the other oxides. However, θ was somewhat noisy at low frequencies when the impedance was very large, where this was not the case for the other oxides.

Addition of phosphate appeared to still be correlated with more capacitive θ values, but this trend was only easily resolved at 10^{-6} M phosphate concentrations and greater. Although Nelson et al. (2000) [41] found that phosphate increased proton mobility in a TiO_2 film, it is possible that phosphate did not promote this process in alumina to the same extent as the other oxides. This might agree with the finding that little effect on alumina voltammograms occurred when phosphate was added. At pH 8.50, a Bode phase plot of the alumina electrode in phosphate solutions (Figure 4.26) showed evidence that θ at a chosen frequency less than 0.5 Hz could be correlated to phosphate concentration with the same relationship as for the other metal oxides, but 10^{-7} M, 10^{-8} M, and 5 mM $NaClO_4$ were indistinguishable from each other. This low resolution for submicromolar phosphate concentrations continued over the full pH range tested. As with the other oxides, an unprocessed 1-frequency value would not provide enough

information to determine whether the components of impedance were due to a change in pH or an altered phosphate concentration.

4.3.3. Memory Effects

Titania and zirconia electrodes were tested in a perchlorate solution after use in 1 μm phosphate to determine what level of hysteresis, or memory effect, was present using these materials as sensing electrodes at a single pH (8.50). The alumina electrode was excluded from this study because concentrations less than 1 μm phosphate could not be resolved from 5 mM $NaClO_4$. A titania electrode was calibrated from 10^{-9} M to 10^{-6} M phosphate concentration using a plot of θ vs. phosphate concentration at the frequency 10 Hz. The coefficient of determination for the titania standard curve over this phosphate range was 0.938. The subsequent EIS measurement in phosphate-free 5 mM $NaClO_4$ produced a θ correlated to 0.575 nM phosphate in the standard curve. This reduction in signal of over 99.9% showed that a high phosphate measurement may not have a strong hysteresis effect on the titania electrode. The zirconia electrode was also calibrated over the same phosphate range at pH 8.50 with chosen frequency 0.2 Hz, producing a fit with $R^2 = 0.931$. Measurement in phosphate-free solution then gave a measured phosphate concentration of 61.5 nM phosphate, a 93.9% reduction in signal. Thus, the zirconia electrode was less capable than the titania electrode to show signal reversibility after application in solutions with high phosphate levels.

4.4. Conclusion

Electrodes with titania, zirconia, and alumina coatings showed features of electrochemical response to phosphate that could be tied to adsorption of this ion to metal oxides.

Cyclic voltammograms of the titania electrodes indicated a competition between OH^- and the phosphate anion where each may produce distinct cathodic peaks. Electrochemical impedance spectra of the titania electrode gave no evidence of distinct Faradaic charge transfer in the high frequency region, although there was a bend in the high frequency region indicative of this being a electrode with behavior controlled by electrolyte penetration into pores. Zirconia had similar features in the cyclic voltammogram and a similar absence of charge transfer features in a Nyquist plot. However, the zirconia electrode was not highly porous and did not produce the high frequency bend in a Nyquist plot seen for porous electrodes. The alumina electrode had a relatively featureless voltammogram that was not much affected by phosphate addition. This absence of perturbation with the alumina electrode hinted that phosphate adsorption processes on titania and zirconia materials with applied voltage may be more complex than simple chemisorption.

In all three tested metal oxide electrodes, an increase in phosphate produced more capacitive features in the low frequency region of impedance spectra. At a chosen applied frequency of 10 Hz, the titania electrode had a lin-log correlation between the phase of impedance and 10 nM – 0.1 mM phosphate over the pH range 6.00 – 8.75 with $R^2 \geq 0.919$. At 0.2 Hz, the zirconia electrode also had a lin-log correlation between phase and phosphate levels of $R^2 \geq 0.914$ over the pH range, but the resolution among concentrations was not as great at low pH. Phosphate concentration could not be resolved by the alumina electrode at any pH using a one-frequency method. However, a decrease in pH also produced more capacitive features in all tested electrodes. Using the one-frequency method, the resolution between log-unit phosphate concentrations in a standard curve is not great enough to ignore all effects of pH on impedance when the pH is unknown. In a case of constant pH (8.50), the correlation curve could still be

used to determine the level of hysteresis in the titania and zirconia electrode. The titania and zirconia electrodes showed a reduction in signal of 99.9% (titania) and 93.9% (zirconia) when calibrated to 1 μM phosphate and then tested in phosphate-absent 5 mM $NaClO_4$. Based on these findings, it appeared that the titania electrode is the best choice of these three for further study of a phosphate-sensitive electrode, either by itself or in conjunction with a hematite electrode (that was found in earlier work to have selectivity for phosphate over competing ions such as sulfate and carbonates). However, a more intensive investigation of impedance results may be required to distinguish the effects of phosphate from those of altered pH.

References

[1] Schindler, D. W. Eutrophication and recovery in experimental lakes: implications for lake management. *Science* **1974**, *184*, 897–899.

[2] Schindler, D. W. Factors regulating phytoplankton production and standing crop in the world's freshwaters. *Limnology and Oceanography* **1978**, *23*, 478–486.

[3] U.S. Environmental Protection Agency *Phosphorus Water Quality Standards Criteria Summaries: A Compilation of State/Federal Criteria*; Washington DC, 1988.

[4] Organisation for Economic Cooperation and Development *Eutrophication of Waters, Monitoring, Assessment and Control*; Paris, 1982.

[5] Hudson, J. J.; Taylor, W. D.; Schindler, D. W. Phosphate concentrations in lakes. *Nature* **2000**, *406*, 54–56.

[6] Slater, C.; Cleary, J.; Lau, K. T.; Snakenborg, D.; Corcoran, B.; Kutter, J. P.; Diamond, D. Validation of a fully autonomous phosphate analyser based on a microfluidic lab-on-a-chip. *Water Science & Technology* **2010**, *61*.

[7] Zhang, J. Z.; Chi, J. Automated analysis of nanomolar concentrations of phosphate in natural waters with liquid waveguide. *Environmental Science & Technology* **2002**, *36*, 1048–1053.

[8] Gimbert, L. J.; Haygarth, P. M.; Worsfold, P. J. Determination of nanomolar concentrations of phosphate in natural waters using flow injection with a long path length liquid waveguide capillary cell and solid-state spectrophotometric detection. *Talanta* **2007**, *71*, 1624–1628.

[9] Li, Q. P.; Hansell, D. A. Intercomparison and coupling of magnesium-induced co-precipitation and long-path liquid-waveguide capillary cell techniques for trace analysis of phosphate in seawater. *Analytica Chimica Acta* **2008**, *611*, 68–72.

[10] Patey, M. D.; Rijkenberg, M. J. A.; Statham, P. J.; Stinchcombe, M. C.; Achterberg, E. P.; Mowlem, M. Determination of nitrate and phosphate in seawater at nanomolar concentrations. *TrAC Trends in Analytical Chemistry* **2008**, *27*, 169–182.

[11] Karl, D. M.; Tien, G. MAGIC: A sensitive and precise method for measuring dissolved phosphorus in aquatic environments. *Limnology and Oceanography* **1992**, *37*, 105–116.

[12] Rimmelin, P.; Moutin, T. Re-examination of the MAGIC method to determine low orthophosphate concentration in seawater. *Analytica Chimica Acta* **2005**, *548*, 174–182.

[13] Anagnostou, E.; Sherrell, R. M. A MAGIC method for sub-nanomolar orthophosphate determination in freshwater. *Limnology and Oceanography: Methods* **2008**, *6*, 64–74.

[14] Engblom, S. O. The phosphate sensor. *Biosensors and Bioelectronics* **1998**, *13*, 981–994.

[15] Wollenberger, U.; Schubert, F.; Scheller, F. W. Biosensor for sensitive phosphate detection. *Sensors and Actuators B: Chemical* **1992**, *7*, 412–415.

[16] Breeuwsma, A.; Lyklema, J. Physical and chemical adsorption of ions in the electrical double layer on hematite (α-Fe_2O_3). *Journal of Colloid and Interface Science* **1973**, *43*, 437–448.

[17] Yates, D.; Healy, T. Mechanism of anion adsorption at the ferric and chromic oxide/water interfaces. *Journal of Colloid and Interface Science* **1975**, *52*, 222–228.

[18] Hansmann, D. D.; Anderson, M. A. Using electrophoresis in modeling sulfate, selenite, and phosphate adsorption onto goethite. *Environmental Science & Technology* **1985**, *19*, 544–551.

[19] Parfitt, R. L. Phosphate reactions with natural allophane, ferrihydrite and goethite. *European Journal of Soil Science* **1989**, *40*, 359–369.

[20] Tejedor-Tejedor, M. I.; Anderson, M. A. Protonation of phosphate on the surface of goethite as studied by CIR-FTIR and electrophoretic mobility. *Langmuir* **1990**, *6*, 602–611.

[21] Nilsson, N.; Lövgren, L.; Sjöberg, S. Phosphate complexation at the surface of goethite. *Chemical Speciation and Bioavailability* **1992**, *4*, 121–121.

[22] Arai, Y.; Sparks, D. L. ATR-FTIR spectroscopic investigation on phosphate adsorption mechanisms at the ferrihydrite-water interface. *Journal of Colloid and Interface Science* **2001**, *241*, 317–326.

[23] Appenzeller, B. M. R.; Duval, Y. B.; Thomas, F.; Block, J. C. Influence of phosphate on bacterial adhesion onto iron oxyhydroxide in drinking water. *Environmental Science & Technology* **2002**, *36*, 646–652.

[24] Antelo, J.; Avena, M.; Fiol, S.; López, R.; Arce, F. Effects of pH and ionic strength on the adsorption of phosphate and arsenate at the goethite-water interface. *Journal of Colloid and Interface Science* **2005**, *285*, 476–486.

[25] Daou, T. J.; Begin-Colin, S.; Grenèche, J. M.; Thomas, F.; Derory, A.; Bernhardt, P.; Legaré, P.; Pourroy, G. Phosphate adsorption properties of magnetite-based nanoparticles. *Chemistry of Materials* **2007**, *19*, 4494–4505.

[26] Anderson, M. A.; Malotky, D. T. The adsorption of protolyzable anions on hydrous oxides at the isoelectric pH. *Journal of Colloid and Interface Science* **1979**, *72*, 413–427.

[27] Feiler, A.; Jenkins, P.; Ralston, J. Metal oxide surfaces separated by aqueous solutions of linear polyphosphates: DLVO and non-DLVO interaction forces. *Physical Chemistry Chemical Physics* **2000**, *2*, 5678–5683.

[28] Rigney, M.; Funkenbusch, E.; Carr, P. Physical and chemical characterization of microporous zirconia. *Journal of Chromatography A* **1990**, *499*, 291–304.

[29] Xu, Q.; Anderson, M. A. Synthesis of porosity controlled ceramic membranes. *Journal of Materials Research* **1991**, *6*, 1073–1081.

[30] Anderson, M. A.; Gieselmann, M. J.; Xu, Q. Titania and alumina ceramic membranes. *Journal of Membrane Science* **1988**, *39*, 243–258.

[31] Moss, R. E.; Jackowski, J. J.; de Souza Castilho, M.; Anderson, M. A. Development and evaluation of a nanoporous iron (hydr)oxide electrode for phosphate sensing. *Electroanalysis* **2011**, *23*, 1718–1725.

[32] Xu, Q. Physical-chemical factors affecting the synthesis and characteristics of transition metal oxide membranes, University of Wisconsin-Madison: Madison, WI, 1991.

[33] Stern, K. H. *Metallurgical and Ceramic Protective Coatings*; Springer, 1996.

[34] Innocenzi, P.; Guglielmi, M.; Gobbin, M.; Colombo, P. Coating of metals by the sol-gel dip-coating method. *Journal of the European Ceramic Society* **1992**, *10*, 431–436.

[35] Ayral, A.; Guizard, C. Preparation of Sol-Gel Derived SiO_2 and Al_2O_3 layers with designed nanoporosity. *Materials Transactions-JIM* **2001**, *42*, 1641–1646.

[36] Lee, B.; Hench, L. Electrophoretic behavior and surface reactions of sol-gel derived alumina. *Colloids and Surfaces* **1989**, *23*, 211–229.

[37] Soled, S.; McVicker, G. B. Acidity of silica-substituted zirconia. *Catalysis Today* **1992**, *14*, 189–194.

[38] Zacharaki, I.; Kontoyannis, C.; Lycourghiotis, A.; Kordulis, C. The influence of calcination on the size of nanocrystals, porous structure and acid-base properties of mesoporous anatase used as catalytic support. *Colloids and Surfaces A: Physicochemical and Engineering Aspects* **2008**, *324*, 208–216.

[39] Pourbaix, M. Atlas of electrochemical equilibria in aqueous solutions. *M. Pourbaix, published 1974 by NACE, 644,* **1974**.

[40] Sugimoto, W.; Iwata, H.; Yokoshima, K.; Murakami, Y.; Takasu, Y. Proton and electron conductivity in hydrous ruthenium oxides evaluated by electrochemical impedance spectroscopy: the origin of large capacitance. *The Journal of Physical Chemistry B* **2005**, *109*, 7330–7338.

[41] Nelson, B. P.; Candal, R.; Corn, R. M.; Anderson, M. A. Control of surface and ζ potentials on nanoporous TiO_2 Films by potential-determining and specifically adsorbed ions. *Langmuir* **2000**, *16*, 6094–6101.

[42] Kang, S. A.; Li, W.; Lee, H. E.; Phillips, B. L.; Lee, Y. J. Phosphate uptake by TiO_2: Batch studies and NMR spectroscopic evidence for multisite adsorption. *Journal of Colloid and Interface Science* **2011**.

[43] Kosmulski, M. The significance of the difference in the point of zero charge between rutile and anatase. *Advances in Colloid and Interface Science* **2002**, *99*, 255–264.

[44] Keiser, H.; Beccu, K. D.; Gutjahr, M. A. Abschätzung der porenstruktur poröser elektroden aus impedanzmessungen. *Electrochimica Acta* **1976**, *21*, 539–543.

[45] Song, H.-K.; Sung, J.-H.; Jung, Y.-H.; Lee, K.-H.; Dao, L. H.; Kim, M.-H.; Kim, H.-N. Electrochemical Porosimetry. *Journal of the Electrochemical Society* **2004**, *151*, E102.

[46] Liu, H.; Sun, X.; Yin, C.; Hu, C. Removal of phosphate by mesoporous ZrO_2. *Journal of Hazardous Materials* **2008**, *151*, 616–622.

[47] Cabrera, F.; Madrid, L.; Arambarri, P. Adsorption of phosphate by various oxides: theoretical treatment of the adsorption envelope. *European Journal of Soil Science* **1977**, *28*, 306–313.

[48] Huang, X.; Foster, G. D.; Honeychuck, R. V.; Schreifels, J. A. The maximum of phosphate adsorption at pH 4.0: why it appears on aluminum oxides but not on iron oxides. *Langmuir* **2009**, *25*, 4450–4461.

[49] Huang, C. Adsorption of phosphate at the hydrous γ-Al_2O_3-electrolyte interface. *Journal of Colloid and Interface Science* **1975**, *53*, 178–186.

[50] Caldararu, M.; Postole, G.; Hornoiu, C.; Bratan, V.; Dragan, M.; Ionescu, N. I. Electrical conductivity of γ-Al_2O_3 at atmospheric pressure under dehydrating/hydrating conditions. *Applied Surface Science* **2001**, *181*, 255–264.

[51] Bard, A. J.; Faulkner, L. R. *Electrochemical Methods: Fundamentals and Applications*; 2nd ed.; John Wiley & Sons, 2001.

Tables

Table 4.3 Isoelectric pH values for metal oxide ceramics prepared via sol-gel methods.

Metal oxide	Isoelectric pH	Reference
TiO_2	6.7	Zacharaki et al. (2008)[38]
ZrO_2	7.3	Soled and McVicker (1992)[37]
γ-Al_2O_3	8.5	Lee and Hench (1989)[36]
α-Fe_2O_3	8.1	Own work

Figures

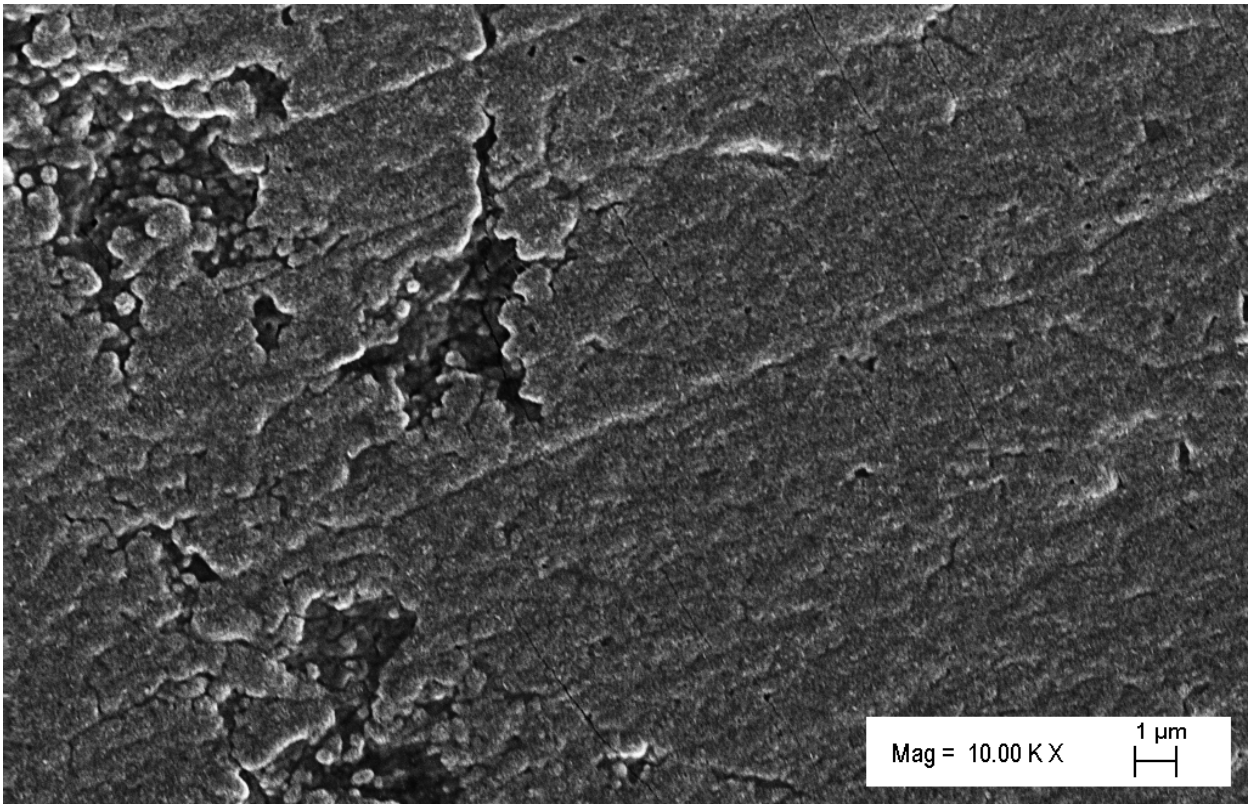

Figure 4.1 Scanning electron micrograph of titania (TiO_2) coated electrode surface with 10,000x magnification.

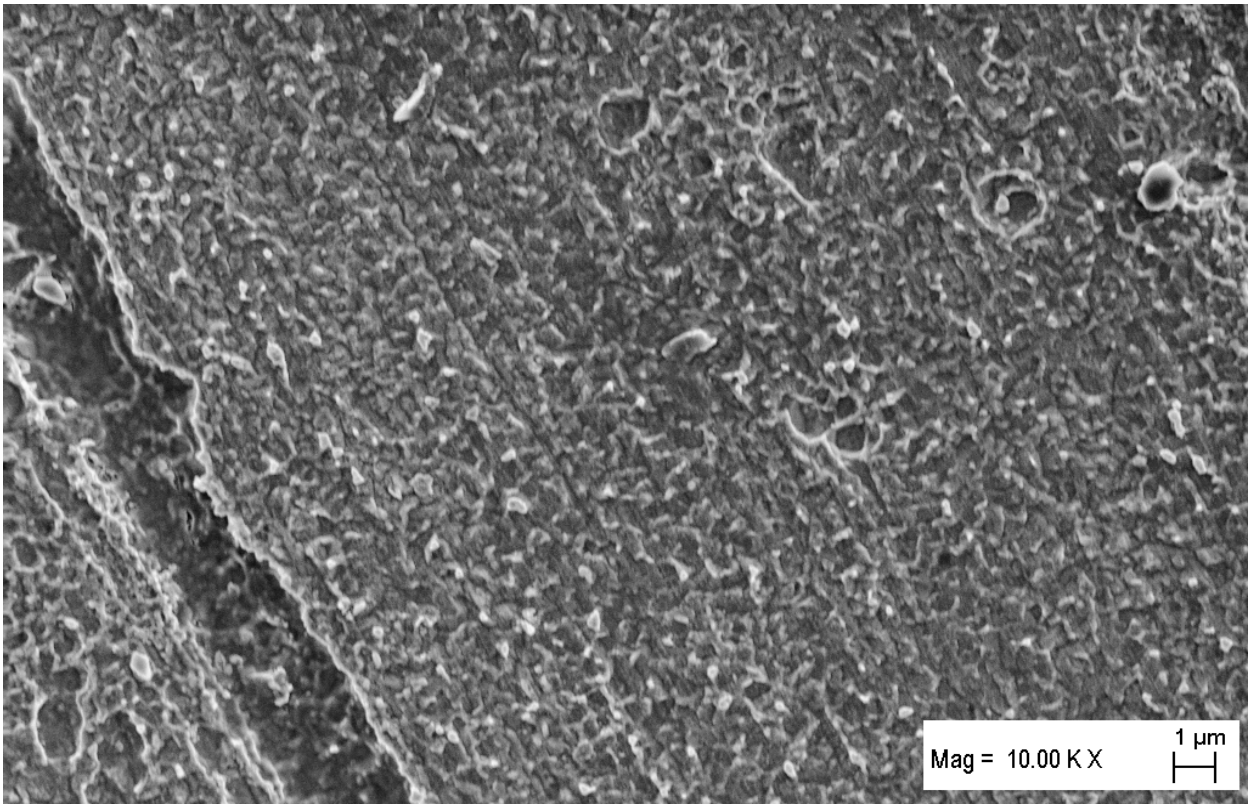

Figure 4.2 Scanning electron micrograph of zirconia (ZrO_2) coated electrode surface with 10,000x magnification.

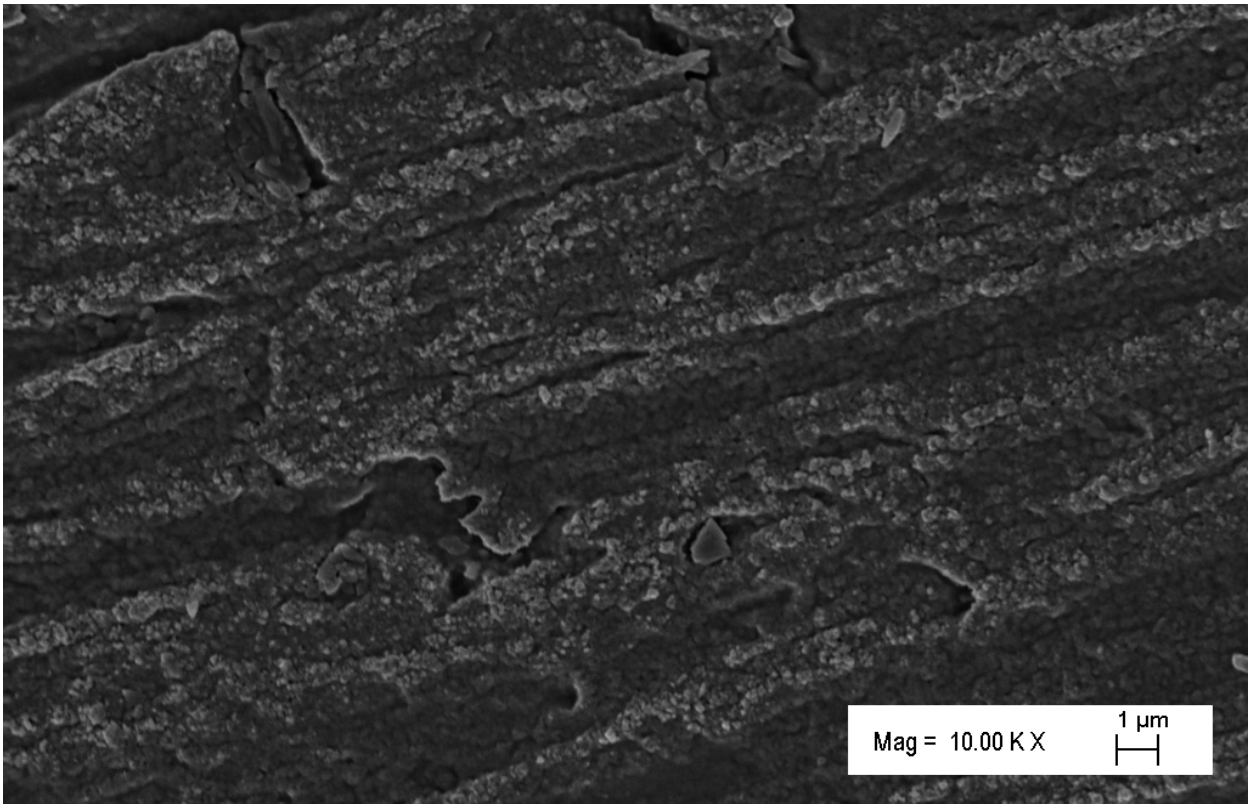

Figure 4.3 Scanning electron micrograph of γ-alumina (γ-Al_2O_3) coated electrode surface with 10,000x magnification.

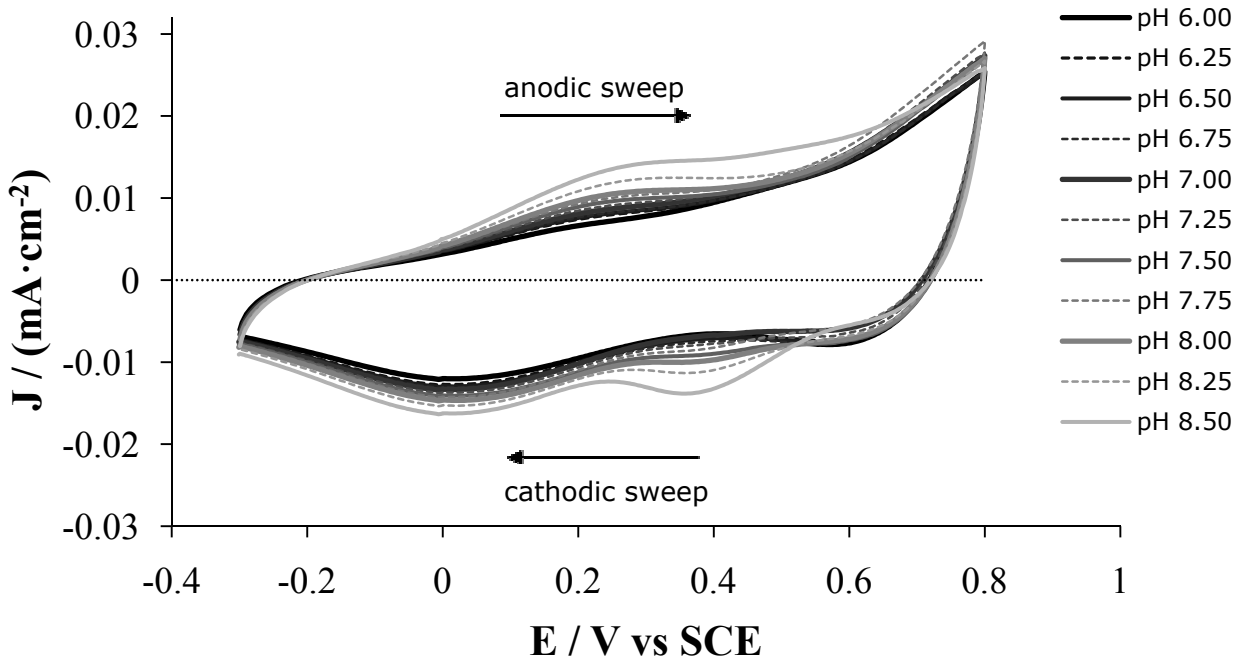

Figure 4.4 Cyclic voltammograms of the titania coated electrode in 5 mM $NaClO_4$ over the pH range 6.00 – 8.50. Arrows denote the anodic and cathodic potential sweep direction.

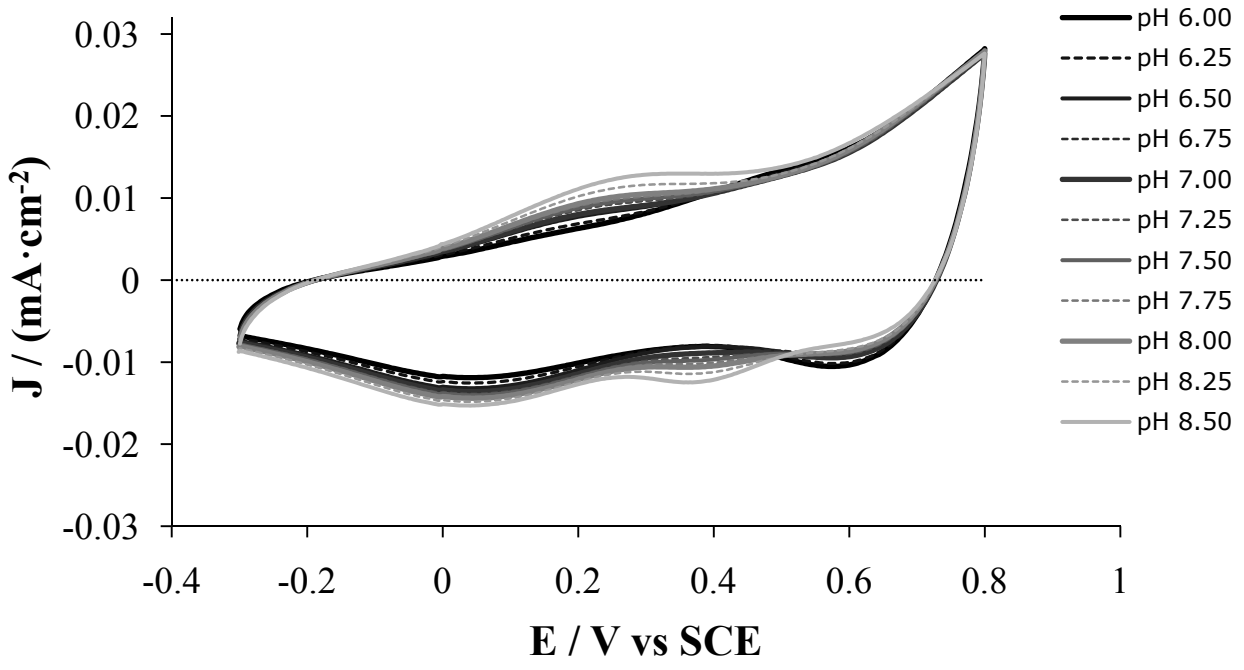

Figure 4.5 Cyclic voltammograms of the titania coated electrode in 10^{-6} M phosphate, 5 mM $NaClO_4$, over the pH range 6.00 – 8.50.

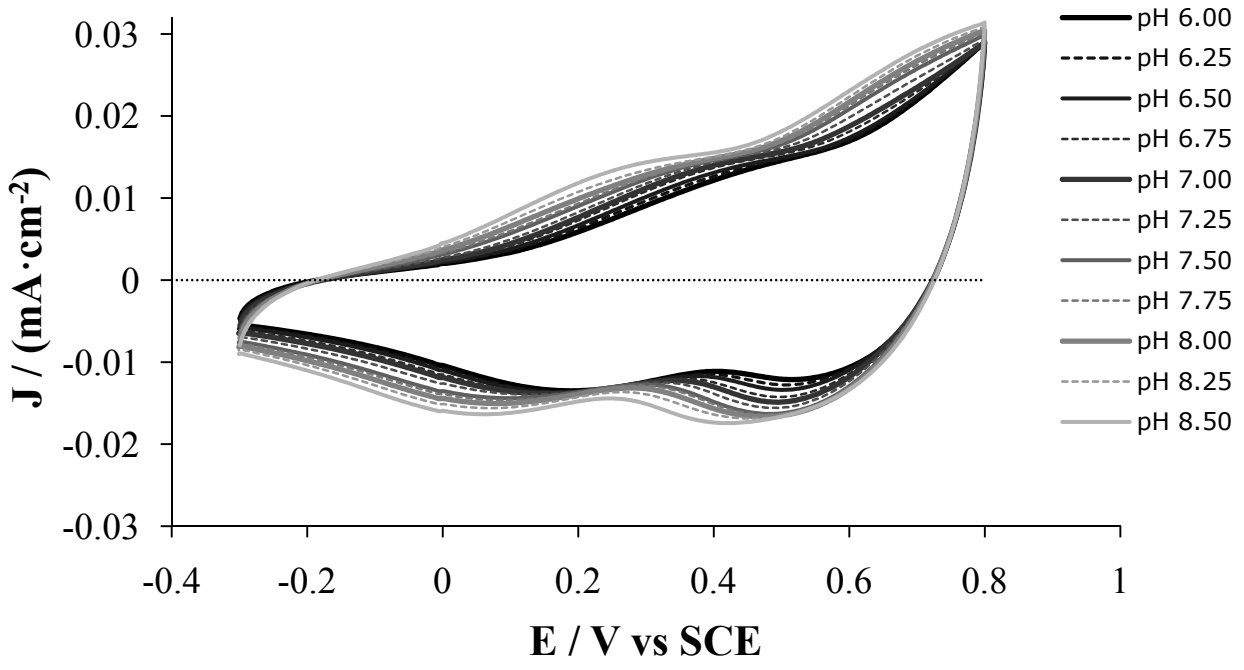

Figure 4.6 Cyclic voltammograms of the titania coated electrode in 10^{-4} M phosphate, 5 mM $NaClO_4$, over the pH range 6.00 – 8.50.

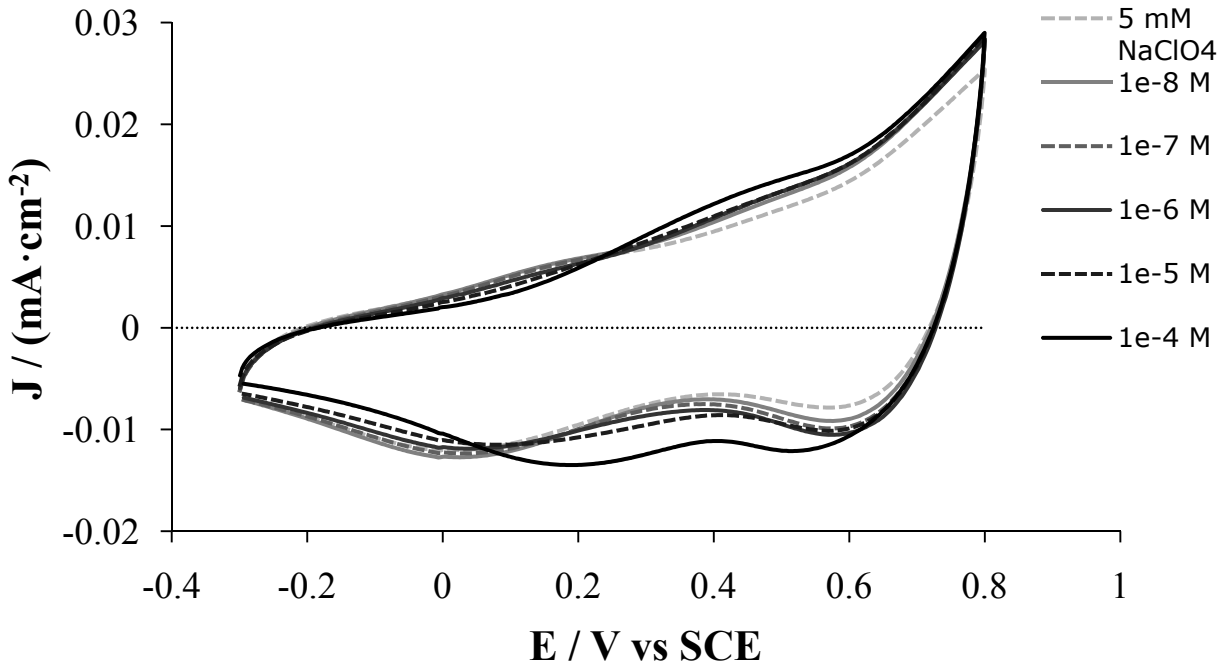

Figure 4.7 Cyclic voltammograms of the titania coated electrode in 5 mM $NaClO_4$ and in 10^{-8} M, 10^{-7} M, 10^{-6} M, 10^{-5} M, and 10^{-4} M phosphate, pH 6.00.

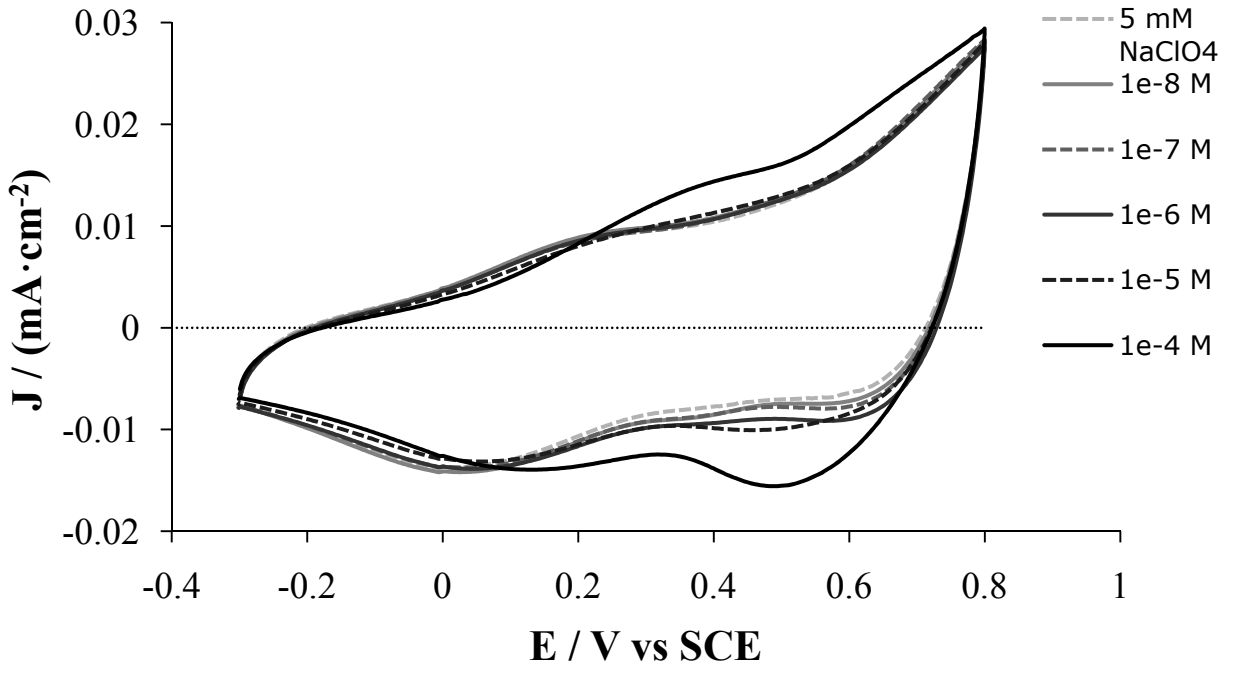

Figure 4.8 Cyclic voltammograms of the titania coated electrode in 5 mM $NaClO_4$ and in 10^{-8} M, 10^{-7} M, 10^{-6} M, 10^{-5} M, and 10^{-4} M phosphate, pH 7.25.

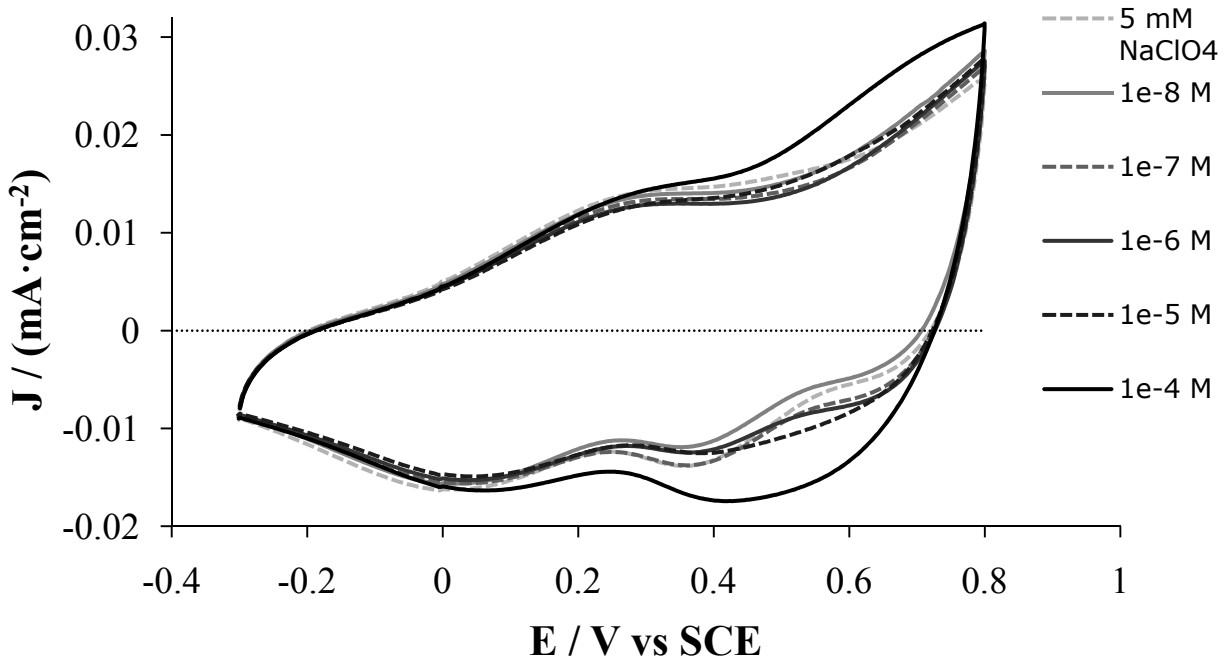

Figure 4.9 Cyclic voltammograms of the titania coated electrode in 5 mM $NaClO_4$ and in 10^{-8} M, 10^{-7} M, 10^{-6} M, 10^{-5} M, and 10^{-4} M phosphate, pH 8.50.

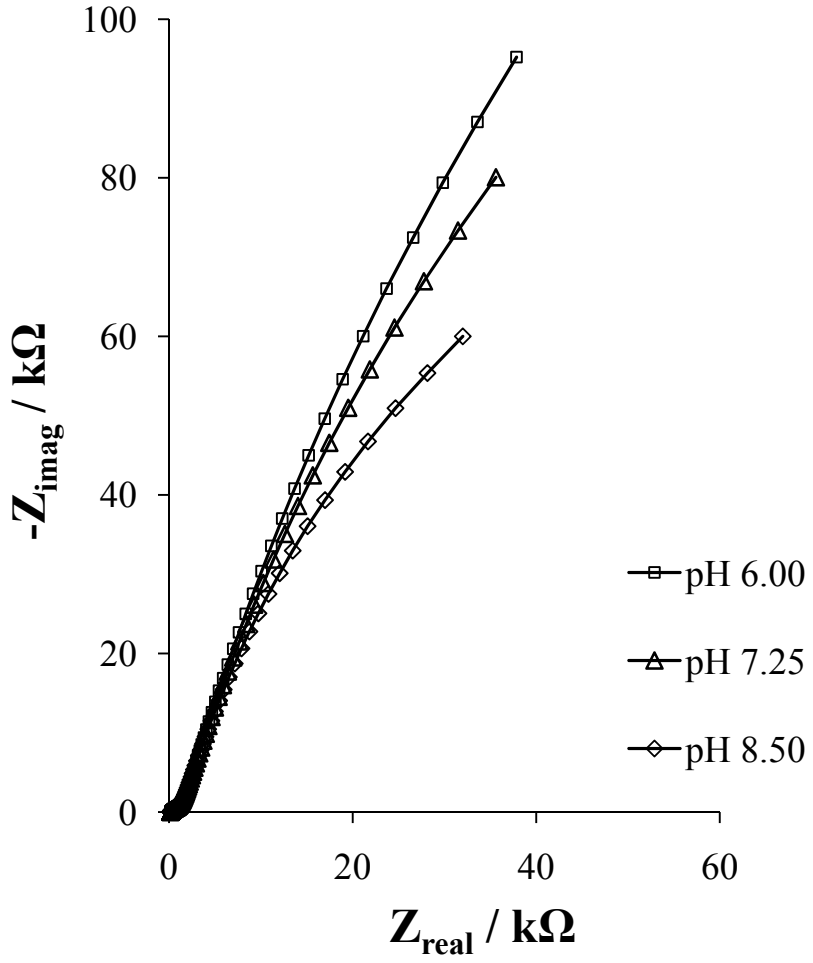

Figure 4.10 Nyquist plot of the titania coated electrode in 5 mM $NaClO_4$ at pH 6.00, 7.25, and 8.50. The electrochemical impedance spectra bias voltage was -0.24 V vs. SCE, with frequency range 50 mHz – 10 kHz.

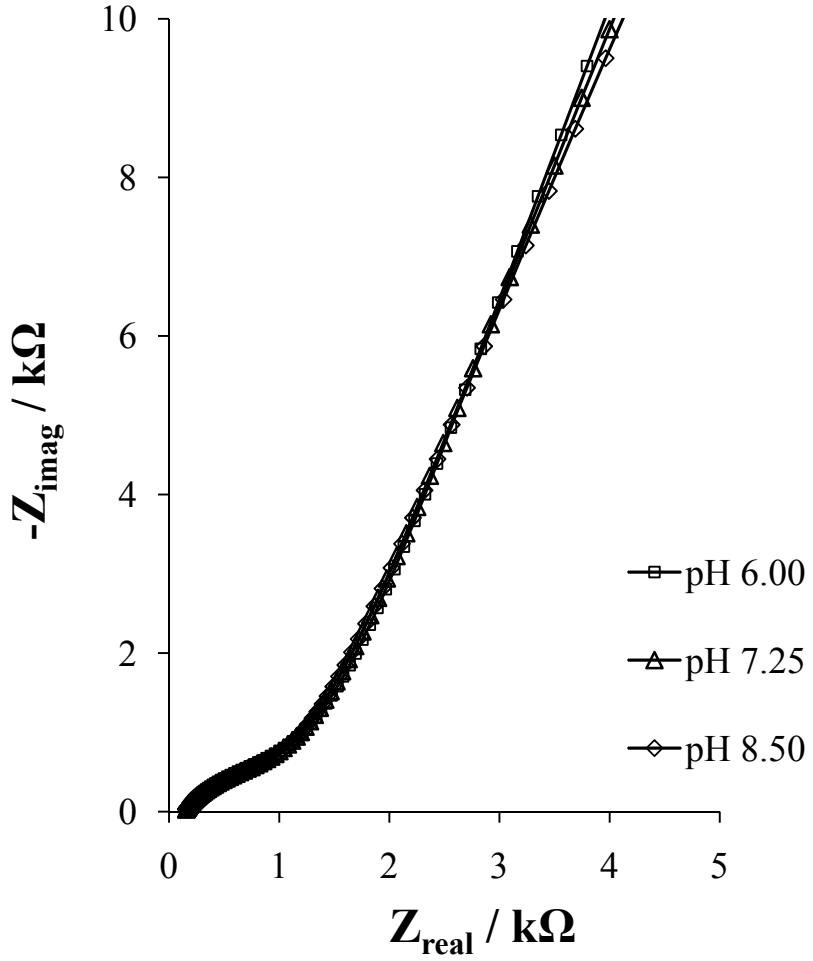

Figure 4.11 High frequency region of Nyquist plot of the titania coated electrode in 5 mM $NaClO_4$ at pH 6.00, 7.25, and 8.50.

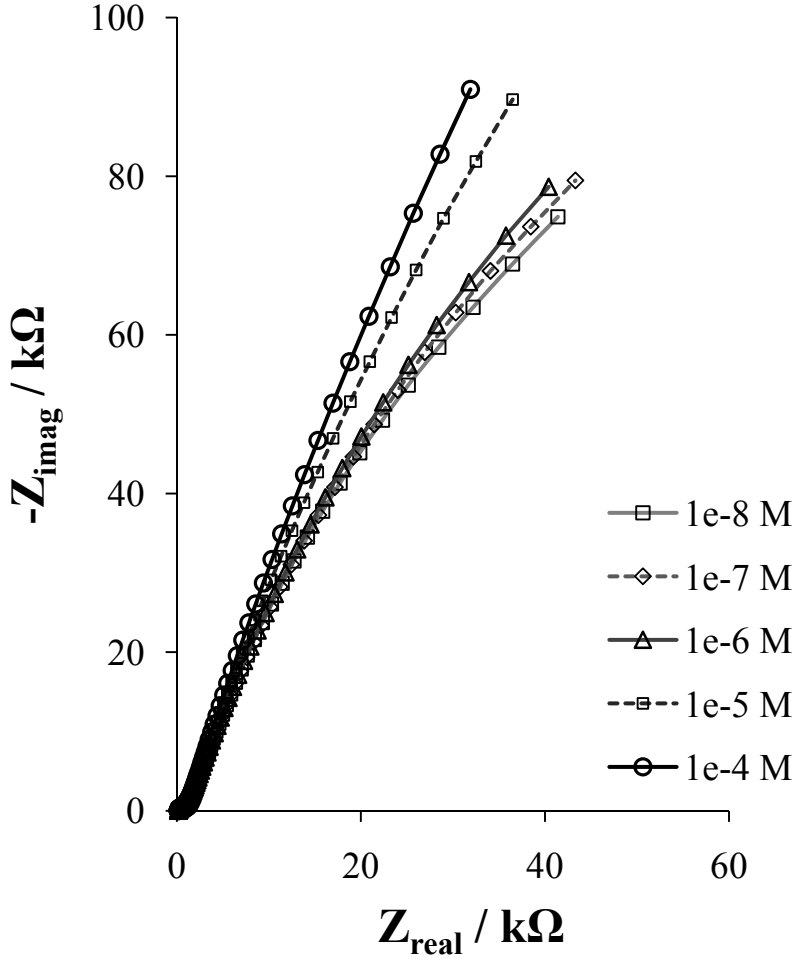

Figure 4.12 Nyquist plot of the titania coated electrode in 5 mM $NaClO_4$ and in 10^{-8} M, 10^{-7} M, 10^{-6} M, 10^{-5} M, and 10^{-4} M phosphate, pH 7.25.

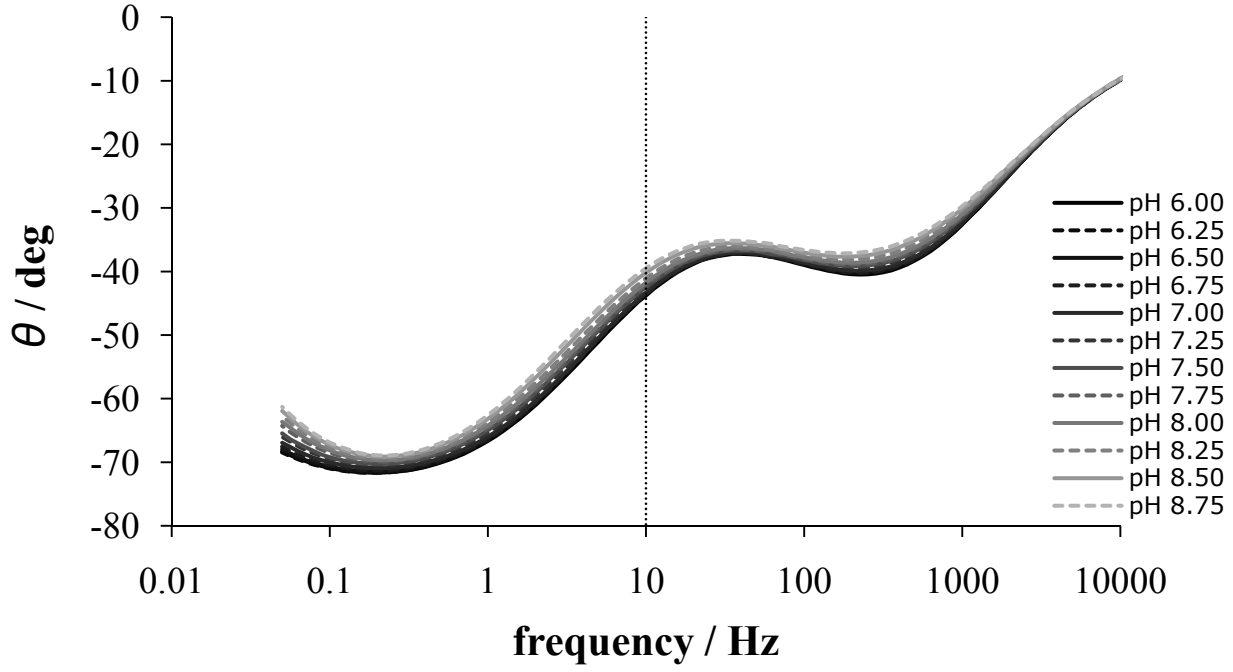

Figure 4.13 Bode phase plot of the titania coated electrode in 5 mM $NaClO_4$ over the pH range 6.00 – 8.75. The dotted line indicates the frequency 10 Hz.

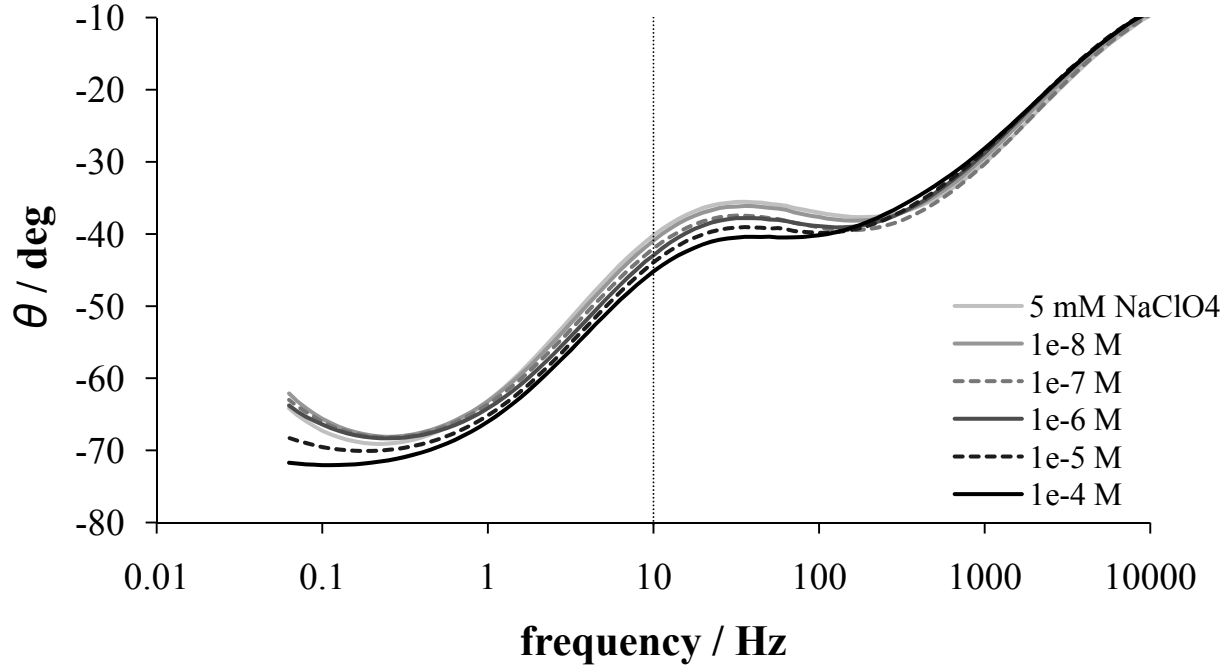

Figure 4.14 Bode phase plot of the titania coated electrode in 5 mM $NaClO_4$ and 10^{-8} M, 10^{-7} M, 10^{-6} M, 10^{-5} M, and 10^{-4} M phosphate, pH 8.50. The dotted line indicates the frequency 10 Hz.

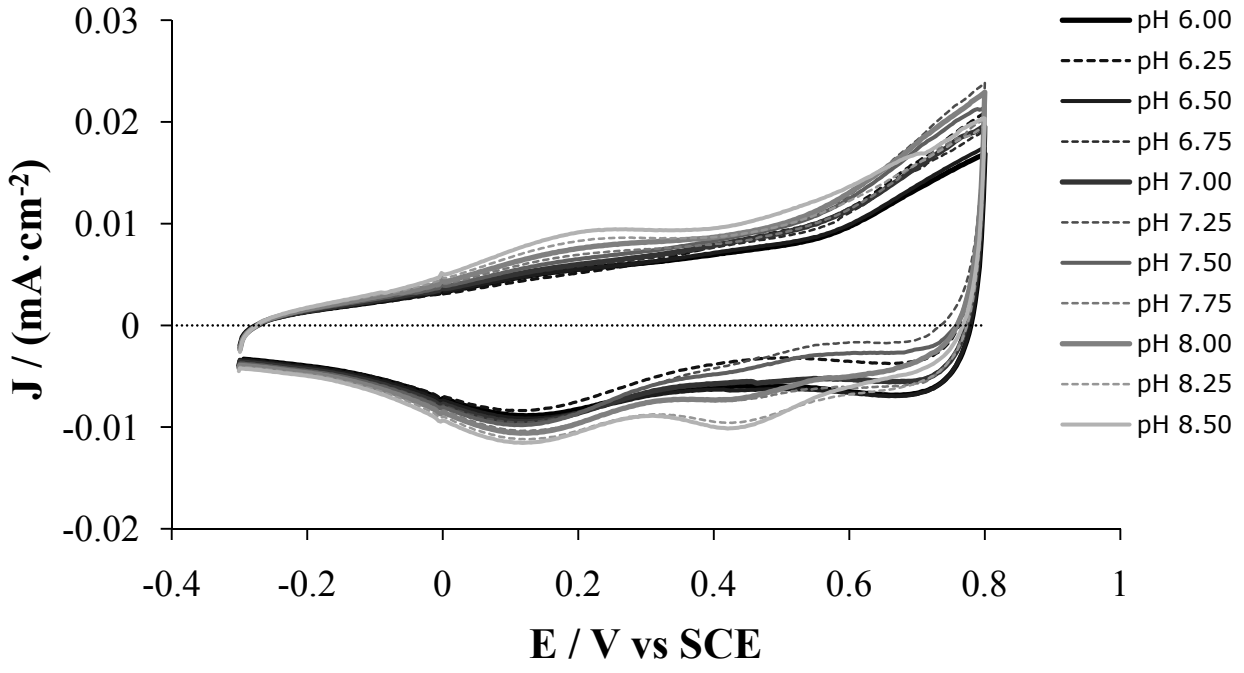

Figure 4.15 Cyclic voltammograms of the zirconia coated electrode in 5 mM $NaClO_4$ over the pH range 6.00 – 8.50.

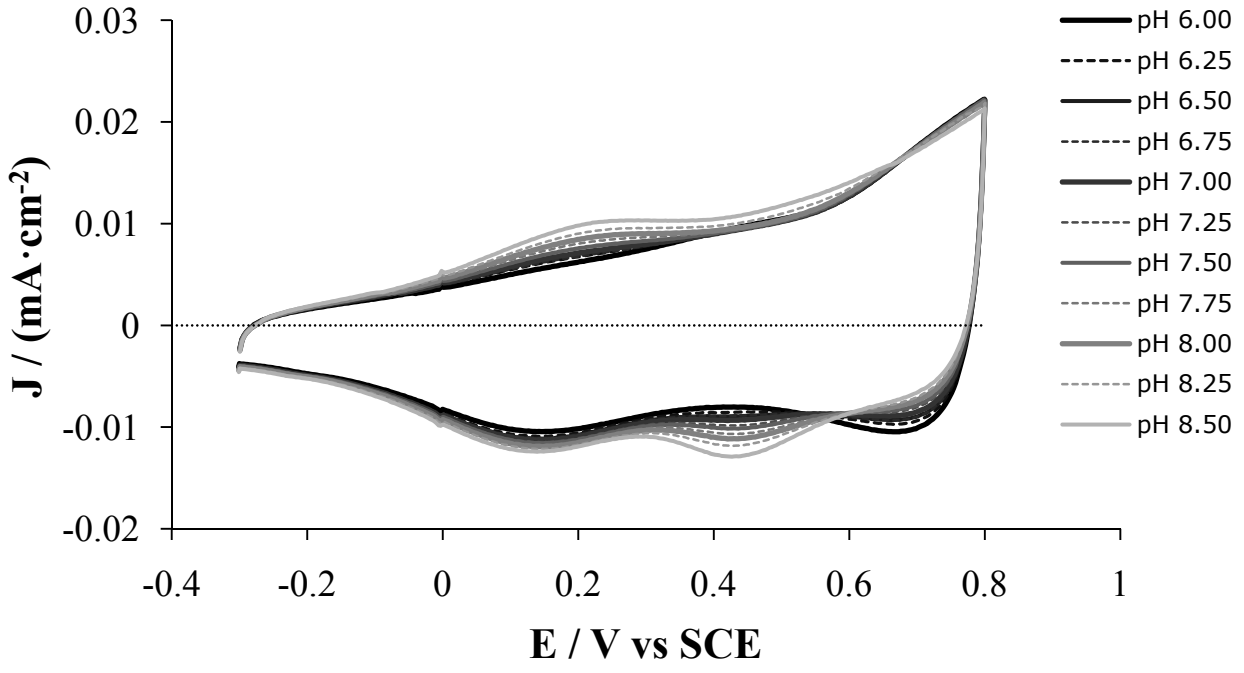

Figure 4.16 Cyclic voltammograms of the zirconia coated electrode in 10^{-6} M phosphate, 5 mM $NaClO_4$, over the pH range 6.00 – 8.50.

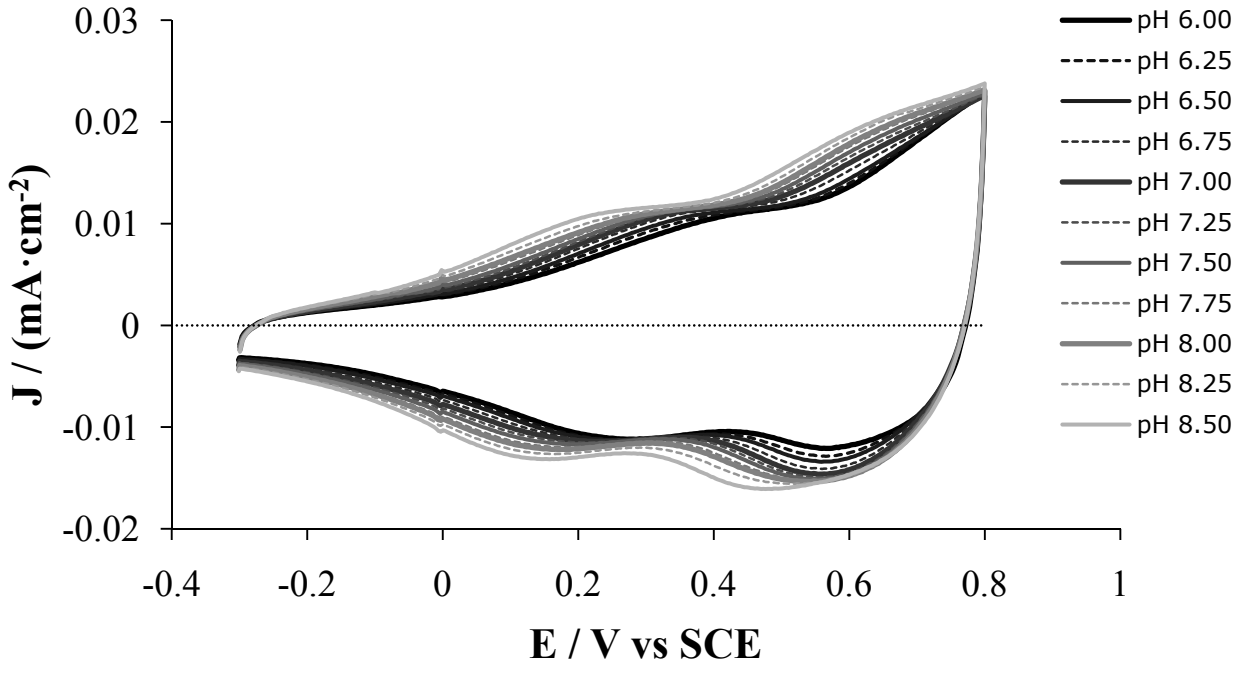

Figure 4.17 Cyclic voltammograms of the zirconia coated electrode in 10^{-4} M phosphate, 5 mM $NaClO_4$, over the pH range 6.00 – 8.50.

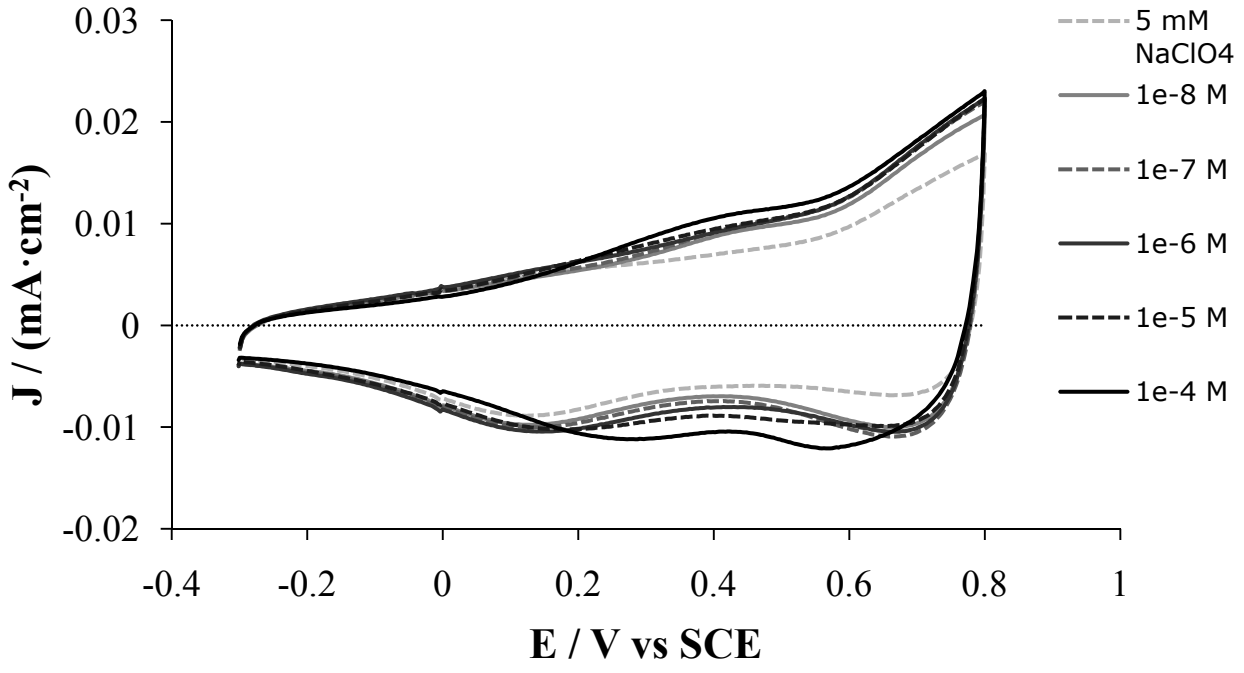

Figure 4.18 Cyclic voltammograms of the zirconia coated electrode in 5 mM $NaClO_4$ and in 10^{-8} M, 10^{-7} M, 10^{-6} M, 10^{-5} M, and 10^{-4} M phosphate, pH 6.00.

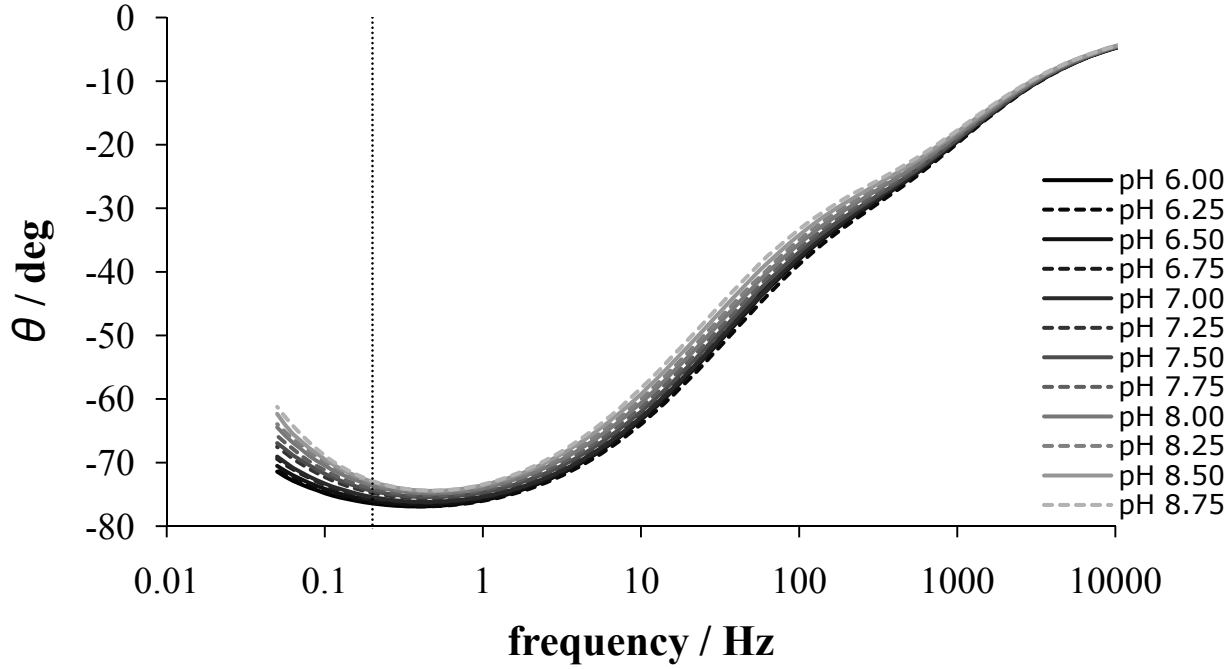

Figure 4.19 Bode phase plot of the zirconia coated electrode in 5 mM $NaClO_4$ over the pH range 6.00 – 8.75. The dotted line indicates the frequency 0.2 Hz.

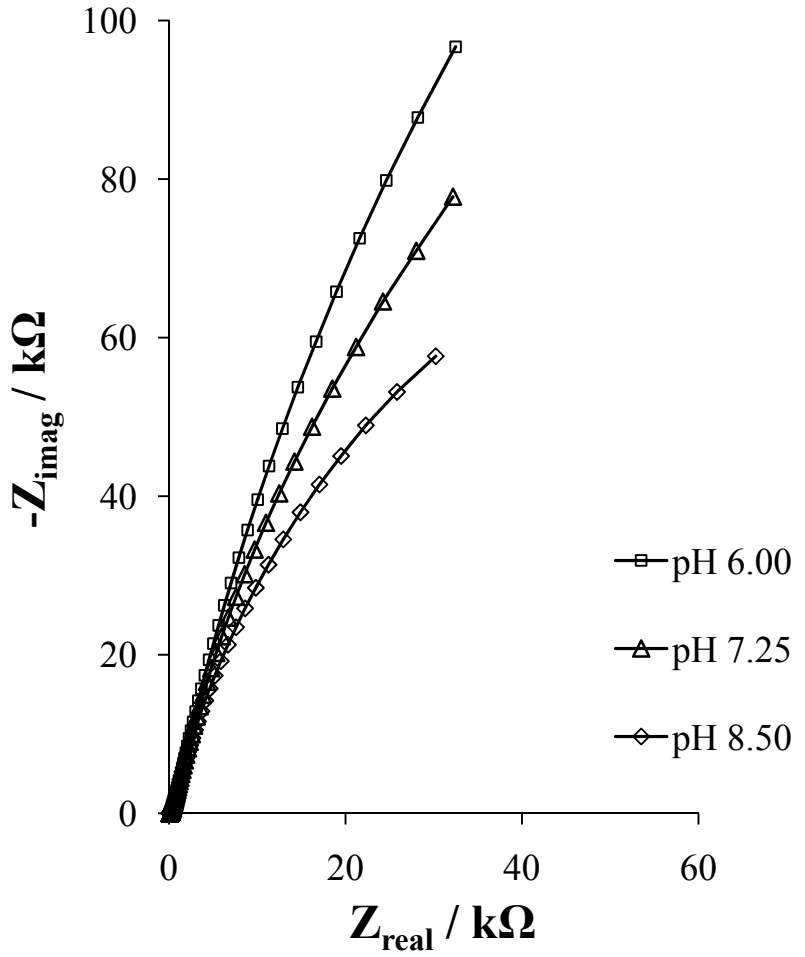

Figure 4.20 Nyquist plot of the zirconia coated electrode in 5 mM $NaClO_4$ at pH 6.00, 7.25, and 8.50.

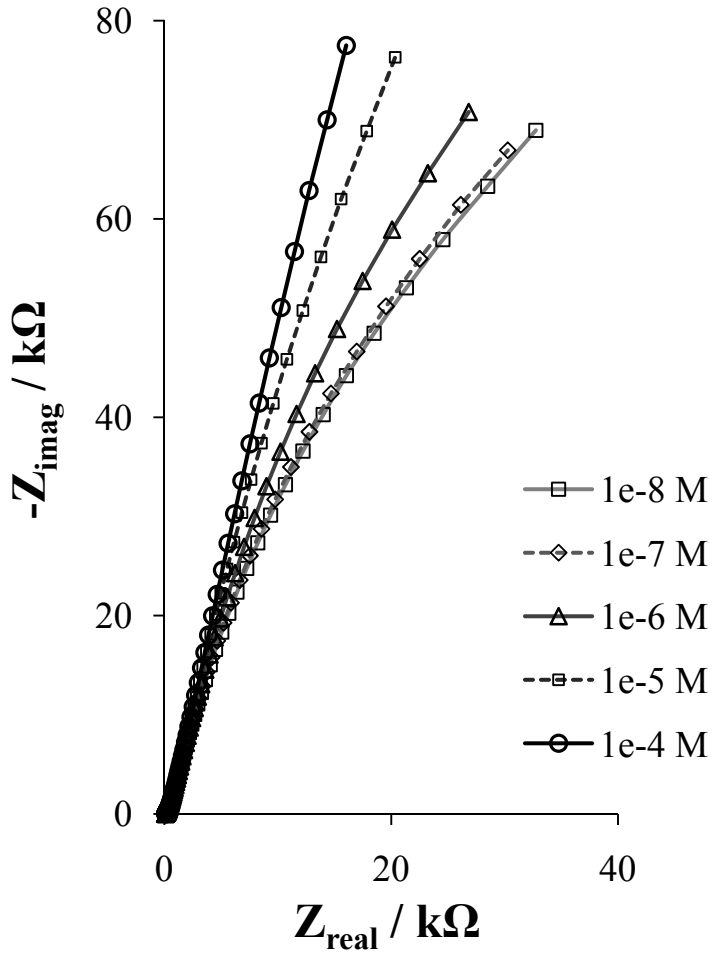

Figure 4.21 Nyquist plot of the zirconia coated electrode in 5 mM $NaClO_4$ and in 10^{-8} M, 10^{-7} M, 10^{-6} M, 10^{-5} M, and 10^{-4} M phosphate, pH 7.25.

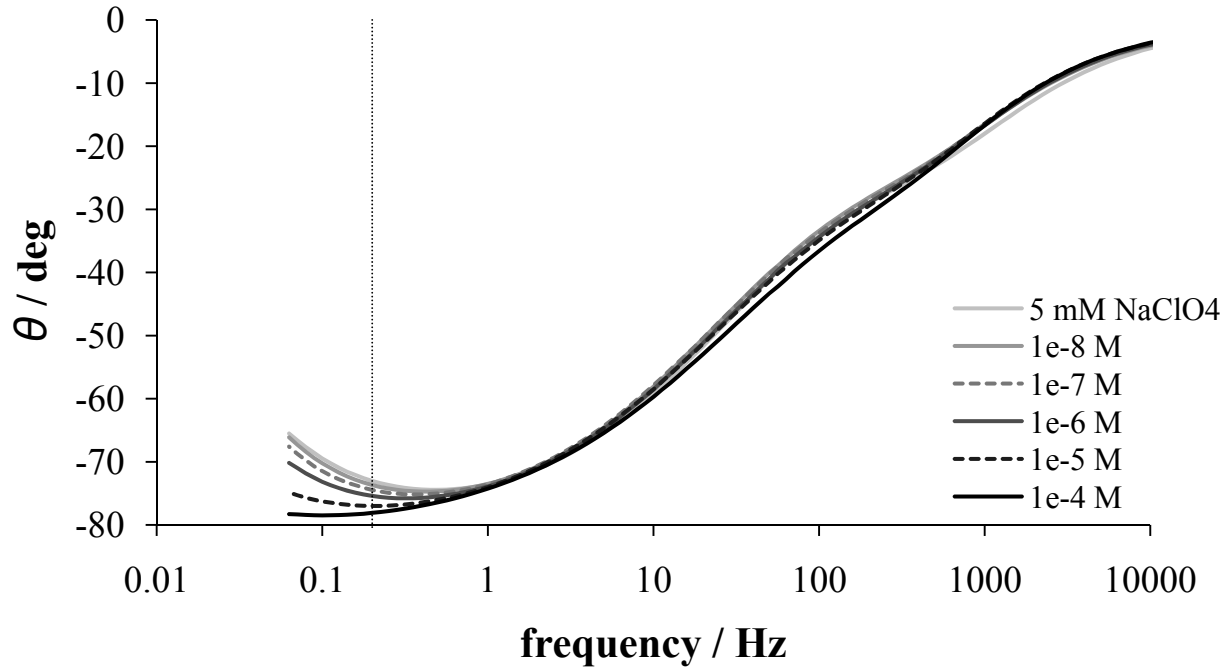

Figure 4.22 Bode phase plot of the zirconia coated electrode in 5 mM $NaClO_4$ and in 10^{-8} M, 10^{-7} M, 10^{-6} M, 10^{-5} M, and 10^{-4} M phosphate, pH 8.50. The dotted line indicates the frequency 0.2 Hz.

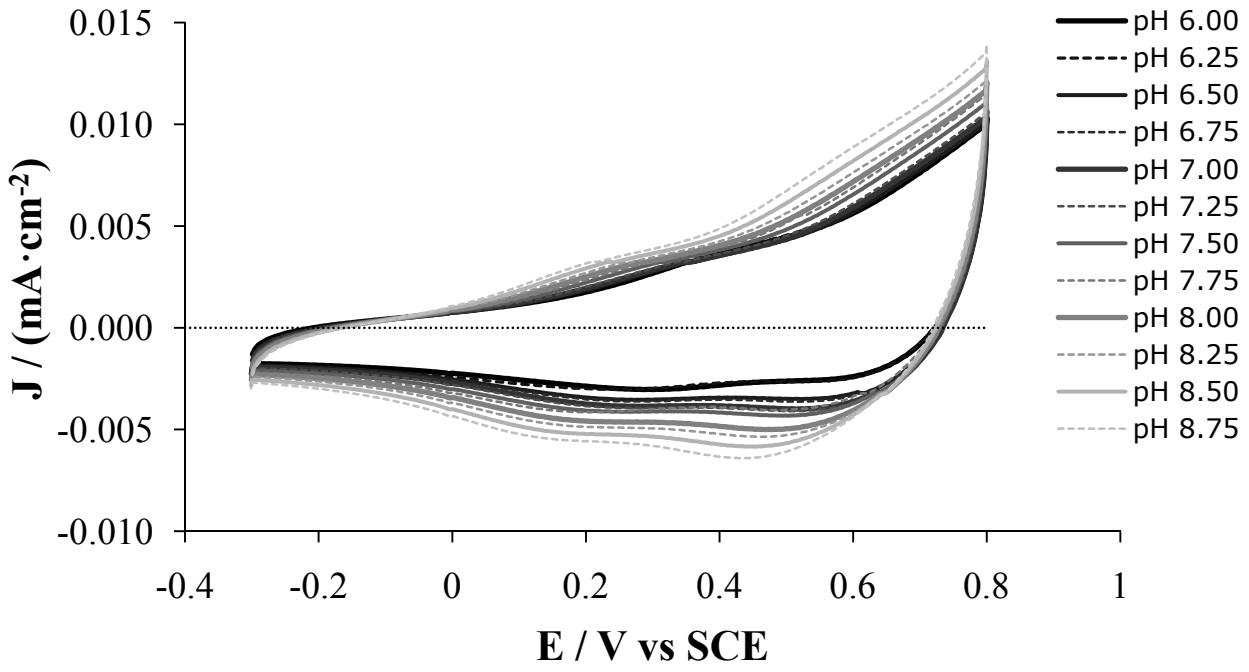

Figure 4.23 Cyclic voltammograms of the alumina coated electrode in 5 mM $NaClO_4$ over the pH range 6.00 – 8.50.

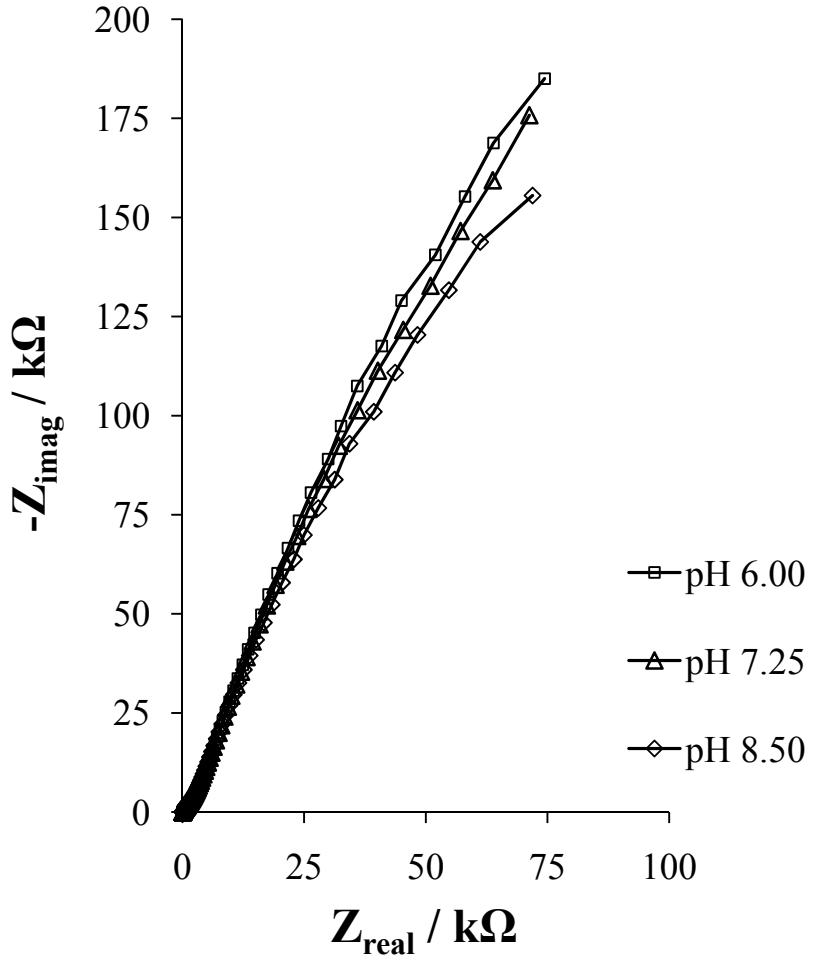

Figure 4.24 Nyquist plot of the alumina coated electrode in 5 mM $NaClO_4$ at pH 6.00, 7.25, and 8.50.

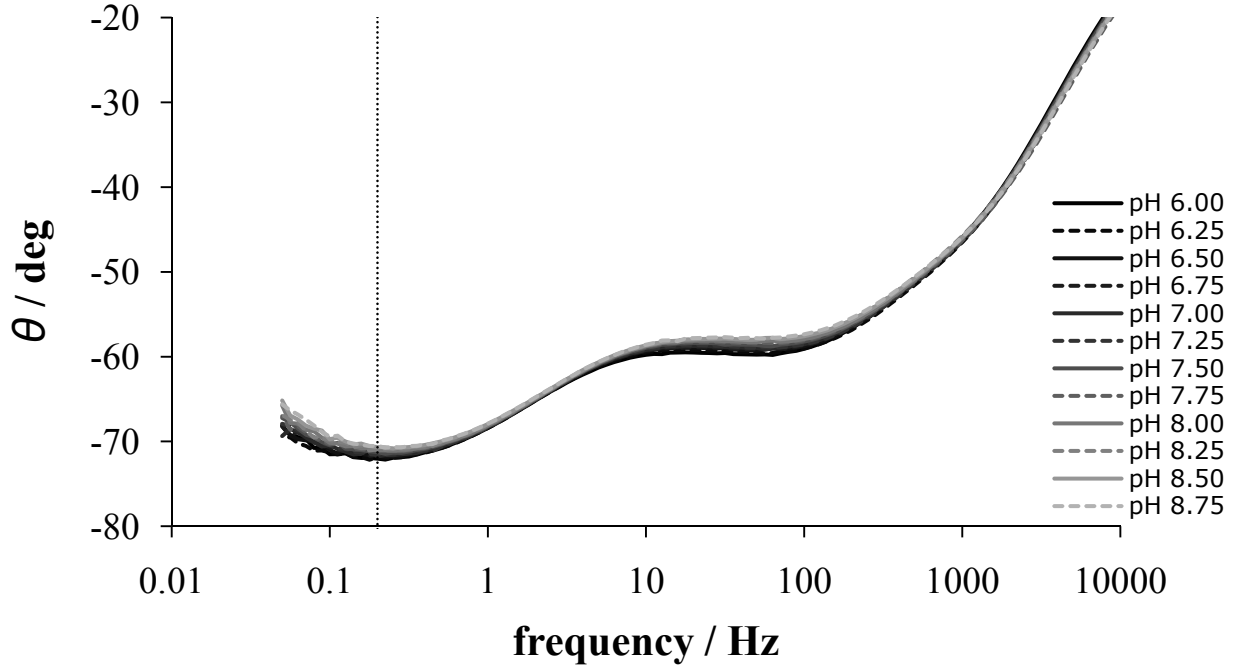

Figure 4.25 Bode phase plot of the alumina coated electrode in 5 mM $NaClO_4$ over the pH range 6.00 – 8.75. The dotted line indicates the frequency 0.2 Hz.

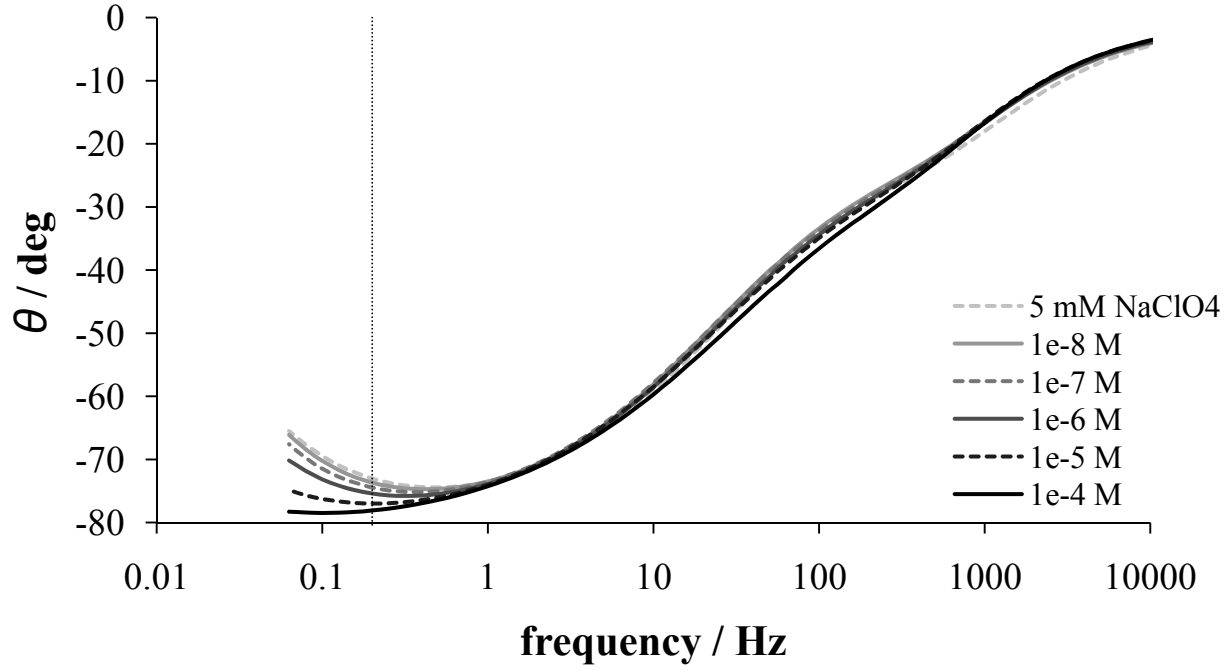

Figure 4.26 Bode phase plot of the alumina coated electrode in 5 mM $NaClO_4$ and in 10^{-8} M, 10^{-7} M, 10^{-6} M, 10^{-5} M, and 10^{-4} M phosphate, pH 8.50. The dotted line indicates the frequency 0.2 Hz.

CHAPTER 5

CONCLUDING REMARKS AND RECOMMENDATIONS

5.1. Concluding Remarks

Phosphorus pollution of aquatic bodies is an environmental problem that is not expected to go away any time soon. Lake Mendota, bordering the campus of the University of Wisconsin-Madison, is expected to remain eutrophic for hundreds of years, even if external input from agricultural sources is reduced [1]. Once a body of water is supplied with excess phosphorus, natural recycling from enriched sediments makes reversal of eutrophic conditions difficult. A sensor for *in situ* measurement of phosphate, the most easily metabolized form of phosphorus, would be a useful tool for monitoring areas that have, or are at risk of having, an overabundance of this important nutrient.

Many researchers have studied phosphate interaction with metal oxides to understand the interfacial chemistry of the adsorption process. This dissertation work is a real-world application that builds upon those efforts. If not for other researchers' findings that phosphate adsorption to metal oxides produces changes in surface electrochemistry, there would not have been reason to believe that the electrochemical perturbation produced by phosphate could be used as a method to quantify the ion. Therefore, this dissertation research is indebted to the efforts of other scientists who investigated specific adsorption of ions on metal oxide surfaces.

Electrodes coated with porous metal (hydr)oxides are easily produced via sol-gel methods. Metal oxide minerals have been long known to interact with phosphate in a way that perturbed electrochemistry, although few studies had set to determine phosphate effects on

coated electrodes with applied voltage. At neutral pH, the hematite (α-Fe_2O_3) iron oxide coated electrode was able to resolve submicromolar phosphate levels using electrochemical impedance spectroscopy, even when other ions common to lakes were present in concentrations several orders of magnitude greater than phosphate (Chapter 2). Upon further investigation, the hematite electrode could produce a standard curve of phosphate concentration over a range of circumneutral pH values (Chapter 3). Adsorption over a phosphate range 10 nM to 0.1 mM and pH range 6.00 – 8.75 was further analyzed by fitting electrochemical impedance data to an equivalent circuit. The model consisted of a solution resistance element and three sub-circuits in series indicating the behavior of phosphate adsorption onto hematite at high, medium, and low frequencies of applied sinusoidal voltage. Analysis of the resistive, capacitive, and constant phase elements in the equivalent circuit provided information that may be useful for sensor applications.

Electrochemical response of a metal oxide to phosphate was not limited to hematite. Titania (TiO_2), zirconia (ZrO_2), and alumina (γ-Al_2O_3) coated electrodes also showed sensitive response to the analyte (Chapter 4). Effects of pH and 10 nM – 0.1 mM phosphate were evaluated for trends in cyclic voltammograms and in graphical representations of electrochemical impedance data. Titania and zirconia had similar response, although the titania coating was more sensitive to submicromolar phosphate over a larger pH range. Furthermore, the titania electrode had a greater reversibility of phosphate detection than either zirconia or hematite. Although phosphate also specifically adsorbs with high surface coverage on aluminum (hydr)oxides [2, 3], the alumina electrode produced current response that differed from the other metal oxides, indicating complex processes of adsorption that may have dependence on the electrical properties of the material. Reviewing sensitivity, selectivity, and reversibility criteria,

nanoporous titania and hematite seemed like the best candidates for further development toward an electrochemical phosphate sensor.

5.2. Recommendations for Future Study

These metal oxide electrodes showed high sensitivity to phosphate, and the hematite electrode has very good selectivity of phosphate over other ions. However, reproducibility of signal between electrodes and minimal hysteresis are also important for a commercial sensor. It is also important to know if polyphosphates and organophosphates will produce a response with these electrodes that may be separated from the orthophosphates detected in these studies. Additionally, a method of applying a porous metal oxide electrode series for quantifying ions other than phosphate would be a great step forward for electrochemical sensing.

Lab-produced materials showed some differences from electrode to electrode. There are several steps in the electrode production process where differences occur. As the sol drying is not instantaneous, gravity and surface tension processes cause the sol to collect more on some sections of an electrode than on others during the dip-coating process, leading to a non-uniform xerogel coat even on a single electrode. In particular, the lengthwise edges of the rectangular foil electrode are an area of film thickness heterogeneity. This may be corrected by the use of a conductive wire substrate that does not have lengthwise edges, as long as the total surface area is great enough that perturbation of the electrical double layer can still be measured. Furthermore, after the electrode has been produced, the distance and angle between electrodes in the electrochemical cell may cause differences in experimental results from the ohmic drop due to solution resistance. A wire electrode may also allow easier construction of a standardized electrochemical cell.

Once a sensor has been calibrated over a range of analyte concentration, it is important that the instrument will give measurements that are not affected by its previous use. Memory issues in a sensor can cause measurements of low concentration to be inaccurate after a high concentration reading. In a system with no potential cycling, phosphate desorption from metal (hydr)oxides does not easily occur without high concentration of NaOH [4-6] that can degrade the material. This work has found evidence that potential cycling can desorb 10^{-6} or 10^{-7} M phosphate at some pH, reducing signal from titania to a great (>99%) extent and from hematite and zirconia to a good (>90%) extent. However, the act of calibration itself should preferably contribute no detectable memory effects. Further study should investigate what could be done to mitigate apparent hysteresis from using the sensor in concentrated phosphate solution. It is also possible that the proposed coated wire electrode, produced by standardized fabrication procedures, could make calibration less essential to the sensing process if the length of the wire has uniform coating.

Soluble phosphorus occurs in a natural environment in forms other than orthophosphates. Other phosphate molecules are polyphosphates, made up of chains of the phosphate monomer, and organophosphates, where a phosphate group is covalently bound to an organic molecule. Polyphosphates can compete with orthophosphate and may also change surface charge properties of metal oxides [7, 8]. More experimental work is needed to determine whether these electrode sensors are selective for orthophosphates over these other molecules. Polyphosphates and organophosphates are bulkier molecules than orthophosphates, and so they might not as easily enter nanopores. These considerations are necessary for the optimization of an electrode capable of excluding other forms of phosphate.

Other oxyanions, such as arsenate and vanadate, are similar to phosphate but specifically adsorb to metal oxides with slightly different affinity [9]. Although the hematite electrode was not able to distinguish phosphate from arsenate (Chapter 2), it is possible that such determination could be made by a series of electrodes. Preliminary multivariate statistical analysis showed evidence that electrochemical impedance can be decomposed to separate the effects of pH from phosphate concentration. It is possible that a multiple electrode system could be fine-tuned to separate electrochemical effects produced by ions that compete with phosphate. This may be useful for developing a sensor with a low detection limit for a specific analyte in an environment or application where it is necessary to exclude phosphate from the measurement. Thus, the results of this work may be useful for the production of either a phosphate sensor or a sensor that eliminates phosphate interference when the phosphate ion is more ubiquitous than the analyte of interest. The development of an electrode system with multiple applications would be an important step forward for *in situ* measurement of ions that impact aquatic systems. Further study making these improvements for standardization and fine-tuning of the phosphate sensor may lead to a robust product that could aid scientists in environmental monitoring, protection, and remediation for years to come.

References

[1] Carpenter, S. R. Eutrophication of aquatic ecosystems: bistability and soil phosphorus. *Proceedings of the National Academy of Sciences of the United States of America* **2005**, *102*, 10002.

[2] Huang, C. Adsorption of phosphate at the hydrous γ-Al_2O_3-electrolyte interface. *Journal of Colloid and Interface Science* **1975**, *53*, 178–186.

[3] Huang, X.; Foster, G. D.; Honeychuck, R. V.; Schreifels, J. A. The maximum of phosphate adsorption at pH 4.0: why it appears on aluminum oxides but not on iron oxides. *Langmuir* **2009**, *25*, 4450–4461.

[4] Schafer, W. A.; Carr, P. W.; Funkenbusch, E. F.; Parson, K. A. Physical and chemical characterization of a porous phosphate-modified zirconia substrate. *Journal of Chromatography A* **1991**, *587*, 137–147.

[5] Strauss, R.; Brümmer, G.; Barrow, N. Effects of crystallinity of goethite: II. Rates of sorption and desorption of phosphate. *European Journal of Soil Science* **1997**, *48*, 101–114.

[6] Liu, H.; Sun, X.; Yin, C.; Hu, C. Removal of phosphate by mesoporous ZrO_2. *Journal of Hazardous Materials* **2008**, *151*, 616–622.

[7] Michelmore, A.; Gong, W.; Jenkins, P.; Ralston, J. The interaction of linear polyphosphates with titanium dioxide surfaces. *Physical Chemistry Chemical Physics* **2000**, *2*, 2985–2992.

[8] Guan, X.-H.; Chen, G.-H.; Shang, C. Competitive adsorption between orthophosphate and other phosphates on aluminum hydroxide. *Soil Science* **2005**, *170*, 340–349.

[9] Stumm, W. The inner sphere surface complex. *Aquatic Chemistry. American Chemical Society, Washington, DC* **1995**, 1–32.

APPENDIX A

OUTPUT OF THE EQUIVALENT CIRCUIT MODEL FOR THE HEMATITE ELECTRODE IN PHOSPHATE

Tables

Table A.1 Parameters of best fit to model circuit $R_S + Q_1/(R_2+Q_2)/(R_3+C_4/R_4)$ for electrochemical impedance spectra of the hematite electrode in 5 mM $NaClO_4$, pH 6.00 – 8.75.

C_{PO4} (M)	pH	R_S (Ω)	Q_1 ($\mu F \cdot s^{\alpha-1}$)	α_1	R_2 (Ω)	Q_2 ($\mu F \cdot s^{\alpha-1}$)	α_2	R_3 (kΩ)	C_4 (μF)	R_4 (kΩ)	χ^2
0	6.00	93.4	56.5	0.7	861	91.1	0.7	4.66	143	19.8	2.37E-02
0	6.25	92.4	56.5	0.7	848	89.8	0.7	4.63	140	20.6	2.22E-02
0	6.50	91.5	56.7	0.7	856	85.6	0.7	4.86	137	22.2	1.96E-02
0	6.75	91.7	57.1	0.7	883	77.9	0.7	5.59	134	24.7	1.36E-02
0	7.00	91.0	56.9	0.7	868	79.8	0.7	5.30	134	24.5	1.45E-02
0	7.25	90.0	57.3	0.7	900	71.3	0.7	6.04	133	27.9	1.03E-02
0	7.50	88.7	57.3	0.7	894	72.5	0.7	5.82	134	27.8	9.98E-03
0	7.75	88.5	57.7	0.7	918	67.2	0.7	6.53	134	30.4	7.94E-03
0	8.00	88.7	57.8	0.7	928	62.8	0.7	7.28	133	33.4	6.78E-03
0	8.25	87.9	58.2	0.7	931	58.2	0.7	8.28	131	37.5	5.64E-03
0	8.50	87.0	58.4	0.7	923	54.1	0.7	9.66	129	42.7	5.48E-03
0	8.75	86.9	58.8	0.7	900	50.1	0.7	11.7	127	50.8	5.41E-03

Table A.2 Parameters of best fit to model circuit $R_S + Q_1/(R_2+Q_2)/(R_3+C_4/R_4)$ for electrochemical impedance spectra of the hematite electrode in 10^{-8} M phosphate, 5 mM $NaClO_4$, pH 6.00 – 8.75.

C_{PO4} (M)	pH	R_S (Ω)	Q_1 ($\mu F \cdot s^{\alpha-1}$)	α_1	R_2 (Ω)	Q_2 ($\mu F \cdot s^{\alpha-1}$)	α_2	R_3 (kΩ)	C_4 (μF)	R_4 (kΩ)	χ^2
1E-08	6.00	102	54.7	0.7	871	85.6	0.7	5.36	127	23.9	1.69E-02
1E-08	6.25	101	55.0	0.7	870	81.3	0.7	5.71	125	25.5	1.40E-02
1E-08	6.50	100	55.4	0.7	888	74.7	0.7	6.32	124	28.4	1.11E-02
1E-08	6.75	99.3	55.4	0.7	883	72.2	0.7	6.49	124	29.4	1.02E-02
1E-08	7.00	98.6	55.5	0.7	860	75.3	0.7	6.04	123	28.4	1.12E-02
1E-08	7.25	97.4	55.7	0.7	865	73.4	0.7	6.27	125	29.6	9.04E-03
1E-08	7.50	97.0	56.1	0.7	876	67.4	0.7	6.87	124	32.9	8.00E-03
1E-08	7.75	96.2	56.1	0.7	868	67.9	0.7	6.79	124	32.9	7.54E-03
1E-08	8.00	95.7	56.4	0.7	880	62.5	0.7	7.78	124	37.4	5.74E-03
1E-08	8.25	95.0	56.9	0.7	882	59.3	0.7	8.68	123	41.2	5.53E-03
1E-08	8.50	94.4	57.3	0.7	877	56.0	0.7	9.92	122	46.5	5.34E-03
1E-08	8.75	93.7	57.7	0.7	858	51.9	0.7	12.6	120	58.4	5.77E-03

Table A.3 Parameters of best fit to model circuit $R_S + Q_1/(R_2+Q_2)/(R_3+C_4/R_4)$ for electrochemical impedance spectra of the hematite electrode in 10^{-7} M phosphate, 5 mM $NaClO_4$, pH 6.00 – 8.75.

C_{PO4} (M)	pH	R_S (Ω)	Q_1 ($\mu F \cdot s^{\alpha-1}$)	α_1	R_2 (Ω)	Q_2 ($\mu F \cdot s^{\alpha-1}$)	α_2	R_3 (kΩ)	C_4 (μF)	R_4 (kΩ)	χ^2
1E-07	6.00	96.9	55.6	0.7	792	91.7	0.7	4.82	120	24.0	1.29E-02
1E-07	6.25	96.6	55.6	0.7	809	86.1	0.7	5.22	118	27.0	1.22E-02
1E-07	6.50	95.8	55.7	0.7	818	81.3	0.7	5.51	119	28.9	9.86E-03
1E-07	6.75	95.8	56.0	0.7	846	75.8	0.7	5.99	118	31.7	9.22E-03
1E-07	7.00	95.4	55.8	0.7	826	79.4	0.7	5.47	117	29.8	1.04E-02
1E-07	7.25	95.0	55.9	0.7	834	77.2	0.7	5.79	117	31.1	8.57E-03
1E-07	7.50	94.3	55.9	0.7	852	75.2	0.7	5.96	117	32.6	8.98E-03
1E-07	7.75	94.1	56.1	0.7	858	70.3	0.7	6.46	116	35.6	7.53E-03
1E-07	8.00	93.5	56.4	0.7	872	66.7	0.7	7.04	117	38.2	6.15E-03
1E-07	8.25	93.4	56.7	0.7	887	62.8	0.7	7.96	118	41.8	5.52E-03
1E-07	8.50	92.7	56.9	0.7	880	57.6	0.7	9.21	127	54.3	8.99E-03
1E-07	8.75	92.2	57.4	0.7	884	52.8	0.7	11.4	121	67.0	8.75E-03

Table A.4 Parameters of best fit to model circuit $R_S + Q_1/(R_2+Q_2)/(R_3+C_4/R_4)$ for electrochemical impedance spectra of the hematite electrode in 10^{-6} M phosphate, 5 mM $NaClO_4$, pH 6.00 – 8.75.

C_{PO4} (M)	pH	R_S (Ω)	Q_1 ($\mu F \cdot s^{\alpha-1}$)	α_1	R_2 (Ω)	Q_2 ($\mu F \cdot s^{\alpha-1}$)	α_2	R_3 (kΩ)	C_4 (μF)	R_4 (kΩ)	χ^2
1E-06	6.00	89.5	56.2	0.7	813	103	0.7	3.59	134	23.5	2.40E-02
1E-06	6.25	89.3	56.0	0.7	801	103	0.7	3.71	130	24.2	2.05E-02
1E-06	6.50	87.9	56.3	0.7	851	88.2	0.7	4.42	125	30.5	1.71E-02
1E-06	6.75	87.6	56.5	0.7	890	78.3	0.7	5.36	123	35.1	1.01E-02
1E-06	7.00	87.2	56.6	0.7	883	80.2	0.7	5.20	121	34.0	9.91E-03
1E-06	7.25	86.9	56.6	0.7	866	83.8	0.7	4.89	121	32.9	1.19E-02
1E-06	7.50	86.0	56.9	0.7	909	70.0	0.7	6.10	122	39.6	5.92E-03
1E-06	7.75	85.7	56.8	0.7	904	69.7	0.7	6.03	123	39.6	6.14E-03
1E-06	8.00	85.1	57.1	0.7	918	69.6	0.7	6.19	122	40.3	5.59E-03
1E-06	8.25	84.2	57.5	0.7	935	60.9	0.7	7.90	120	49.3	4.36E-03
1E-06	8.50	84.5	57.7	0.7	928	55.6	0.7	9.64	119	57.8	4.09E-03
1E-06	8.75	83.4	58.1	0.7	938	54.0	0.7	10.6	117	62.5	4.65E-03

Table A.5 Parameters of best fit to model circuit $R_S + Q_1/(R_2+Q_2)/(R_3+C_4/R_4)$ for electrochemical impedance spectra of the hematite electrode in 10^{-5} M phosphate, 5 mM $NaClO_4$, pH 6.00 – 8.75.

C_{PO4} (M)	pH	R_S (Ω)	Q_1 ($\mu F \cdot s^{\alpha-1}$)	α_1	R_2 (Ω)	Q_2 ($\mu F \cdot s^{\alpha-1}$)	α_2	R_3 (kΩ)	C_4 (μF)	R_4 (kΩ)	χ^2
1E-05	6.00	98.8	57.0	0.7	826	118	0.7	2.92	155	24.1	3.34E-02
1E-05	6.25	97.0	57.6	0.7	801	122	0.7	2.73	154	24.2	2.86E-02
1E-05	6.50	93.0	58.7	0.7	855	111	0.7	3.10	144	30.1	2.09E-02
1E-05	6.75	93.7	58.6	0.7	883	100	0.7	3.54	135	37.0	1.63E-02
1E-05	7.00	93.8	58.7	0.7	900	98.8	0.7	3.83	134	40.5	7.98E-03
1E-05	7.25	92.6	58.5	0.7	932	89.5	0.7	4.27	129	47.7	8.57E-03
1E-05	7.50	93.3	58.6	0.7	940	86.3	0.7	4.58	135	51.3	8.25E-03
1E-05	7.75	92.6	58.8	0.7	949	86.9	0.7	4.69	134	50.2	9.60E-03
1E-05	8.00	92.5	59.1	0.7	987	74.2	0.7	5.49	133	66.2	1.17E-02
1E-05	8.25	91.1	58.7	0.7	976	67.2	0.7	6.49	120	73.8	5.82E-03
1E-05	8.50	90.8	59.3	0.7	987	59.7	0.7	8.10	119	97.4	4.84E-03
1E-05	8.75	89.9	59.6	0.7	996	54.6	0.7	10.6	119	18.0	1.00E-02

Table A.6 Parameters of best fit to model circuit $R_S + Q_1/(R_2+Q_2)/(R_3+C_4/R_4)$ for electrochemical impedance spectra of the hematite electrode in 10^{-4} M phosphate, 5 mM $NaClO_4$, pH 6.00 – 8.75.

C_{PO4} (M)	pH	R_S (Ω)	Q_1 ($\mu F \cdot s^{\alpha-1}$)	α_1	R_2 (Ω)	Q_2 ($\mu F \cdot s^{\alpha-1}$)	α_2	R_3 (kΩ)	C_4 (μF)	R_4 (kΩ)	χ^2
1E-04	6.00	98.3	59.7	0.7	692	213	0.7	1.45	265	10.9	1.85E-02
1E-04	6.25	99.0	59.9	0.7	707	209	0.7	1.61	234	13.3	1.06E-02
1E-04	6.50	94.1	60.3	0.7	743	190	0.7	1.76	211	17.2	9.84E-03
1E-04	6.75	93.0	60.5	0.7	781	174	0.7	1.87	197	21.4	1.09E-02
1E-04	7.00	92.6	60.4	0.7	826	153	0.7	2.16	179	30.2	1.11E-02
1E-04	7.25	92.1	60.6	0.7	898	126	0.7	2.53	164	42.8	1.00E-02
1E-04	7.50	91.0	60.6	0.7	935	106	0.7	3.00	154	55.1	1.02E-02
1E-04	7.75	90.9	61.0	0.7	987	92.7	0.7	3.90	147	72.8	1.15E-02
1E-04	8.00	90.1	60.7	0.7	1030	80.4	0.7	4.07	147	66.8	7.84E-03
1E-04	8.25	88.8	60.7	0.7	1040	68.9	0.7	5.10	138	86.5	8.12E-03
1E-04	8.50	89.4	60.9	0.7	1040	61.1	0.7	6.52	129	105	6.89E-03
1E-04	8.75	89.1	61.0	0.7	1030	53.7	0.7	9.16	120	148	7.08E-03